Feshbach resonances and the three-body problem

Liam Cook

Department of Physics and Astronomy

University College London

A thesis submitted for the degree of

Doctor of Philosophy

February 2012

Role of the author

I confirm that the work presented in this thesis is my own. Where information has been derived from other sources, I confirm that this is indicated.

Much of the research presented in this thesis was the result of several multinational collaborations. In chapter 3 I performed the calculations referred to as "coupled-channels calculations", using computer codes that were entirely developed independently by myself. MQDT and ABM calculations were performed by other groups based respectively at NIST (National Institute of Standards and Technology) and at the Eindhoven University of Technology. Experiments (including processing of raw data) were carried out by three other groups, they are differentiated within the text by their respective geographical locations: J. Walraven and coworkers (Universiteit van Amsterdam), I. Bloch and coworkers (LMU Munich), and T. Esslinger and coworkers (ETH Zürich). All descriptions of experiments in the text are based on detailed accounts kindly given to me by the relevant groups.

All theoretical calculations in chapter 4 were designed and implemented by me. The Experiment was performed by the group of Immanuel Bloch (Munich).

Chapter 6 represents a collaboration between myself and Mark Lee of the University of Southampton. We both designed the project, developed the model, and contributed towards the analysis of the results.

The preparation of chapters 1, 2, 5 and 7 did not involve collaboration with others.

Liam Cook

Papers in preparation

The research presented in this thesis will also appear in the following papers, which are currently in preparation.

- **Detailed characterisation of magnetically tuneable Feshbach resonances in ^{40}K.**
  A. Ludewig, L. Cook, M.R. Goosen, T.M. Hanna, T.G. Tiecke, U. Schneider, L. Tarruell, I. Bloch, T. Esslinger, P.S. Julienne, S.J.J.M.F. Kokkelmans, and J.T.M. Walraven.
- **Photodissociation of $^{40}K_2$ Feshbach molecules.**
  Liam Cook, Ulrich Schneider, Simon Braun, Lucia Hackermüller, Sebastian Will, Thorsten Best, Paul Julienne, and Immanuel Bloch.
- **Many-body dynamics of p-wave Feshbach molecule production: a mean-field approach.**
  L. Austen, L. Cook, M. D. Lee and J. Mur-Petit.
- **Three-body recombination and atom dimer-collisions in ^{39}K.**
  Liam Cook and Mark Lee.

Abstract

By applying a magnetic field across a trapped ultracold gas of alkali metal atoms, it is possible to alter the binding energies of near threshold molecular states. The proximity of molecular states to the scattering threshold has a strong effect on the threshold scattering characteristics. Because of this the magnetic field strength can be used to control low energy scattering within the gas. This resonant phenomena is referred to as a magnetically tuneable Feshbach resonance. This thesis looks at these and related phenomena in the context of trapped potassium atoms.

First, we perform coupled-channels calculations in order to characterise a group of previously unreported Feshbach resonances, occurring in a host of different collision channels. Next, we compare these characterisations to empirical data, and more simplified models.

Second, a detailed investigation into the photodissociation of weakly bound Feshbach molecules is carried out. This allows us to gain new insights into the structure of the exit channel interaction. We make semi-classical arguments which enable experimentalists to directly measure the height of potential barriers. We also perform detailed numerical calculations which, in conjunction with experimental data, allow us to develop a fine-tuned potential model for the exit state.

Third, we model weakly bound triatomic states and their impact on near threshold scattering. Then, we discuss the use of three body recombination as a tool for observing Efimov states. Furthermore, we model the three body recombination rate using a simplified two channel model.

Finally we suggest a method intended to provide the basis for numerical calculations using realistic Born-Oppenheimer potentials. It could also be used to analytically study near threshold three body physics.

To my family and friends.

Acknowledgements

I have had the pleasure of working with a range of different and interesting characters over the last few years. I would like to thank Jordi Mur-Petit for his help during the early days. Thank you to Dr. Luke Austen for many stimulating discussions, and his ability to debate any topic. I would like to thank Mark Lee for his help with navigating the icy cold slopes of scattering theory and few body physics, and for providing valuable comments on an early draft of this thesis. I am also indebted to Tania Montero for her very useful feedback on earlier drafts of this work.

I acknowledge gratefully Ulrich Schneider, Immanuel Bloch, Tim Rom, and the rest of their group at the LMU and MPQ for making my year in Munich productive and fun.

Tom Hanna, and Paul Julienne have been very kind to me over the years. They provided me with collaborative projects, useful discussions, and a couple of very enjoyable trips to NIST. For these things I am very grateful.

I would also like to thank Maria and all the good friends whom I have lived with over the years – for frequently reminding me that there is fun to be had outside of working.

Thank you also to Tessa and Matt for all the good times we had in Bristol and Liverpool - all of which were fun and often much needed escapades from work and London. Last but not least, I would like to thank Mum, Callum and Madeleine for their continuous and caring support and for always providing a place to go back to.

Contents

List of Figures

List of Tables

LIST OF TABLES

1

Introduction

The successful creation of a Bose-Einstein condensate out of an ultracold atomic vapour in 1995 [1, 2] was a watershed moment in the development of an emerging research field. This realisation of the ideas originating from Bose and Einstein, around 70 years prior [3, 4], built on earlier work developing the engineering techniques of laser cooling and trapping through the 1970's and 1980's [5]. A similar time period elapsed between the initial considerations of Fermi-Dirac statistics [6, 7, 8] and the creation of the first degenerate Fermi-gas of atoms in the lab [9]. Since then things have progressed somewhat, with the field now containing many subfields including, amongst other things, resonantly interacting gases [10], gases of weakly bound molecules [11], polar molecules [12], Efimov's effect [13] , simulating condensed matter physics [14, 15, 16], and gases consisting of mixed atomic species [17, 18, 19, 20, 21, 22, 23, 24, 25].

Ultracold atomic vapours have some unique defining features. Firstly they are very cold, typically temperatures are in the range 0.001-1 μK. Secondly, they are very dilute, with the density of atoms within the vacuum chamber being on the order of 10^{13}-10^{15} cm^{-1} [26]. Thirdly they have a high degree of quantum degeneracy, with the de Broglie wavelength similar in magnitude to the spacing of the atomic constituents. Due to this low density and temperature we may reasonably consider the case of two atoms colliding starting from a point where we neglect all atoms apart from the colliding pair. Furthermore, for bosons and fermions in different internal states, we may neglect collision orbitals with angular momentum $l > 0$. The reason being that collision channels with $l > 0$ have a centrifugal barrier, shielding the atoms from the potential. This leaves only the $l = 0$ s-wave collisions, which at low temperature are entirely charac-

terised by a single quantity, the s-wave scattering length a_s. This quantity is extremely sensitive to the proximity of a bound state to the scattering threshold. For fermions in the same internal state s-wave collisions are forbidden by symmetry considerations and only p-wave ($l = 1$) collisions are allowed.

A particularly important development has been the ability to manipulate the trapped ultracold gas using lasers and electromagnetic fields. Not merely the confinement of the sample, but also the manner in which those atoms interact with one another. One tool that has been particularly useful is the magnetically tuneable Fano-Feshbach resonance in collisions between alkali metal atoms [27, 28]. This is not the only phenomena with the label Feshbach resonance, but as there will be no ambiguity, here we will refer to this as a Feshbach resonance for short. The concept can be traced back to Fano's [29, 30] considerations of electron tunneling in atomic orbitals through a barrier into continuum modes. Feshbach considered rate enhancement in nucleon collisions due to coupling with a bound state in some sub-system [31, 32]. It transpired that the two ideas were in fact equivalent [30]. The first consideration of the effects on scattering cross sections of tuning an applied magnetic field came in ref. [33] where Tiesinga, Verhaar and Stoof considered Cs+Cs collisions. In short by adjusting the magnitude of a homogeneous magnetic field the scattering length can be, in principle, tuned so as to take on any real value. These resonances were experimentally realised and the results pulished 6 years later in 1999 by Vuletić *et al* [34]. Concurrent experiments worked with Na [35] and Rb [36, 37].

Collisions involving three atoms play an important role in many experiments. Three-body recombination, the process where three atoms collide forming a dimer and one free atom, limits the lifetime of experiments and causes heating within the sample. They can also be seen as tool for probing exotic three-body bound states. As early as 1935, Thomas [38] showed that three weakly interacting particles can form a trimer state, even though the pairwise potential is very shallow. This bound state persists when the pairwise potential is so weak that it does not support a single dimer state. Later in 1970, Efimov [39] discovered that if one considers three resonantly interacting particles, in the limit $a \to \pm\infty$, Thomas' effect can be extended to give an infinite series of excited three-body energy levels accumulating at the threshold. First progress towards experimental realisation of this phenomena in atomic systems came in molecular beam diffraction experiments working with ^{4}He [40, 41]. They were able to clearly resolve

diffraction peaks associated with helium dimers and trimers. A series of experiments, employing Feshbach resonances as a crucial tool, have been more recently performed in the alkalis [13, 42, 43, 44, 45, 46, 47, 48, 49, 50, 51, 52]. Modelling three body quantum mechanical systems is significantly more challenging than their two body counterparts. Indeed, this is obviously true since a three body collision will contain (in the minimum) all of the two body interactions pairwise three times over. It was, in fact, a non-trivial exercise in functional analysis to demonstrate that one can formulate a set of equations consisting of operators well behaved enough to admit unique and calculable solutions [53]. A different approach was introduced by Alt, Grassberger and Sandhas [54]. The two derivations give equivalent solutions, but the latter is often seen as giving a more convenient set of equations.

This thesis begins by stating some of the important textbook results of scattering theory. Limited to the essential ideas necessary for understanding the rest of the thesis. It then continues by reviewing the basic theory required to describe Feshbach resonances. The results are standard (at least for s-wave resonances), but the derivation is designed to introduce an approach and notation that fits with later work in the thesis. We then introduce textbook elements of atomic physics in the presence of a magnetic field.

In the third chapter a survey of Feshbach resonances in diatomic ^{40}K collisions is carried out. A new 'coupled-channels' computer program is developed and is used in tandem with experimental investigations (carried out by collaborating groups). Development of the program, in the MATLAB programming language, was in itself a significant task. However, it is only referred to by way of the results that it produces. The resulting numerical data is used to help develop simplified models of Feshbach resonances.

Chapter 4 puts forward a detailed account of the photodissociation of Feshbach molecules by laser light blue detuned from an atomic transition. Textbook descriptions of scattering theory and matter light interactions are combined in a straight forward way to give a detailed account of the mathematical model used here. A further MATLAB code is developed to solve the problem numerically. To the best of my knowledge this is the first time a a program to study the photodissociation of Feshbach molecules has been written. New analytical results are derived by developing a semi-classical model of the photodissociation process; concentrating mainly on the photodissociation in the vicinity of a potential barrier in the final state interaction. This allows one to extract,

directly from the experimental data, the height of the potential barrier. A new potential model for the outgoing state is developed.

In chapter 5 we elucidate our approach to modelling few body physics in terms of simplified pairwise interactions. To this end, we conduct a study of the helium dimer and trimer using standard pseudo-potential methods applied to the Faddeev equations. This system has been studied experimentally and theoretically and so allows for a detailed critique of, and introduction to, the methods that we will later use in a more complicated problem.

The sixth chapter of this thesis is devoted to modelling three body recombination in alkali metal atoms. Specifically we study three body recombination in the vicinity of a broad resonance in homonuclear collisions of ^{39}K atoms. We use our previously tested coupled-channels code to build detailed knowledge of the near threshold physics. Armed with this we construct a two channel model of the Feshbach resonance, with pseudo-potentials used in the channel Hamiltonians. We compare our three body recombination rate predications to experimental observations reported in the literature.

Chapter 7 develops a new representation of the potential and T-matrix. This is intended for use in few body studies where realistic pairwise interactions are to be used. Standard methods from the theory of integral equations, and AGS theory [54], are applied and tailored for near threshold calculations. An exact expansion in terms of zero energy bound states (half-bound states for s-wave collisions) is given in detail. Mass scaling is discussed and a possible application to the ytterbium system is suggested.

The final chapter gives an overview of the achievements put forward in this thesis.

2

Magnetically tuneable Feshbach resonances

2.1 Introduction

In this chapter we briefly introduce some of the important tools and notation that will feature prominently in subsequent chapters. We introduce the basic concepts underpinning the theory of quantum mechanical scattering. The details of the interaction between two atoms with a single valence electron are introduced. We go on to discuss the concept of resonant enhancement of scattering, and how, for alkali metal atomic collisions, it may be induced by the application of a magnetic field. A simple two-channel model, which encapsulates the notable details of these magnetically controllable resonances, is introduced.

2.2 Scattering theory

2.2.1 Time dependent scattering theory

Working in the centre of mass frame allows us to discuss the scattering of two particles in a manner similar to the scattering of one particle, of reduced mass μ, from a fixed external potential [55]. The scattering process can be envisaged as follows: an initial wave packet is far from the scattering centre, and so does not feel the effects of the potential. Its wave function evolves according to the solution of the time dependent Schrödinger equation, $|\Psi(t)\rangle = \exp(-iHt/\hbar)|\Psi\rangle$. Here H is the full Hamiltonian, and

H_0 is the Hamiltonian in the absence of a potential. Over time it follows what in a classical sense would be called an orbit. At some intermediate times it feels the effects of the potential, before evolving, in the distant future, once again free from the potential. Given the free nature of the state a long time before and after the collision it is convenient to introduce the asymptotic reference wave functions $|\phi_{\text{in}}\rangle$ and $|\phi_{\text{out}}\rangle$. These are defined such that they converge strongly [55, 56] with the full wave function, $|\Psi(t)\rangle$, in the following manner

$$\lim_{t\to-\infty(+\infty)} \left|\left| e^{-\frac{i}{\hbar}Ht}|\Psi\rangle - e^{-\frac{i}{\hbar}H_0 t}|\phi_{\text{in(out)}}\rangle \right|\right| = 0. \tag{2.1}$$

We are not interested in the intermediate times. It is sufficient for our purposes to know that, given a particular initial state, there is some probability, w, for obtaining a particular outgoing state which we call $|\chi\rangle$. In this spirit, it is possible to describe a scattering operator S such that this probability, is given in terms of the asymptotic reference states

$$w(\chi \leftarrow \phi_{\text{in}}) = |\langle\chi|S|\phi_{\text{in}}\rangle|^2 . \tag{2.2}$$

This is the first step towards the often desirable removal of the time dependence from the formalism.

2.2.2 Time independent scattering theory

We have seen that the intrinsic time dependence of the scattering problem leads to time dependent state vectors and inconvenient infinite limits. It is possible to entirely remove this time dependence from the theory, thus removing the infinite limits [55, 56]. This sees matrix elements of the S operator being written

$$\langle \boldsymbol{p'}|S|\boldsymbol{p}\rangle = \delta\left(\boldsymbol{p'}-\boldsymbol{p}\right) - 2\pi i\delta\left(\frac{p'^2}{2\mu}-\frac{p^2}{2\mu}\right)\langle \boldsymbol{p'}|T\left(\frac{p^2}{2\mu}+i0\right)|\boldsymbol{p}\rangle, \tag{2.3}$$

where the $i0$ indicates that the argument of the transition operator T approaches the real axis from the upper half of the complex plane. This limit in momentum space is the remnant of the time dependence described in the previous section. Its inclusion is the trade off one has to make in order to arrive at a time independent scattering theory. The physical interpretation of eq. (2.3) is clear; one term which gives an amplitude for the particle to not be scattered at all, and one which corresponds to the amplitude for

scattering $|\boldsymbol{p}\rangle$ into $|\boldsymbol{p'}\rangle$, whilst conserving total energy. Here $|\boldsymbol{p}\rangle$ is an eigenstate of the kinetic energy operator and is defined as

$$\langle \boldsymbol{r}|\boldsymbol{p}\rangle = \frac{1}{(2\pi\hbar)^{3/2}} e^{i\boldsymbol{p}.\boldsymbol{r}/\hbar}, \tag{2.4}$$

where $\boldsymbol{r}$ is the vector describing the separation of the two particles. We have also defined an operator $T(z)$ (where z is a complex argument) which contains all the information needed to give the scattering operator S.

Considering the Dirac delta-functions in eq. (2.3) it is clear that T benefits from being less singular than S. The Lippmann-Schwinger equation [55] for T is

$$T(z) = V + VG_0(z)T(z), \tag{2.5}$$

where the free Green's operator G_0 is defined as $G_0(z) = (z - H_0)^{-1}$, and V is the potential operator. It is at this point that we introduce the Green's operator,

$$G(z) = (z - H)^{-1}, \tag{2.6}$$

which can be related to T via

$$G(z) = G_0(z) + G_0(z)T(z)G_0(z). \tag{2.7}$$

By virtue of G being defined directly in terms of the Hamiltonian it is often a more convenient starting point when considering more complex multichannel problems.

Finally, it is also possible to decompose the T operator into partial waves,

$$\langle p\hat{\mathbf{p}}'|T(z)|\mathbf{p}\rangle = \sum_{l=0}^{\infty} \sum_{m=-l}^{l} Y_{lm}(\hat{\mathbf{p}}')Y^*_{lm}(\hat{\mathbf{p}})\langle plm|T(z)|plm\rangle, \tag{2.8}$$

where we have used the expansion of the plane wave state,

$$|\boldsymbol{p}\rangle = \sum_{l=0}^{\infty} \sum_{m=-l}^{l} e^{il\pi/2}|p,l,m\rangle Y^*_{lm}(\hat{\boldsymbol{p}}), \tag{2.9}$$

and Y_{lm} is the spherical harmonic. In eq. (2.8) we have assumed that the interaction is central and so does not couple different partial waves, but this is not always the case as we will see later when we consider the weak anisotropic dipole-dipole interaction of

the two electron spins. It is well known [55, 56] that in the low collision energy limit the matrix elements on the right hand side of eq. (2.8) go as

$$\lim_{p\to 0} \langle plm|T(z)|plm\rangle = \frac{(4\pi\hbar)^2}{2\mu(2\pi\hbar)^3}\frac{a_{lm}p^{2l}}{\hbar^{2l}}. \tag{2.10}$$

The important contribution here is $a_{lm}p^{2l}$, which demonstrates that only one parameter is required to characterise the low energy scattering in each partial wave, the scattering length[1]. Furthermore lower partial waves will dominate increasingly as p is reduced allowing one to neglect all but a few values of l in the summation of eq. (2.8). At extremely low temperatures, like the ones we will be mainly concerned with, all but the lowest partial wave $l = 0$ can be neglected and the scattering then becomes isotropic, and well described by the s-wave scattering length a_s alone. For the special case of scattering between two identical fermionic particles, s-wave interactions are forbidden by symmetry requirements, and so p-wave collisions will dominate at low kinetic energies. One important caveat, though, is that the functional form of the inter-particle interaction should obey certain constraints in order that a_{lm} be mathematically well defined, see, for example, refs. [55, 56].

Although we have discussed the Green's function and T-operator entirely in the context of scattering. It is important to point out certain key properties of these operators when z takes on certain negative real values. When z is in the point spectrum of H it is clear from eq. (2.6) that G is defined in terms of the inverse of a singular operator. In fact the operators exhibit poles that dominate in the regions surrounding them. If there is a bound state near the scattering threshold, then it is expected that the associated pole will have an effect on scattering properties. An extreme example would be that of a bound state with $l = 0$, degenerate with the scattering threshold, which will cause the s-wave scattering length to diverge. This is known as a zero energy resonance [55].

[1]We note that for $l \neq 0$ this quantity does not have the dimensions of a length, for example, a_p ($l = 1$) is sometimes referred to as the scattering volume instead.

2.3 Resonance enhanced scattering

2.3.1 Magnetic tuneability

Magnetically tuneable Feshbach resonances in ultra-cold gases of alkali metal atoms [27, 28] are phenomena that facilitate many of the current experiments with quantum gases. Figure 2.1 lays out the main features, indicating that they occur when colliding atoms with particular internal configurations are coupled to a near degenerate bound state with a different internal configuration. The energy difference between the scattering threshold and the bare bound state can be adjusted by the application of a magnetic field. Near where the two are energetically degenerate there is a divergence in the s-wave scattering length [55].

Due to the Pauli principle identical fermions cannot undergo s-wave collisions. In this case it is the p-wave scattering volume that diverges. A crucial property of the Feshbach resonance is that the scattering length's magnitude and sign can be adjusted at will.

2.3.2 A two channel picture

A two channel model can be developed to illustrate the properties of magnetically tuneable Feshbach resonances. It is often significantly simpler than a full treatment of the two-body physics, and so can also be used as a starting point when seeking to model few or many body physics in the vicinity of a Feshbach resonance. The atoms enter the collision in a channel which we refer to as the background channel, this is coupled to another channel we refer to as the closed channel. The word closed here indicates that the atoms do not have sufficient kinetic energy to exit the collision in this channel. An energetically allowed exit channel is referred to as open. Their respective channel Hamiltonians are H_{bg}, H_{cl}, and they are coupled by $\mathcal{W}$, such that the total Hamiltonian is written

$$H = \begin{pmatrix} H_{\mathrm{bg}} & \mathcal{W} \\ \mathcal{W} & H_{\mathrm{cl}} \end{pmatrix}. \tag{2.11}$$

We can define the Green's operator and its components in the usual way

$$G(z) = (z - H)^{-1} = \begin{pmatrix} G_{\mathrm{bg\,bg}}(z) & G_{\mathrm{bg\,cl}}(z) \\ G_{\mathrm{cl\,bg}}(z) & G_{\mathrm{cl\,cl}}(z) \end{pmatrix}. \tag{2.12}$$

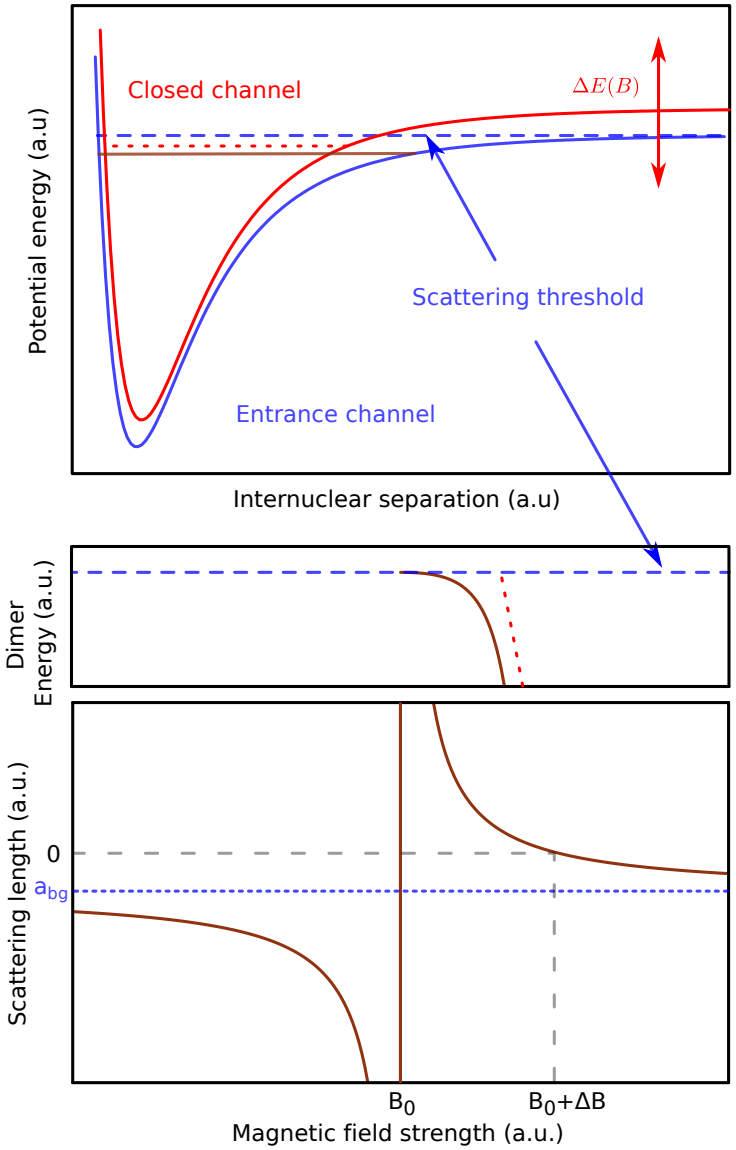

Figure 2.1: A cartoon representation of a magnetically tuneable Feshbach resonance. The upper plot indicates the presence of two spin channels, one of which contains a bound state (red dotted line). The energy of this bound state, relative to the entrance channel threshold, is manipulated by adjusting the applied magnetic field. The solid brown line indicates the presence of a Feshbach molecular state constituted by a mixture of the two spin states. The middle plot shows the trajectory of the closed channel bound state relative to the entrance channel scattering threshold, and the energy of the Feshbach molecular state which is proportional to the inverse square of the scattering length. The scattering length is shown in the lower plot, it can be seen to diverge where the Feshbach molecular state becomes degenerate with the entrance channel scattering continuum.

Where the channel Green's operators are defined as

$$\mathcal{G}_{\mathrm{bg}}(z) = (z - H_{\mathrm{bg}})^{-1}, \tag{2.13}$$

and

$$\mathcal{G}_{\mathrm{cl}}(z) = (z - H_{\mathrm{cl}})^{-1}, \tag{2.14}$$

which would describe the system in the absence of inter-channel coupling. If we define a zero order resolvent as

$$G_0(z) = \begin{pmatrix} \mathcal{G}_{\mathrm{bg}}(z) & 0 \\ 0 & \mathcal{G}_{\mathrm{cl}}(z) \end{pmatrix}, \tag{2.15}$$

then we can use the Lippmann-Schwinger equation

$$G(z) = G_0(z) + G_0(z) W G(z) \tag{2.16}$$

with the *potential* given by

$$W = \begin{pmatrix} 0 & \mathcal{W} \\ \mathcal{W} & 0 \end{pmatrix}. \tag{2.17}$$

Since the non-entrance channel here is closed, we only need to calculate one component of $G(z)$. This contains all information pertaining to scattering amplitudes, and the bound state spectrum. The component can be obtained by iterating eq. (2.16)

$$G_{\mathrm{bg\,bg}}(z) = \mathcal{G}_{\mathrm{bg}}(z) + \mathcal{G}_{\mathrm{bg}}(z)\mathcal{W}\mathcal{G}_{\mathrm{cl}}(z)\mathcal{W}G_{\mathrm{bg\,bg}}(z). \tag{2.18}$$

Motivated by the pole structure of the Green's operator, the single resonance approximation replaces the closed channel Green's operator with

$$\mathcal{G}_{\mathrm{cl}}(z) \approx \frac{|\phi_{\mathrm{res}}\rangle\langle\phi_{\mathrm{res}}|}{z - E_{\mathrm{res}}}, \tag{2.19}$$

where it is assumed that the coupling is dominated by one closed channel bound state with other closed channel bound states and the closed channel scattering continuum energetically far away. By substituting (2.19) into (2.18) and performing repeated iteration of the equation

$$G_{\mathrm{bg\,bg}}(z) = \mathcal{G}_{\mathrm{bg}}(z) + \mathcal{G}_{\mathrm{bg}}(z)\mathcal{W}\frac{|\phi_{\mathrm{res}}\rangle\langle\phi_{\mathrm{res}}|}{z - E_{\mathrm{res}}}\mathcal{W}\mathcal{G}_{\mathrm{bg}}(z)\sum_{n=0}^{\infty}\left[\frac{\langle\phi_{\mathrm{res}}|\mathcal{W}\mathcal{G}_{\mathrm{bg}}(z)\mathcal{W}|\phi_{\mathrm{res}}\rangle}{z - E_{\mathrm{res}}}\right]^n, \tag{2.20}$$

we then sum the infinite series

$$\sum_{n=0}^{\infty}\left[\frac{\langle\phi_{\mathrm{res}}|\mathcal{W}\mathcal{G}_{\mathrm{bg}}(z)\mathcal{W}|\phi_{\mathrm{res}}\rangle}{z - E_{\mathrm{res}}}\right]^n = \left(1 - \frac{\langle\phi_{\mathrm{res}}|\mathcal{W}\mathcal{G}_{\mathrm{bg}}(z)\mathcal{W}|\phi_{\mathrm{res}}\rangle}{z - E_{\mathrm{res}}}\right)^{-1}. \tag{2.21}$$

The background channel Green's function can be related to the background channel T-matrix $\mathcal{T}_{\rm bg}(z)$,

$$\mathcal{G}_{\rm bg}(z) = \mathcal{G}_0(z) + \mathcal{G}_0(z)\mathcal{T}_{\rm bg}(z)\mathcal{G}_0(z), \tag{2.22}$$

and by analogy we can extract a T-matrix $T_{\rm bg\,bg}$ that is related to the Green's function

$$G_{\rm bg\,bg}(z) = \mathcal{G}_0(z) + \mathcal{G}_0(z)T_{\rm bg\,bg}(z)\mathcal{G}_0(z), \tag{2.23}$$

where the free resolvent is as usual

$$\mathcal{G}_0(z) = (z - H_0)^{-1}. \tag{2.24}$$

We can recall the partial wave decomposition of the T-matrix where, assuming that different partial waves are not coupled,

$$\langle p\hat{\mathbf{p}}'|T_{\rm bg\,bg}(z)|\mathbf{p}\rangle = \sum_{l=0}^{\infty}\sum_{m=-l}^{l} Y_{lm}(\hat{\mathbf{p}}')Y_{lm}^*(\hat{\mathbf{p}})\langle plm|T_{\rm bg\,bg}(z)|plm\rangle. \tag{2.25}$$

We can then define the scattering length in an arbitrary partial wave for this two channel single resonance model as

$$a_{lm} = \lim_{p\to 0} -\frac{\hbar^{2l}}{p^{2l}} f_{lm}(p) = \lim_{p\to 0} \frac{\hbar^{2l}}{p^{2l}} \frac{2\mu(2\pi\hbar)^3}{(4\pi\hbar)^2} \left\langle plm \left| T_{\rm bg\,bg}\left(\frac{p^2}{2\mu}\right)\right| plm\right\rangle, \tag{2.26}$$

where $f_{lm}(p)$ is the partial wave scattering amplitude [55]. Bringing this together, applying the limits, making use of the definition of the scattering state $|\phi_{\boldsymbol{p}}^{(\pm)}\rangle$ [56]

$$\mathcal{G}_{\rm bg}\left(\frac{p^2}{2\mu} \pm i0\right)\mathcal{G}_0\left(\frac{p^2}{2\mu} \pm i0\right)^{-1}|\boldsymbol{p}\rangle = i0\,\mathcal{G}_{\rm bg}\left(\frac{p^2}{2\mu} \pm i0\right)|\boldsymbol{p}\rangle = |\phi_{\boldsymbol{p}}^{(\pm)}\rangle, \tag{2.27}$$

and its partial wave decomposition,

$$|\phi_{\boldsymbol{p}}^{(\pm)}\rangle = \sum_{l=0}^{\infty}\sum_{m=-l}^{l} e^{i\pi l/2}|\phi_{plm}^{\pm}\rangle Y_{lm}^*(\hat{p}), \tag{2.28}$$

we arrive at an explicit equation for the scattering length that we have defined in eq. (2.26)

$$a_{lm} = a_{\rm bg} + \lim_{p\to 0} \frac{\hbar^{2l}}{p^{2l}} 2\mu \frac{(2\pi\hbar)^3}{(4\pi\hbar)^2} \frac{\langle\phi_{plm}^{(-)}|\mathcal{W}|\phi_{\rm res}\rangle\langle\phi_{\rm res}|\mathcal{W}|\phi_{plm}^{(+)}\rangle}{\frac{p^2}{2\mu} - E_{\rm res} - \langle\phi_{\rm res}|\mathcal{W}\mathcal{G}_{\rm bg}(\frac{p^2}{2\mu} + i0)\mathcal{W}|\phi_{\rm res}\rangle}. \tag{2.29}$$

If we now assume that the energy of the closed channel bound state, relative to the background channel scattering threshold, varies linearly with magnetic field, then we can quote the well known resonance formula

$$a_{lm}(B) = a_{lm}^{\mathrm{bg}} \left(1 - \frac{\Delta B}{B - B_0}\right). \tag{2.30}$$

Here the parameters are the background scattering length a_{lm}^{bg}, resonance magnetic field strength B_0, and width ΔB, fig. 2.1 shows the significance of these values. The parameterisation can be completed by relating them to the matrix elements that we have derived in relation to $G_{\mathrm{bg,bg}}(z)$,

$$\lim_{p\to 0} \frac{p^2}{2\mu} - E_{\mathrm{res}} - \langle \phi_{\mathrm{res}} | \mathcal{W} \mathcal{G}_{\mathrm{bg}}(p^2/2\mu + i0) \mathcal{W} | \phi_{\mathrm{res}} \rangle = \frac{\partial E_{\mathrm{res}}}{\partial B} (B - B_0), \tag{2.31}$$

and,

$$\lim_{p\to 0} \frac{\hbar^{2l}}{p^{2l}} \frac{2\mu}{(4\pi\hbar)^2} (2\pi\hbar)^3 \langle \phi_{plm}^{(-)} | \mathcal{W} | \phi_{\mathrm{res}} \rangle \langle \phi_{\mathrm{res}} | \mathcal{W} | \phi_{plm}^{(+)} \rangle = a_{lm}^{\mathrm{bg}} \frac{\partial E_{\mathrm{res}}}{\partial B} \Delta B. \tag{2.32}$$

It is worth noting that at no point here have we restricted ourselves to s-waves. The above parameterisations are in principle applicable to any partial-wave. The only difference is in the physical significance of a_{lm} for any particular l.

2.4 Two alkali metal atoms in a magnetic field

It is clear that the discussion in sec. 2.3.2 represents an idealised system. In reality the scattering of two alkali metal atoms in a magnetic field requires a more detailed discussion.

2.4.1 Angular momentum of the atoms

Adopting Russell-Saunders notation, ${}^{2s+1}l_j$ we denote an alkali metal atom in the electronic ground state as ${}^2S_{1/2}$. Here $\boldsymbol{s}$ is the spin of the unpaired electron, $\boldsymbol{l}$ is its orbital angular momentum, and $\boldsymbol{j} = \boldsymbol{l} + \boldsymbol{s}$ is the total electronic angular momentum. If we have two atoms each in the ${}^2S_{1/2}$ state, then we can consider coupling their respective spins $\boldsymbol{s_1}$ and $\boldsymbol{s_2}$ to form $\boldsymbol{S} = \boldsymbol{s_1} + \boldsymbol{s_2}$. This coupling gives both singlet ($S = 0$) and triplet ($S = 1$) states. If we define the axis of quantisation to be along the direction of the magnetic field vector $\boldsymbol{B}$ then the electronic spin of each atom will also have a projection m_s along that axis. Further to the electronic spins there are also the nuclear spins i_1 and i_2, and their respective projections m_{i1} and m_{i2}.

2.4.2 The Born-Oppenheimer Potentials

In principle the Schrödinger equation for the diatomic system would consist of the Coulomb potential energy of the composite system (two nuclei and $2n$ electrons), and the individual kinetic energies of each of these $2n+2$ constituents. We require a method by which to treat the $2n+2$ positions vectors, reducing the problem to a simpler form.

The part of the total Hamiltonian representing the coulomb energy and electronic kinetic energy is given by

$$H_e(R) = \sum_{i=1}^{n} \left[\frac{-Z_1 e^2}{(4\pi\epsilon_0)|\mathbf{r_i} - \mathbf{R_1}|} + \frac{-Z_2 e^2}{(4\pi\epsilon_0)|\mathbf{r_i} - \mathbf{R_2}|} - \frac{\hbar^2}{2m_e}\nabla^2_{\mathbf{r_i}} \right] + \sum_{i<j=1}^{n} \frac{e^2}{(4\pi\epsilon_0)|\mathbf{r_i} - \mathbf{r_j}|} + \frac{Z_1 Z_2 e^2}{(4\pi\epsilon_0)R}. \tag{2.33}$$

Here $\mathbf{r}$ denotes the coordinate of an electron, $\mathbf{R_1}$ and $\mathbf{R_2}$ are the nuclear coordinates and R is their relative separation, Z_1 and Z_2 are the charges of the nuclei. Clamping the positions of the atomic nuclei ($\mathbf{R}$ is held fixed) and considering the functions that satisfy the equation

$$H_e\Phi_q(\mathbf{R}; \mathbf{r_1}, \mathbf{r_2}, \ldots \mathbf{r_n}) = V_q\Phi_q(\mathbf{R}; \mathbf{r_1}, \mathbf{r_2}, \ldots \mathbf{r_n}), \tag{2.34}$$

the wave function, Ψ, can be expanded as

$$\Psi(\mathbf{R}; \mathbf{r_1}, \mathbf{r_2}, \ldots \mathbf{r_n}) = \sum_q \psi_q(\mathbf{R})\Phi_q(\mathbf{R}; \mathbf{r_1}, \mathbf{r_2}, \ldots \mathbf{r_n}). \tag{2.35}$$

We can identify the set of energies $V_s(R)$ as a set of internuclear (Born-Oppenheimer) potentials that depend on the electronic state of the atoms. In principle the nuclear kinetic energy operator, T_N, would couple these different electronic states. However the Born-Oppenheimer approximation consists of neglecting derivatives of the Φ with repspect to the internuclear coordinates contained arising from T_N, in favour of those derivatives of ψ_q. In addition, only diagonal matrix elements are retained. This is usually justified by reference to the much faster relaxation time of the electrons, when compared to that of the nuclear system [57].

When both atoms are in the $^2S_{1/2}$ state the electronic wave functions have the following symmetries: the singlet ($S = 0$) is described by $^1\Sigma_g^+$, and the triplet ($S = 1$) by $^3\Sigma_u^+$. Here we are following the conventional notation $^{2S+1}|\lambda|^{-/+}_{u/g}$ where λ is the

total projection of electronic orbital angular momentum on the internuclear axis, the superscript $-$ or $+$ indicates a reflection symmetry of the spatial component of the electronic wave function through a plane containing the internuclear axis, and the g/u (gerade/ungerade) subscript indicates even/odd symmetry under inversion of all electrons through the centre of charge. The $-/+$ symmetry only exists for Σ states, also the u/g symmetry only exists for homonuclear systems. In the case, like the one we now consider, where both atoms are in the same electronic state, the g/u symmetry is determined by S, λ, and the $-/+$ symmetry. This describes the scheme with which the potential energy curves arising from eq. (2.34) are labelled.

The long range part of the Born-Oppenheimer potential can be understood by considering the separated atomic limit, with the interatomic interaction being treated peturbatively. Generally this involves the potential being represented by a power series in $1/R$, or dispersion series as it is sometimes known [57, 58]. For the case that we are now considering the leading order contribution is an attractive induced-dipole-induced-dipole or van der Waals interaction which goes as C_6/R^6. The singlet and triplet potentials mentioned above have the same C_6 and so the two potentials are degenerate at large internuclear separation. As the potential is followed to smaller internuclear separations electron exchange becomes gradually more important, causing the singlet and triplet curves to differ in energy. The antisymmetric spin wave function associated with the singlet state results in a symmetric wave function in configuration space. The converse is true for the triplet state; it has an antisymmetric wave function in configuration space. The different symmetries give different charge distributions and so different potential energy curves. At smaller internuclear separations still, there is a splitting between the two potentials created by the difference in chemical bonding interactions from the overlap of the charge distributions.

2.4.3 Zeeman and hyperfine interactions

The Zeeman and hyperfine interactions are treated here in the separated atom picture. As this is the case we need only consider one atom at a time with the understanding that when both atoms are included the appropriate symmetry is applied. This picture clearly has its limitations – when the nuclei are very close together two atoms independently interacting with the magnetic field is not a perfect description. We find, though, that it is sufficient for our purposes throughout this thesis.

The Hamiltonian for interaction between the electronic and nuclear spins with the magnetic field is given by [26]

$$H_z(\boldsymbol{B}) = \mu_B(g_e\boldsymbol{s} + g_n\boldsymbol{i})\cdot\boldsymbol{B}. \tag{2.36}$$

The electronic and nuclear gyromagnetic factors are g_e and g_n respectively, and here μ_B is the Bohr magneton. Defining the direction of the vector $\boldsymbol{B}$ as the axis of quantisation the matrix elements in the $|s, m_s, i, m_i\rangle$ basis can be written down directly as

$$\langle s, m_s, i, m_i|H_z(\boldsymbol{B})|s, m_s', i, m_i'\rangle = \mu_B(g_e m_s + g_n m_i)B\delta_{m_s,m_s'}\delta_{m_i,m_i'}, \tag{2.37}$$

where $\delta_{i,j}$ is the Kronecker delta. In this basis the Zeeman effect only contributes to diagonal elements of the Hamiltonian.

Interaction between the spin of the valence electron and that of the nucleus gives rise to the hyperfine contribution to the Hamiltonian

$$H_{\rm hf} = \frac{C_{\rm hf}}{\hbar^2}\boldsymbol{s}\cdot\boldsymbol{i} = \frac{C_{hf}}{\hbar^2}(s_x i_x + s_y i_y + s_z i_z). \tag{2.38}$$

In order to evaluate the matrix elements of this operator we first make use of the ladder operator form of the elements of an angular momentum operator, $\boldsymbol{j}$,

$$\langle j, m_j|\boldsymbol{j}|j', m_j'\rangle = \langle j, m_j|\begin{pmatrix}\frac{1}{2}[j_+ + j_-]\\ \frac{i}{2}[j_- - j_+]\\ j_z\end{pmatrix}|j', m_j'\rangle = \langle j, m_j|\ldots$$
$$\begin{pmatrix}\frac{\hbar}{2}[j(j+1) - m_j'(m_j'+1)]^{1/2}|j, m_j'+1\rangle + \frac{\hbar}{2}[j(j+1) - m_j'(m_j'-1)]^{1/2}|j, m_j'-1\rangle\\ \frac{\hbar}{2i}[j(j+1) - m_j'(m_j'+1)]^{1/2}|j, m_j'+1\rangle - \frac{\hbar}{2i}[j(j+1) - m_j'(m_j'-1)]^{1/2}|j, m_j'-1\rangle\\ \hbar m_j'|j, m_j'\rangle\end{pmatrix}. \tag{2.39}$$

Applying for $\boldsymbol{s}$ and $\boldsymbol{i}$ in eq. (2.38) allows to state that matrix elements are given by

$$\langle s, m_s, i, m_i|H_{\rm hf}|s, m_s,' i, m_i'\rangle = \frac{C_{\rm hf}}{2}\Big\{2m_s m_i\delta_{m_s,m_s'}\delta_{m_i,m_i'} + \ldots$$
$$\left[s(s+1) - m_s'(m_s'+1)\right]^{1/2}\left[i(i+1) - m_i'(m_i'-1)\right]^{1/2}\delta_{m_s,m_s'+1}\delta_{m_i,m_i'-1} + \ldots$$
$$\left[s(s+1) - m_s'(m_s'-1)\right]^{1/2}\left[i(i+1) - m_i'(m_i'+1)\right]^{1/2}\delta_{m_s,m_s'-1}\delta_{m_i,m_i'+1}\Big\}. \tag{2.40}$$

The Kronecker deltas here indicate that in this uncoupled spin basis the hyperfine interaction has a diagonal contribution to the Hamiltonian; however there are also off-diagonal contributions. These off diagonal elements allow for the flipping of the

electron spin, and a corresponding increase or decrease in the projection of the nuclear spin. It is clear then, that by providing off-diagonal terms, the hyperfine interaction plays an important role, by providing the coupling between states that gives rise to rich resonant structure. This perspective is useful provided that $\mu_B B/\hbar$ is on the order of, or smaller than, C_{hf}. If the magnetic field is very strong then the hyperfine contribution is negligible.

Coupling together the nuclear and electronic spins we define $\boldsymbol{f} = \boldsymbol{s} + \boldsymbol{i}$, and its projection on the quantisation axis m_f. Since $[H_{\mathrm{hf}}, f^2] = [H_{\mathrm{hf}}, m_f] = 0$, we can conclude that f and m_f are good quantum numbers at zero magnetic field[1]. Also, $[H_z(\boldsymbol{B}) + H_{\mathrm{hf}}, m_f] = 0$, and so m_f remains a good quantum number at all magnetic field strengths.

2.4.4 Collision channels

Here we define the important concept of collision channels. Generally they are any possible incoming or outgoing internal configurations of the atoms. When the quantum mechanical scattering theory was introduced we spoke in terms of wave packets at very large distances from the potential centre, where the spatially dependant interaction was no longer present. In the present case this corresponds to the internuclear separation tending to an infinite distance, such that the Born-Oppenheimer potentials have tended to zero. The internal atomic Hamiltonians, specifically here the hyperfine interactions and the Zeeman interaction with the spatially ubiquitous magnetic field, do not disappear as the nuclei are separated. In accordance with this we define the spin nature of the scattering channels to be the products of the separated atomic eigenstates of the Zeeman and hyperfine Hamiltonians with the appropriate (anti)-symmetry requirements applied. This symmetry depends on whether we are considering identical bosons or fermions, and whether the spatial part of the Hamiltonian is projected on to the symmetric or antisymmetric subspace. This is determined in the language of the partial wave expansion by whether l is odd or even. If the atoms are not identical then there are no such symmetry restrictions. The make up of these channel spin states are dependent on the magnetic field since adjusting the magnetic field alters the relative magnitudes of diagonal and off diagonal matrix elements.

[1] Here the commutator $[A, B] = AB - BA$.

In zero magnetic field there are two eigenenergies characterised by the sum of the total electronic angular momentum and the nuclear spin. Since here the electrons only have spin, this quantity is given by $f = i \pm 1/2$. Each of these levels is $2f+1$ degenerate, since for any given f the different projections m_f are equal in energy. As the magnetic field is turned on and increased this degeneracy is lifted due to the Zeeman terms. Here f ceases to be a good quantum number due to mixing between the manifolds. The Hamiltonian so far is symmetrical about the magnetic field axis, as a result the total projection of angular momentum $m_{f1} + m_{f2} = m_{i1} + m_{i2} + m_{s1} + m_{s2}$ remains a good quantum number. Even at finite magnetic field strengths, channels are often labelled $\{f_1, m_{f1}, f_2, m_{f2}\}$, however this refers to the state that originates from the $|f_1, m_{f1}, f_2, m_{f2}\rangle$ state in the zero field limit.

2.4.5 Electron-electron dipole-dipole interaction

One final term that we include in the Hamiltonian accounts for the weak dipolar interaction between the valence electron of atom one and the valence electron of atom two. We take the form of the interaction to be [59]

$$\mathcal{V}^{\mathrm{ss}}(\boldsymbol{r}) = \frac{\alpha^2 E_{\mathrm{h}} a_0^3}{\hbar^2 r^3} \left[\boldsymbol{s}_1 \cdot \boldsymbol{s}_2 - 3(\boldsymbol{s}_1 \cdot \hat{\boldsymbol{r}})(\boldsymbol{s}_2 \cdot \hat{\boldsymbol{r}}) \right]. \tag{2.41}$$

Here $\hat{\boldsymbol{r}}$, E_{h}, and α are the unit vector of interatomic separation ($\boldsymbol{r} = r\hat{\boldsymbol{r}}$), Hartree energy, and fine structure constant respectively. The manipulation of eq. (2.41) into a form more useful for calculating matrix elements is long and algebraically tedious, and so the result is stated without proof [59]

$$\mathcal{V}^{\mathrm{ss}}(\boldsymbol{r}) = -\alpha^2 E_h \left(\frac{a_0}{r}\right)^3 \sqrt{\frac{4\pi}{5}} \sum_{\mu=-2}^{2} (-1)^{\mu} Y_{2,-\mu}(\hat{\boldsymbol{r}}) \Sigma_{2,\mu}. \tag{2.42}$$

Here the operators $\Sigma_{2,\mu}$ are given by

$$\Sigma_{2,\pm 2} = \frac{1}{\hbar^2} \sqrt{\frac{3}{2}} s_{1,\pm} s_{2,\pm}, \tag{2.43}$$

$$\Sigma_{2,0} = \frac{1}{\hbar^2} \left[2 s_{1,z} s_{2,z} - \frac{1}{2}(s_{1,+} s_{2,-} + s_{1,-} s_{2,+}) \right], \tag{2.44}$$

and,

$$\Sigma_{2,\pm 1} = \mp \frac{1}{\hbar^2} \sqrt{\frac{3}{2}} (s_{1,\pm} s_{2,z} + s_{1,z} s_{2,\pm}), \tag{2.45}$$

where $s_{i,+(-)}$ is the raising (lowering) ladder operator acting on the spin of atom i.

It is useful to consider how the anisotropic nature of eq. (2.42) leads to coupling of different partial waves. The relevant matrix element with

$$|\alpha, l, m_l\rangle = |s_1, m_{s1}, s_2, m_{s2}, l, m_l\rangle, \tag{2.46}$$

and,

$$|\alpha', l', m_l'\rangle = |s_1', m_{s1}', s_2', m_{s2}', l', m_l'\rangle \tag{2.47}$$

is given by

$$\begin{aligned}\langle \alpha, l, m_l|\mathcal{V}^{\rm ss}(\boldsymbol{r})|\alpha', l', m_l'\rangle = &-\alpha^2 E_h \left(\frac{a_0}{r}\right)^3 \sqrt{\frac{2l'+1}{2l+1}}(-1)^{m_l'-m_l}\ldots \\ &\langle l', 0; 2, 0|l, 0\rangle\langle l', m_l'; 2, m_l - m_l'|l, m_l\rangle\ldots \\ &\langle \alpha|\Sigma_{2,m_l'-m_l}|\alpha'\rangle. \end{aligned}\tag{2.48}$$

The middle line of this expression contains Clebsch-Gordan coefficients for the coupling of angular momentum j_1 and j_2 to form J, $\langle j_1, m_{j1}; j_2, m_{j2}|J, M_J\rangle$. For completeness we note that

$$\langle \alpha|\Sigma_{2,\pm 2}|\alpha'\rangle = \sqrt{\frac{3}{2}}\,\delta_{m_{s1}',\mp 1/2}\,\delta_{m_{s1},\pm 1/2}\,\delta_{m_{s2}',\mp 1/2}\,\delta_{m_{s2},\pm 1/2}, \tag{2.49}$$

$$\begin{aligned}\langle \alpha|\Sigma_{2,\pm 1}|\alpha'\rangle = \mp\sqrt{\frac{3}{2}}\Big(&\delta_{m_{s1}',\mp 1/2}\,\delta_{m_{s1},\pm 1/2}\,\delta_{m_{s2}',m_{s2}}\,m_{s2} + \ldots \\ &\delta_{m_{s2}',\mp 1/2}\,\delta_{m_{s2},\pm 1/2}\,\delta_{m_{s1}',m_{s1}}\,m_{s1}\Big),\end{aligned}\tag{2.50}$$

and,

$$\begin{aligned}\langle \alpha|\Sigma_{2,0}|\alpha'\rangle = &2\delta_{m_{s1}',m_{s1}}\delta_{m_{s2}',m_{s2}}m_{s1}m_{s2} - \ldots \\ &\frac{1}{2}\Big(\delta_{m_{s1}',-1/2}\,\delta_{m_{s1},1/2}\,\delta_{m_{s2}',1/2}\,\delta_{m_{s2},-1/2} + \ldots \\ &\delta_{m_{s1}',1/2}\,\delta_{m_{s1},-1/2}\,\delta_{m_{s2}',-1/2}\,\delta_{m_{s2},1/2}\Big).\end{aligned}\tag{2.51}$$

As can be seen from the Clebsch-Gordan factors in eq. (2.48) this term is non-diagonal in l, and so couples partial waves. It has no contribution when considering only s-wave collisions. It has diagonal contributions when considering higher partial waves and so for these cases the $\mathcal{V}^{\rm ss}(\boldsymbol{r}) \propto \alpha^2/r^3$ term replaces C_6/r^6 as the most long range part of the spatially dependent interaction. The off diagonal terms couple partial waves that

differ by two units of angular momentum, for example, s-waves are coupled to $l = 2$ d-waves which are in turn coupled to $l = 4$ g-waves so on and so forth. Even though $\mathcal{V}^{\mathrm{ss}}$ is in general much weaker than the other contributions, it can sometimes have a significant effect. For example, it can provide decay channels to collisions that would otherwise be completely elastic.

3

Feshbach resonances in Potassium-40

3.1 Introduction

Since first being used to form a degenerate Fermi gas [9] experiments using ^{40}K have explored a wealth of ultracold physics. A crucial experimental achievement was the discovery of a magnetically tuneable Feshbach resonance in ^{40}K [10], which led to the formation of a molecular BEC [11], and the creation of an ultracold gas of polar molecules [12]. In optical lattices a Mott insulator of fermionic atoms was demonstrated [14], which provides insights into the fermionic Hubbard Hamiltonian [16]. In addition, experiments probing a strongly interacting gas in the BCS-BEC crossover regime have been carried out [15]. Several studies involving resonant collisions and molecular formation provided by Feshbach resonances have been performed using mixtures of ^{40}K with other species such as: ^{87}Rb [17, 18, 19, 20, 21, 22, 23, 24], and ^{6}Li [25].

When a magnetic field B is present, we can define a collisional entrance channel in terms of the energy eigenstates of the asymptotically separated atoms as shown in fig. (3.1). The ^{40}K single atom energy levels of the electronic ground state are shown as a function of magnetic field. The states are labelled alphabetically, a to r, in order of increasing energy. An important feature specific to ^{40}K is the inverted hyperfine structure [60]. This has important consequences for spin-exchange relaxation in the presence of a magnetic field. Of the 55 different binary mixtures possible using the lowest hyperfine manifold, as many as 17 are stable against spin-exchange relaxation

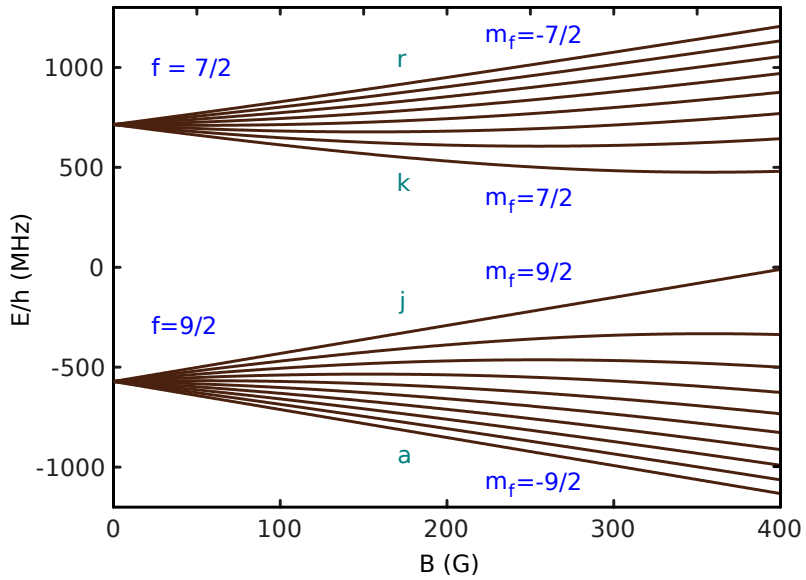

Figure 3.1: The energy eigenvalues of the single ^{40}K atom Zeeman and hyperfine Hamiltonian H_1 as a function of applied magnetic field (10^4 G = 1 T). We label the states from a to r in order of increasing energy. Also shown are the f and m_f quantum numbers that these states correspond to. The inverted nature of the hyperfine splitting was first reported in [60], atomic data is taken from [64]. An entrance channel labeled as ab, for example, would correspond to a collision with the atoms initially in a state with appropriate symmetry, containing one atom in state a and one in state b [28].

in the zero temperature limit. These include all combinations with atoms in adjacent hyperfine states. Furthermore, these also include all binary mixtures with atoms in hyperfine states differing by two units of angular momentum because all exit channels are forbidden either energetically or by the Pauli principle. Of the 17 s-wave channels stable against spin-exchange, only the ab mixture is fully stable. The lifetime of all other binary mixtures is limited by magnetic dipole-dipole relaxation. Thus far, the observation of Feshbach resonances has been reported for the ab, bb, and ac channels [10, 61, 62, 63]. The large variety of mixtures stable against spin exchange stimulated us to make a broader exploration of Feshbach resonances in ^{40}K.

It is possible, using the coupled channels (CC) method [59], to make quantitative

predictions regarding the properties of these resonances. However this requires detailed knowledge of the singlet and triplet Born-Oppenheimer (BO) potentials [57]. The combination of calculation with experiment allows the fine tuning of BO models, and adds credibility to the parameterisation and further prediction of atomic scattering processes.

Given reliable BO potentials the CC approach results in a set of coupled differential equations that can be computationally expensive to solve. Motivated by this simple models such as the Multichannel Quantum Defect Theory three parameter model (MQDT) [65] and the Asymptotic Boundstate Model (ABM) [66] are of interest.

In this chapter we explore Feshbach resonances in homonuclear mixtures of the fermionic quantum gas ^{40}K by performing coupled channels calculations. Our results are compared with newly measured positions of resonances (B_0). They are shown to agree well with our theoretical results based on the best available Born-Oppenheimer potentials for potassium [67]. We discuss the experimental contributions of our collaborators and present the main results of this chapter in tables 3.1 and 3.2. We predicted a host of not previously observed resonances, of s-wave and p-wave character. Our coupled channels data is used in the further development of two simplified theoretical models. Developed for the exploration of Feshbach spectra in binary mixtures; we discuss the three parameter multichannel quantum defect theory (MQDT)[1] [65] and the asymptotic bound-state model (ABM)[2] [66]. We pay attention to the advantages and disadvantages of the simplified models and their respective performances are compared against the CC results.

3.2 Experiments

The experimental data in tables 3.1 and 3.2 was obtained using different experimental setups in groups from Amsterdam [A][3], Munich [M][4] (previously in Mainz) and Zurich [Z][5], which all determined the resonance field locations via loss measurements. Data marked with [A] was measured in a three-dimensional optical dipole trap by observing

[1] Calculations performed by the group of P. Julienne, NIST.
[2] Calculations performed by the group of S. Kokkelmans, Eindhoven University
[3] J. Walraven and coworkers, Universiteit van Amsterdam.
[4] I. Bloch and coworkers, LMU Munich
[5] T. Esslinger and coworkers, ETH Zürich

the spin-dependent loss of atoms versus magnetic field. Data marked with [M] or [Z] was extracted whilst using optical lattice arrangements. In Munich the width of the resonance, ΔB, was determined by investigating the crossover from ballistic to diffusive expansion in a blue-detuned optical lattice as a function of magnetic field [68]. In Zurich ΔB was measured by observing the dephasing of Bloch oscillations in a red-detuned optical lattice, as was previously demonstrated for the bosonic case in ref. [69]. More detailed accounts of the experiments are provided in appendix A.

3.3 Models

In this Section we discuss our coupled-channels (CC) caculation, which we used to accurately describe the diatomic near threshold physics for ultracold potassium atoms. The CC method allows for a precise characterisation of all the measured Feshbach resonances. The results are included in tables 3.1 and 3.2 for comparison with experiment. Additionally, the CC method is compared with two simplified models of resonance scattering: the asymptotic bound-state model (ABM) and multichannel quantum defect theory (MQDT). Our CC calculations allowed for the further development and comparison of these models. Each of these two approaches represents a different method for simplifying the problem of searching for and characterising Feshbach resonances and molecular states.

3.3.1 Coupled channels calculations

Numerical solution of the CC equations and specifically their application to cold gases have been discussed widely, for example see refs. [59, 73, 74, 75]. Here we give an overview of what is involved in solving the CC equations. As input for the newly written CC code, which was implemented in the MATLAB programming language, we use the Born-Oppenheimer (BO) potentials of ref. [76]. The combination of calculation and experiment showed that it was not necessary to fine tune these BO potentials, i.e. the BO potentials are accurate enough to properly describe the scattering of ultracold potassium atoms. The obtained numerical results are used to characterize atomic two body loss rates and resonance parameters, which are presented in tables 3.1 and 3.2. The inelastic collision rate in the vicinity of a resonance is also of interest as it is related to the longevity of an experiment.

		Experiment			CC				
Channel	M_T	B_0 [G]	ΔB [G]	Source	B_0 [G]	Δ [G]	a_{bg}/a_0	a_{res}/a_0	γ_b [mG]
ab	-8	202.10(7) [70]	7.0 ± 0.2 [M]; 7.5(1) [Z]	[70], M, Z	202.1	6.9	167.0	-	-
ac	-7	224.21(5)	9.7(6) [63]; 7.6(1) [Z]	[63], Z	224.2	7.2	167.3	1.8×10^{7}	0.068
bc	-6	174	7	[71]	174.3	7.9	183.5	4.6×10^{6}	0.32
bc	-6	228.8(4)		A	228.7	8.2	137.6	1.0×10^{6}	1.1
bd	-5	168.5(4)		M	169.1	1.0	184.8	9.5×10^{4}	2.0
bd	-5	260.3(6)		M	260.5	11.2	164.9	1.5×10^{6}	1.2
cd	-4	22.1(3)		A	22.44	6.5×10^{-2}	166.3	1.8×10^{3}	6.2
cd	-4	178(1)		A	178.3	8.7	185.6	1.8×10^{6}	0.90
cd	-4	254.8(9)		A	255.1	15.7	139.8	6.1×10^{5}	3.5
de	-2	37.2(3)		A	38.07	0.37	157.8	1.3×10^{3}	46
de	-2	102.1(1)		A	102.2	2.6×10^{-3}	169.2	2.8×10^{1}	16
de	-2	138.2(1)		A	138.2	0.15	176.6	1.3×10^{3}	2.0
de	-2	219.1(1)		A	219.7	1.7	208.0	7.3×10^{4}	4.8
de	-2	292.3(4)		A	292.7	27.5	150.9	9.4×10^{5}	4.4
ih	6	312(1.8)		A	312.4	6.6	129.9	1.5×10^{5}	5.6

Table 3.1: Observed s-wave Feshbach resonances with accompanying coupled-channels (CC) parameterisations. The letters A, M, and Z indicate a measurement performed by the Amsterdam, Mainz/ München, and ETH groups respectively. The CC parameterisations were obtained by fitting to eqs. (3.13,3.12), except for the ab channel where the scattering length is real and so the standard form $a_{\mathrm{bg}}[1-\Delta/(B-B_0)]$ is used. M_T is the total projection of angular momentum along the magnetic field axis, and is a conserved quantity during the collision. CC calculations were performed with an initial collision energy of $\mathrm{E}/k_{\mathrm{b}} = 1\,\mathrm{nk}$.

		Experiment		CC
Channel	M_T	B_0 [G]	Source	B_0 [G]
ac	-6,-8;-7	215(5)	M	215.0;216.1
bb	-6, -8	198.30(2)	[72]	198.4
bb	-7	198.80(5)	[72]	198.9
cc	-4,-6	232.8(2)/232.8(2)	Z/A	233.0
cc	-5	233.4(2)/233.6(2)	Z/A	233.6
cc	-5;-4,-6	245.3(5)/245.4(4)	M/A	245.3;245.0
cd	-4	262.6(2)	A	262.5
cd	-5,-3	262.2(2)	A	262.2
dd	-3;-2,-4	287(1.8)	A	287.6;286.7
dd	-3;-2,-4	311.8(4)	A	311.7;311.5
de	-2;-1,-3	338(1.8)	A	338.4;338.1
ee	-1;0,-2	373(1.8)	A	373.7;372.7
hh	5;4;6	68(1.8)	A	67.4;68.8;67.6
hh	5;4;6	102(1.8)	A	101.0;100.6;100.3
hh	5;4;6	139(1.8)	A	137.9;136.0;136.4
hh	5;4,6	324(1.8)	A	324.1;323.0
hj	7;6;8	44(1.8)	A	44.6;43.4;44.1
ii	7;6	43.8(2)	A	43.5;43.6
ii	7;8	44.7(2)	A	44.9;44.3
ii	6	45.2(2)	A	45.3
ii	7	46.4(2)	A	46.4

Table 3.2: Observed *p*-wave Feshbach resonances with accompanying coupled-channels (CC) parameterisations. The letters A, M, and Z indicate a measurement performed by the Amsterdam, Mainz/ München, and ETH groups respectively. M_T the total projection of angular momentum along the magnetic field axis. For each collision channel M_T can take on three values corresponding to different projections of the orbital angular momentum quantum number $m_l = 0, \pm 1$. CC calculations were performed at a collision energy of $\mathrm{E}/k_\mathrm{b} = 1\,\mu\mathrm{k}$. This accounts for the discrepancy with the *bb* resonance positions given in ref. [72], where effort was made to account for temperature dependence.

In the center of mass frame [55] the Hamiltonian for two alkali metal atoms in the presence of a magnetic field, is given by

$$\mathcal{H} = \frac{\mathbf{p^2}}{2\mu} + \mathcal{H}^{\text{int}} + \mathcal{V} + \mathcal{V}^{\text{ss}}, \tag{3.1}$$

where the first term represents the relative kinetic energy, with μ being the reduced mass. The Zeeman and hyperfine interactions of the two atoms sum to give $\mathcal{H}^{\text{int}}$, which is determined by

$$\mathcal{H}^{\text{int}} = \sum_{j=1}^{2} \left[\frac{C_{\text{hf}}}{\hbar^2} \mathbf{s}_j \cdot \mathbf{i}_j + \mu_{\text{B}} (g_{\text{e}} \mathbf{s}_j + g_{\text{n}} \mathbf{i}_j) \cdot \mathbf{B} \right]. \tag{3.2}$$

The hyperfine constant C_{hf} gives the magnitude of the hyperfine splitting as seen in fig. 3.1. Similar to chap. 2, $\mathbf{i}_j$, $\mathbf{s}_j$, μ_{B}, g_{n}, g_{e} are the nuclear spin of atom j, valence electron spin of atom j, Bohr magneton, nuclear g-factor, and electronic g-factor respectively. The term $\mathcal{V} = \mathcal{P}_{\text{s}} V_{\text{s}} + \mathcal{P}_{\text{t}} V_{\text{t}}$ includes the singlet V_{s} and triplet V_{t} BO potentials [76] with the operators $\mathcal{P}_{\text{s}}$ and $\mathcal{P}_{\text{t}}$ projecting out the singlet and triplet components of the wave function respectively. The spin-spin dipolar interaction is again described by

$$\mathcal{V}^{\text{ss}} = \frac{\alpha^2 E_{\text{h}} a_0^3}{\hbar^2 r^3} \left[\mathbf{s}_1 \cdot \mathbf{s}_2 - 3(\mathbf{s}_1 \cdot \hat{\mathbf{r}})(\mathbf{s}_2 \cdot \hat{\mathbf{r}}) \right], \tag{3.3}$$

which is the long range approximation to the interaction between the magnetic moments of the outer shell electrons belonging to each of the alkali metal atoms, as discussed in ref.[59].

Starting from the rigorous multichannel scattering theory it is possible to derive the following coupled-channels equations in the close coupling approximation [55, 56]. Expressing the wave function in terms of the N channel states $|\alpha_m\rangle$, that diagonalize the Hamiltonian $\mathcal{H}^{\text{int}}$, have the correct symmetry, and project out the relevant partial waves, as $\sum_{m=1}^{N} |\alpha_m\rangle \psi_m(r)/r$, we have the series of N coupled equations

$$\frac{\partial^2 \psi_m}{\partial r^2} = \frac{2\mu}{\hbar^2} \sum_{n=1}^{N} \left[W_{m,n}(r) + \mathcal{V}^{\text{ss}}_{m,n} - E\delta_{m,n} \right] \psi_n(r), \tag{3.4}$$

where $\delta_{m,n}$ is the Kronecker delta and

$$W_{m,n}(r) = \delta_{m,n} \left[E_m + \frac{\hbar^2}{2\mu} \frac{l_m(l_m+1)}{r^2} \right] + \mathrm{V}_{m,n}. \tag{3.5}$$

Here E_m is the eigen-energy of the internal Hamiltonian $\mathcal{H}^{\text{int}}$, and l_m is the relative orbital angular momentum quantum number of the state $|\alpha_m\rangle$. The subscripts m, n indicate that the operator appears between $\langle\alpha_m|$ and $|\alpha_n\rangle$. For example, $V_{m,n} = \langle\alpha_m|V|\alpha_n\rangle$. It is useful to rewrite this set of equations in the N-by-N matrix form

$$\boldsymbol{\Psi}''(r) = [\boldsymbol{Q}(r) + \boldsymbol{\mathcal{V}}^{\mathbf{ss}}(r)]\,\boldsymbol{\Psi}(r), \tag{3.6}$$

where the elements of the matrix $\boldsymbol{Q}(r)$ are given by $(2\mu/\hbar^2)[W_{m,n}(r) - E\delta_{m,n}]$. Considering the scattering boundary condition (taking $r \to \infty$), $[\boldsymbol{\Psi}]_{\{1,\ldots,N\},n}$ can be interpreted as being the scattering wave function with an incoming wave in channel n. In practice, rather than propagating the wave function and derivative matrices to large r, we instead propagate the log-derivative matrix, $\mathbf{Y} = \boldsymbol{\Psi}'[\boldsymbol{\Psi}]^{-1}$, using the technique of Manolopoulos [77]. From this a multichannel S-matrix can be extracted via [55]

$$\mathbf{S}(r) = \left[\mathbf{h}'^{+}(r) - \mathbf{Y}(r)\mathbf{h}^{+}(r)\right]^{-1}\left[\mathbf{h}'^{-}(r) - \mathbf{Y}(r)\mathbf{h}^{-}(r)\right], \tag{3.7}$$

where $\mathbf{h}^{+}(r)$, $\mathbf{h}'^{+}(r)$, $\mathbf{h}^{-}(r)$, and $\mathbf{h}'^{-}(r)$ are diagonal matrices mainly constructed from Riccati-Hankel functions [55]. For non-s-wave entrance channels the numerical propagation becomes difficult at low collision energies. We find it necessary to use a long range approximate correction to the S-matrix, given by [59]

$$\mathbf{S}(\infty) \approx \mathbf{S}(r_1) - \frac{\mu i}{\hbar^2}\int_{r_1}^{\infty}\left[\mathbf{h}^{-}(r) + \mathbf{S}(r_1)\mathbf{h}^{+}(r)\right]\mathcal{V}^{\text{ss}}(r)\left[\mathbf{h}^{-}(r) + \mathbf{h}^{+}(r)\mathbf{S}(r_1)\right]\,\mathrm{d}r, \tag{3.8}$$

in order to greatly increase the rate of convergence. This expression assumes that the endpoint of the numerical propagation, r_1, is large enough to neglect contributions from $\mathcal{V}$, which fall of as r^{-6}. The integration in this expression is performed analytically, and only includes open channels.

Although we have thus far formulated the problem using $|\alpha_i\rangle$, it is also useful to employ an alternative set of angular momentum states. In the inner region, where the singlet and triplet potentials are dominant, we use a basis in which i_1 and i_2 are coupled to give I, and s_1 and s_2 are coupled to give S. This has the advantage of the BO contribution $\mathcal{V}$ being diagonal. We transform to the basis states $|\alpha_i\rangle$ at the point where $|V_S - V_T|$ is comparable with the hyperfine coupling. From this point onwards $\mathcal{V}$ is approximately diagonal in both representations. Once an S-matrix has been evaluated one can extract the s-wave scattering length by defining the phase shift $\delta(E)$, related to the element of the S-matrix $[\mathbf{S}]_{\text{e,e}} = \exp[2i\delta(E)]$, with e indicating

the entrance channel. If the entrance channel is the only open channel the scattering length is given by the limit

$$a = \lim_{k\to 0} \frac{-\tan[\delta(E)]}{k}. \tag{3.9}$$

This can be generalised to the case where the scattering is not purely elastic, i.e., there is more than one open channel. Here the complex scattering length $\tilde{a}$ and complex phase shift $\delta(E)$ are now related by

$$\tilde{a} = a - bi = \lim_{k\to 0} \frac{-\tan[\delta(E)]}{k}. \tag{3.10}$$

It can be shown [78, 79, 80, 81] that in the vicinity of a Feshbach resonance the following parameterization is valid

$$a(B) = a_{\mathrm{bg}} \left(1 - \frac{\Delta B(B - B_0)}{(B - B_0)^2 + (\gamma_{\mathrm{B}}/2)^2}\right), \tag{3.11}$$

$$b(B) = 2a_{\mathrm{res}} \frac{(\gamma_{\mathrm{B}}/2)^2}{(B - B_0)^2 + (\gamma_{\mathrm{B}}/2)^2}. \tag{3.12}$$

In the absence of decay we have $\gamma_{\mathrm{B}} = 0$, and we of course recover

$$a(B) = a_{\mathrm{bg}} \left(1 - \frac{\Delta B}{B - B_0}\right). \tag{3.13}$$

In these expressions, a_{bg} is the background scattering length, representing the scattering length of the entrance channel in the absence of a resonance. We have expressed the decay rate of the bound state, γ, in magnetic field units, $\gamma_{\mathrm{B}} = \hbar\gamma/\mu_{\mathrm{res}}$, where μ_{res} is the difference in magnetic moment between the entrance channel and the bound state causing the resonance. The resonance length a_{res} is defined by $a_{\mathrm{res}}\gamma_{\mathrm{B}} = a_{\mathrm{bg}}\Delta B$ and gives an indication of how much a varies across the resonance, and of the peak loss rate. The width and magnetic field location of the resonance are given by ΔB and B_0, respectively. The absolute value of this scattering length is the appropriate parameter to describe the elastic scattering process, while the imaginary part can be used to describe the inelastic collision rate coefficient [28]

$$K_2(B) = \frac{4\pi\hbar}{\mu} b(B). \tag{3.14}$$

In the limit of zero collisional energy this rate has its peak exactly on resonance, where it equals $K_2(B_0) = 4ha_{\mathrm{res}}/\mu$. For partial densities n_α and n_β the total decay rate of component α is given by $-\dot{n}_\alpha/n_\alpha = K_2 n_\beta + \tau_{\mathrm{vac}}^{-1}$ where τ_{vac} is the vacuum lifetime.

Some results of the CC calculations showing the real and imaginary components $a(B)$ and $b(B)$ for the de mixture are shown in fig. 3.2, where they can be compared to experimental findings. For all observed s-wave resonances the calculated values for B_0, ΔB, $a_{\rm bg}$, $a_{\rm res}$, γ_b and $\mu_{\rm res}$ are tabulated. The positions B_0 for a number of p-wave resonances are also presented.

The bound state calculations are performed as in ref. [74]. They involve numerical methods similar to those used for the scattering calculations. However the asymptotic $r \to \infty$ boundary condition on $\mathbf{\Psi}(r)$ now requires that all elements decay suitably to zero. The term $\boldsymbol{\mathcal{V}}^{\mathbf{ss}}$ is neglected in the bound state calculations because they are used for comparison to the MQDT and the ABM (see fig. 3.4), neither of which include this term. We propagate $\mathbf{Y}(r)$ from small r outwards to some matching point R, which we call $\mathbf{Y}_a$. We then propagate from large r inwards to R which we call $\mathbf{Y}_b$. It can be shown [74] that a bound state exists if the matching matrix,

$$\mathbf{M}(E) = \mathbf{Y}_a(E) - \mathbf{Y}_b(E), \tag{3.15}$$

has an eigenvalue equal to 0.

3.3.2 Multichannel quantum defect theory

Implemented here by the NIST group, the MQDT is motivated by the differential equation formulation of scattering theory [55]. It incorporates simplifying assumptions based on the separation of scale between the kinetic energy of the colliding atoms and the depth of the interatomic potential. The effect of the deep part of the potential is represented by applying a boundary condition on the wave function solution at short range. The boundary condition can be determined using the singlet and triplet scattering lengths [82]. At larger internuclear separations the analytical solutions to the radial Schrödinger equation with a $-C_6/r^6$ potential are used (see ref. [82] and references therein). The short range boundary condition determines the relative admixture of the two linearly independent solutions to the radial Schödinger equation. This allows scattering and bound state properties to be predicted based on just three parameters describing the interactions: the scattering lengths of the singlet (a_s) and triplet (a_t) potentials and the dispersion coefficient C_6. The computational effort of propagating either the wave function or its log-derivative to large distances, as was necessary with our CC calculations, is entirely avoided.

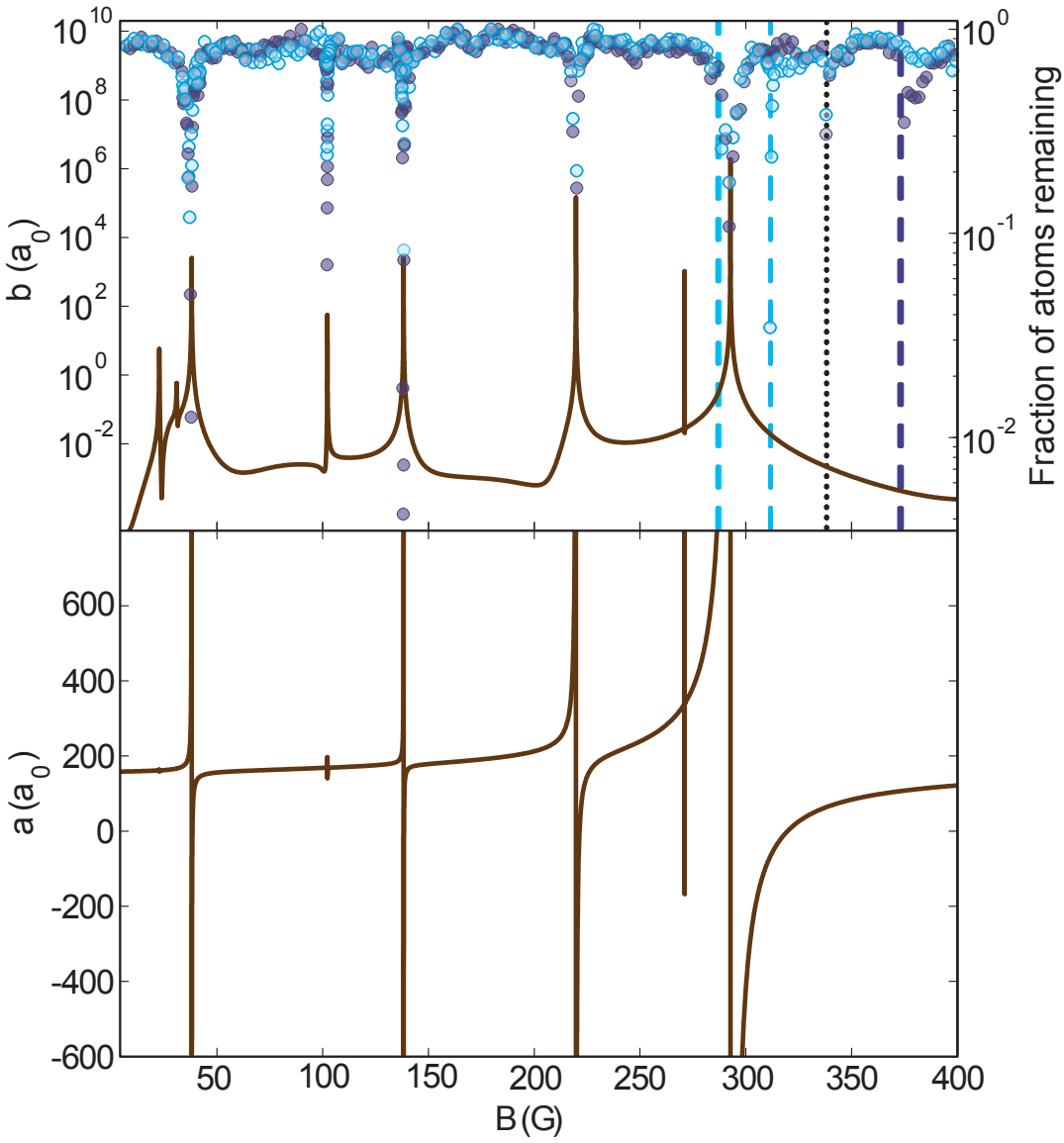

Figure 3.2: Upper plot, right *y*-axis: Observation of ^{40}K Feshbach resonances by loss spectroscopy with atoms in the d and e states. Circles denote atoms remaining in the trap after the cloud had been held in the trap for 3 s in the presence of a homogenous magnetic field of strength B. Light blue circles denote atoms in the d state and dark blue circles denote atoms in the e state. **Left *y*-axis:** the solid line is the imaginary part of the scattering length and is proportional to the inelastic collision rate coefficient. The vertical lines indicate the positions of some p-wave resonances. With the light blue dashed being in the dd channel, black dotted the de channel, and dark blue dashed the ee channel. **Lower plot:** the solid line shows the real part of the scattering length.

This model has been previously applied to calculations in the presence of a magnetic field [65] and RF radiation [83, 84]. In the present work, an MQDT search over all possible collision channels was used as a guide for the CC calculations which are more time consuming. If the singlet and triplet scattering lengths are allowed to vary slightly from their actual values then the agreement between the MQDT and CC calculations can be improved. This can be done for a few resonances and then the scan can be re-performed to offer generally better predictions. This fine-tuning can be seen as adjusting the pseudo-interaction experienced at small internuclear separations.

3.3.3 Asymptotic bound state model

The ABM [66] uses bound states in an approximate expansion of the channel Hamiltonians in the singlet and triplet basis. This is then used to estimate Feshbach resonance positions and widths. This approach involves calculation of overlap integrals (which are treated approximately, or can be used as fitting parameters), and the use of simple matrix operations. With this method as with the MQDT, no numerical propagation of differential equations is necessary. Again, here it is sufficient to use as inputs a_s, a_t and C_6. Binding energies, ϵ_ν^S, are calculated using the accumulated phase method [85]. This also yields the overlap parameters $\langle\psi_{\nu'}^{S'}|\psi_\nu^S\rangle$, where ν, and ν' range over all contributing bound states of the singlet and triplet potentials. Here ν is counted from the dissociation limit, i.e. $\nu = -1$ is the least bound state. The ABM has been previously used to study magnetically tuneable Feshbach resonances [25, 86, 87, 88, 89, 90, 91].

For this project the Eindhoven group adapted their methods to allow the study of systems with large background scattering lengths. The problem arises when the background channel supports a very weakly bound state. In this case ($a_{\mathrm{bg}} \gg r_0$) where the range of the interaction potential is characterised by r_0. The simple expansion of the singlet and triplet Hamiltonians in bound states alone does not account for the now non-negligible coupling to the continuum states. To allow for this effect, the coupling between the weakest bound states is allowed to vary with magnetic field strength. The resulting magnetic field dependent overlap $\langle\psi^0_{-1}|\psi^1_{-1}\rangle(B)$ is determined in a manner consistent with the degenerate internal states (DIS) approximation [59]. Note that the variation of the overlap parameter is a few percent, which corresponds to a shift of ϵ_{bg} of a few MHz.

3.4 Coupled channels predictions and experimental realisation

The theoretical modelling and experimental investigation did not take place in isolation. The coupled channels predictions played a major part in guiding the experiments and helping to interpret the results. Since ^{40}K is unusually complicated by virtue of its large nuclear spin, it is often difficult to unpick which states are responsible for which experimentally observed features. For example, neglecting V^{ss}, ii has no two-body loss channels. On the other hand, V^{ss} couples ii ($m_F = 7$) to $m_F = 5, 6, 8$, and 9 depending on the change of m_l during the collision. Relevant thresholds that are energetically lower than the ii threshold are the ih and hh, see fig. 3.3. In the figure we see that if one neglects V^{ss} then the only p-wave bound state crossing the threshold is the blue one of ii character. Hence there would be only one ii Feshbach resonance for this entrance channel and magnetic field range. Including V^{ss} now couples the i+i channel to the other channels shown in the figure. For example if the i+i collides with $l = 1$ and $m_l = 0$, it can couple to the bound states/closed channel states with spin character ih and ij, whilst still preserving $m_T = m_l + m_F$. It can be seen that this now results in 4 states crossing the i+i threshold. Similarly the ii, $l = 1$, $m_l = +1$ combination will involve ii, ij and jj, giving 2 states crossing. The ij and jj are thresholds that are higher in energy than the ii, and so these collisions have no loss channels even including V^{ss}. Finally the ii, $l = 1$, and $m_l = -1$ combination involves ii, ih, and hh resulting in 4 crossings. Whether each of these are experimentally resolvable depends on the strength of the coupling and the magnetic field accuracy available to the experimentalist.

A further problem may arise when one is reliant on atom loss measurements – not all inelastic processes lead directly to atom loss. In the jh channel a p-wave resonance with decay to the ii channel in which the atoms remain optically trapped is observed. The energy released in the collision is less than the depth of the trap, and so the gas is heated but without associated atom loss (from two body collisions). This is due to the small energy difference between the ii and jh thresholds. This was observed in the imaging process as atoms being transferred from all being in the ii state, to being in a mixture of j and h states.

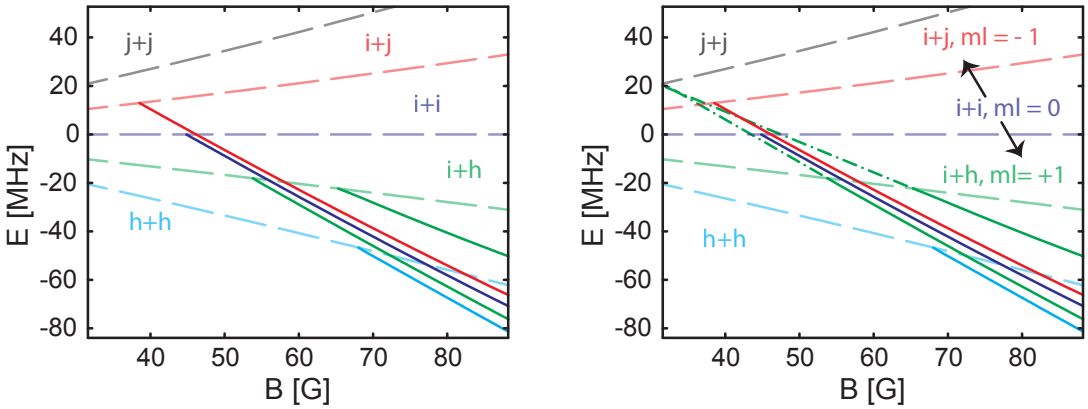

Figure 3.3: Bound states (p-wave) and scattering thresholds for $m_F = 5$ (cyan), 6 (green) 7 (blue) , 8 (red), and 9 (black). Dashed lines are the scattering thresholds, solid lines are bound states existing beneath a corresponding threshold, dash-dot lines are linear extrapolations of those bound states representing the closed channel state responsible for the bound state where energetically allowed. Left: In the absence of the electron spin-spin dipolar V^{ss} interaction the only bound state relevant to the scattering of atoms in the ii combination is represented by the blue line. Including the V^{ss} couples together these states, depending on the m_l projections. Right: If the atoms collide with incoming combination ii, p-wave, with $m_l = 0$, then the black arrows indicate the couplings that take place. All of these states have $m_l + m_F = 7$.

Nevertheless, a glance at tables 3.1 and 3.2 will show that there is fully acceptable agreement between the theoretical predictions and the outcome of the experiments. This holds for both s- and p-wave resonances. The main point to be derived from this, as far as we are concerned, is the implication that our model is extremely accurate. This gives rise to characterisations that we can consider to be good guides to the properties of Feshbach resonances. This may provide a reference for those experimentalists seeking to devise future experiments taking advantage of particular resonance qualities.

3.5 Comparison of MQDT and ABM to the rigorous CC calculations

A detailed comparison of the simpler models with our CC data reveals that they perform impressively given the extreme simplifications involved. We compare the results of the

two models to the results of the CC calculation in tables 3.3 and 3.4, and in fig. 3.4. We compare the success of the models when the inputs consist of just physical parameters, the singlet and triplet scattering lengths and the C_6 coefficient, and also the case where the inputs are allowed to float slightly, taking into account previous knowledge of the system. Sometimes Feshbach resonance positions may be known empirically in advance. For the purposes of comparison here, the calculations are optimised to reproduce the CC calculations.

The results obtained by using physical parameters are shown in the middle columns of table 3.3. MQDT has the slightly higher rms deviation from the CC results compared to the ABM, consistently producing B_0 values that are too low. As the qualitative agreement is good for both models, they can both be used for guiding more accurate coupled channels calculations, particularly in cases where detailed sweeps over many possible entrance channel configurations may be prohibitively slow.

When the parameters, a_s and a_t, were allowed to float slightly the MQDT approach produces a significantly lower rms deviation from the CC results compared to the ABM. To compound this, here 8 free parameters are used in the ABM optimisation. For the ABM s- and p-wave fits the most relevant overlap parameters were $\langle\phi^0_{-1}|\phi^1_{-2}\rangle$ and $\langle\phi^0_{-2}|\phi^0_{-2}\rangle$, respectively. Both of these elements involve the $\nu = -2$ states. Despite the simplification of neglecting scattering states, good qualitative agreement is obtained for the resonance widths with the ABM. With the approach of MQDT, which handles scattering more naturally, good qualitative agreement with the CC results is obtained. However, quantitatively we find that the MQDT and the ABM are limited in their accuracy for predicting the widths of Feshbach resonances. Resonance widths depend on the difference between the singlet and triplet potentials, which both theories only include crudely by assigning each potential the appropriate scattering length.

Next we consider molecular bound-state manifolds obtained via MQDT and ABM and compare these to CC calculations. We consider the s-wave *de* channel which, within the range of 0 G to 300 G, contains 7 resonances. Two of these resonances were too narrow to be observed experimentally. As this channel contains both wide and narrow resonances, it is a good test bed for the simplified models. The results of the comparison, where we used the optimised parameters as input, are shown in fig. 3.4. With the MQDT it is difficult to reproduce the lower field resonances as these result from deeper bound states belonging to an energetically higher collision threshold. The

deeply bound states are sensitive to the non-C_6 part of the interaction. The ABM has difficulty reproducing the highest field resonance as the threshold effects become strong in this instance. These threshold effects can be incorporated [66] to produce better results for the wide resonance, as can be seen in the inset of fig. 3.4. However these additions to the model are, in my view, unappealing since at some point it has to considered no longer simple.

3.6 Concluding remarks

We have presented a detailed study on the rich Feshbach resonance structure of ^{40}K. Excellent agreement is found for a range of resonances (both s-waves and p-waves) between the CC calculations and measurements, many of which were experimentally observed for the first time. We have characterised the resonances so that different qualities can be taken advantage of using the same atomic combination. For example if the zero crossing of the scattering length, at $B = B_0 + \Delta B$ is important, one may choose to use the *cd* entrance channel 178 G resonance. It is an isolated s-wave resonance with 55 G separating it from the next nearest resonance, as compared to a width of 8.7 G. Comparison of the CC calculations with the experimental observations shows that the currently available BO potentials [67], which are used as input for the CC calculations, are sufficiently accurate to predict the positions and widths of all studied resonances. This provides confidence that, with these BO potentials, the CC method can be used to reliably model ultracold collisions of potassium atoms. A fact that we will make use of in our more advanced studies in later chapters.

In addition we compared the performance of the MQDT and the ABM as two valuable simplified models which cannot be seen as competing with the CC method. The MQDT is based on a simplified application of boundary conditions to the asymptotic form of the solutions to the radial Schrödinger equation, while the ABM is based on an expansion of the Hamiltonian in terms of bound states. Both models can be based on three parameters. They are able to reproduce the scattering and bound state properties of ^{40}K atom pairs quite well. In particular the prediction of the resonance positions is fairly accurate. While MQDT gives the better optimised fit, the ABM performs slightly better with the physical input parameters. It should also be noted that most of the ABM results here used more than 3 free parameters, whilst the MQDT did not use

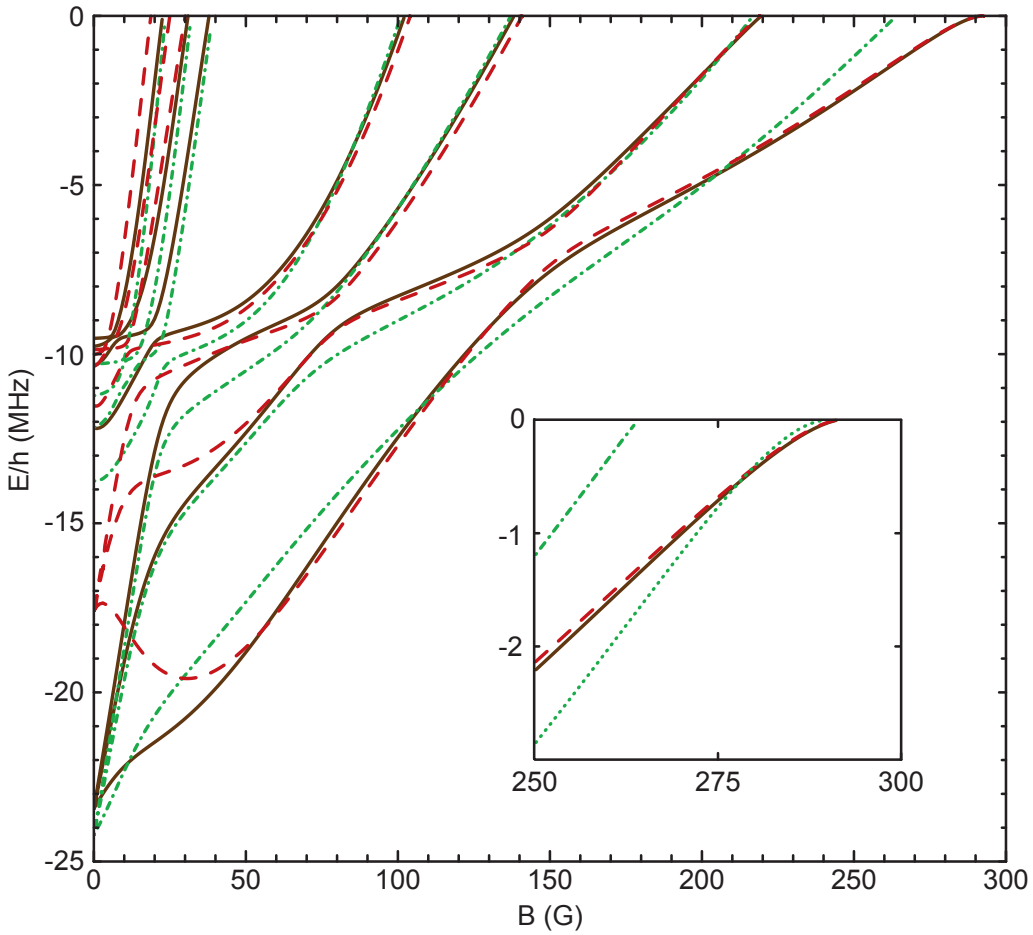

Figure 3.4: (Color online) Energy spectrum of s-wave molecular levels of ^{40}K in the *de* channel, as a function of magnetic field. Energies are given relative to the *de* threshold. The binding energies were obtained using: the CC method (black line), MQDT (red dashed line), and ABM (green dot-dashed line). The inset shows the binding energies near the broad resonance around $B \approx 290$ G. For the MQDT and ABM the optimized parameters were used as input. The results for ABM are shown without the dressing of the bound state [66], except in the inset (green dotted line).

any additional parameters. As both simplified methods do not account properly for the exchange energy, the predictions for the resonance width correspond only qualitatively to the CC results. The strengths and limitations of both models are illustrated by comparing the predicted resonance field positions and bound-state energy spectra with CC calculations. From a detailed study of the molecular bound-state manifolds of the *s*-wave *de* channel we conclude that both models performed equally well. The ABM shows a difficulty in handling resonances where strong threshold effects are involved. Whereas the MQDT has a handicap in cases when more deeply bound states are influential. Both the MQDT and the ABM proved to be useful for the qualitative exploration of the ^{40}K quantum gas, which is an example of a system with a large number of Feshbach resonances. For full characterisation, the more demanding CC calculations remain indispensable.

Channel	CC		Physical parameters MQDT		Physical parameters ABM		Optimised parameters MQDT		Optimised parameters ABM	
ab	202.1	6.9	187.1	7.3	205.8	4.7	201.2	7.1	207.1	6.8
ac	224.2	7.2	208.2	7.6	227.9 5.1	223.3	7.4	229.1	7.1	
bc	174.3	7.9	157.0	8.8	197.7	2.2	173.8	8.4	177.8	3.0
bd	169.1	1.0	156.9	1.5	181.3	0.3	171.9	1.3	169.3	0.6
bd	260.5	11.2	242.8	11.6	261.7	9.2	260.1	11.2	260.5	13.9
cd	22.44	0.065	2.7	0.001	26.4	8×10^{-6}	19.1	0.05	23.1	0.02
cd	178.3	8.7	157.5	11.0	219.9	1.7	177.7	9.8	185.9	3.0
cd	255.1	15.7	237.7	14.8	245.6	20.7	256.4	14.7	234.0	30.7
de	38.07	0.37	6.4	0.06	40.9	4×10^{-5}	32.9	0.3	39.5	0.1
de	102.24	0.0026	98.8	0.001	98.0	3×10^{-4}	105.45	0.003	101.0	2×10^{-4}
de	138.25	0.15	134.3	0.29	137.4	0.01	142.8	0.2	137.4	0.04
de	219.7	1.7	203.9	3.7	251.5	0.004	222.5	2.7	223.2	0.5
de	292.7	27.5	271.6	27	304.6	16.0	293.8	26.8	290.0	30.8
hi	312.4	6.6	300.5	6.9	317.9	0.9	310.7	6.8	321.7	3.1
σ_{RMS}(G):			17.4		16.4		2.6		6.9	

Table 3.3: Positions and widths of s-wave resonances obtained from coupled channels calculations (CC), multichannel quantum defect theory (MQDT) and the asymptotic bound state model (ABM). For the two simple models, results are given using the physical values of a_s , a_t and C_6 obtained from ref. [67], and for an optimisation to the CC data. The bottom row of the table gives the RMS deviations from the CC results, showing the extent to which the free parameters of each model offset the limitations of the simplifying assumptions made.

Channel	CC B_0 (G)	MQDT B_0 (G)	ABM B_0 (G)
ac	215.3700	222.7	229.4
bb	198.5800	200.0	203.1
cc	233.1800	235.9	231.2
cc	245.1300	246.2	247.7
cd	262.2800	263.6	258.9
dd	287.0	292.6	280.1
dd	311.6	312.0	311.2
de	338.1900	339.4	333.4
ee	373.0	380.5	365.9
hh	67.8200	73.8	65.6
hh	101.1700	79.2	94.0
hh	136.4600	119.7	136.5
hh	323.3700	320.1	336.5
hj	44.5700	48.1	43.3
ii	44.8	48.4	43.5
σ_{RMS}(G):		8.1	6.3

Table 3.4: Positions of several p-wave resonances, comparing MQDT and the ABM to CC results. The MQDT positions were calculated using the same fit derived for the s-wave resonances, while a separate ABM fit was performed. The value of σ_{RMS} is determined using the CC results without the dipole-dipole interaction.

4

Photodissociation of Potassium-40 Feshbach molecules

4.1 Introduction

Currently there is a great deal of attention focused on ultracold atomic gases in optical lattices. These experiments often hinge on the ability to manipulate the external potential as well as the interactions between individual atoms. Due to its anti-confining nature, it is often advantageous to use lattice light that is blue detuned from the relevant atomic transition, since this gives additional freedom in the manipulation of the overall confining potential. A disadvantage of blue-detuned light, however, is that colliding atoms can be electronically excited into states that allow them to escape the trap. These light induced inelastic collisions between two atoms on the same lattice site are one of the main heating sources in such a lattice experiment. In this work we systematically study the photodissociation of weakly bound Feshbach molecules by blue-detuned light. We can use the Feshbach molecules as a model system for two atoms on a lattice site, since the size of these weakly bound halo molecules is comparable to the mean distance between two atoms on a lattice site. This study in principle allows us to extract the best suited wavelength for a blue-detuned lattice. In addition we used it as a spectroscopic technique to extract information about the excited state potentials and refine the $B^1\Pi_u$ potential model.

On the one hand, the interaction between two ground state potassium atoms is now very well understood: In the previous chapter we used Born-Oppenheimer potentials

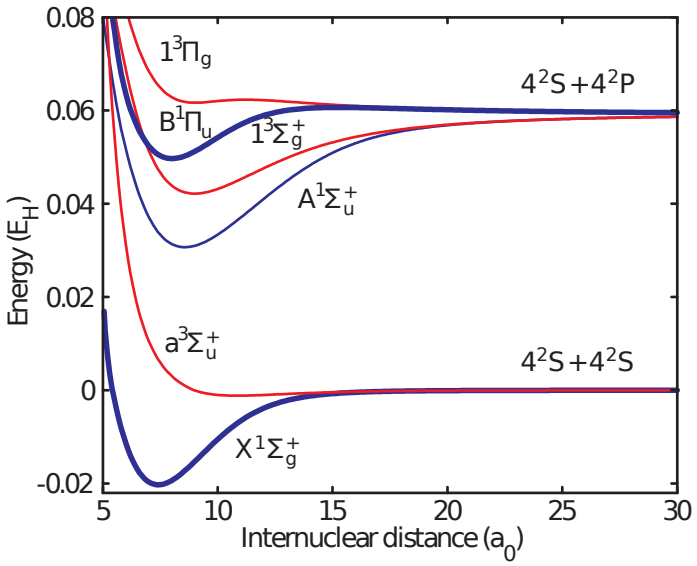

Figure 4.1: Molecular K_2 potential energy curves (in units of the Hartree energy, E_H) for the ground $a^3\Sigma_u^+$, $X^1\Sigma_g^+$ [76] states, *ab initio* curves for the $1^3\Pi_g$, $1^3\Sigma_g^+$, $A^1\Sigma_u^+$ states [103], and the $B^1\Pi_u$ curve which is constructed here. Their common $4^2S + 4^2S$ and $4^2S + 4^2P$ atomic asymptotes are also labeled. Dipole allowed transitions take place between the states who's potential energies are represented here (solid to solid, and dashed to dashed).

derived from molecular spectroscopy [76] to construct a coupled-channels model capable of accurately predicting the positions of a large number of magnetically tuneable Feshbach resonances. In the case of electronically excited states on the other hand, obtaining accurate potential energy models remains an important goal for molecular physics [92, 93, 94, 95, 96]. These potentials are needed to describe such processes as stimulated Raman adiabatic passage [97, 98, 99], optical Feshbach resonances [81, 100], and interactions between ultra-cold atoms and laser pulses in the femto-second regime [101, 102]. In particular, it has thus far been difficult to directly measure the shape of the $B^1\Pi_u$ potential barrier, see fig. 4.1, using conventional spectroscopic methods. Tunnelling rates of metastable states through the barrier have been studied [94] but this method requires a priori assumptions about the shape of the barrier, which may become invalidated if the knowledge of some aspect of the potential improves.

This chapter now continues with a description of the experimental procedure used to adiabatically associate Feshbach molecules, which were then dissociated with blue-

detuned laser light. Secondly, we offer a WKB analysis of photodissociation in the vicinity of a potential maximum. We then outline the theoretical techniques used to analyse the Feshbach molecule, and solve the Half-scattering photo-dissociation problem numerically. In conclusion we provide a detailed analysis of the structures observed in the photodissociation spectrum, allowing us to discern information relating to both the initial Feshbach molecule, and the $4^2\mathrm{S} + 4^2\mathrm{P}$ exit channel.

4.2 Experimental Procedure

In order to motivate our choice of theoretical model it is advantageous to have a clear picture of the experiment that was carried out by the Munich group[1]. The experimental sequence (shown in fig. 4.2) starts with an equal mixture of the $(|F, m_F\rangle)$ $|9/2, -9/2\rangle$ and $|9/2, -7/2\rangle$ hyperfine states, which was cooled to $T/T_F \approx 0.3$ at a magnetic field of $B \approx 219$ G in a pure dipole trap. Here the Fermi-temperature, T_F, is the Fermi-energy divided but the Boltzmann constant. This magnetic field strength corresponds to weakly repulsive interaction above the Feshbach resonance located at $B = 202.1$ G.

Approximately 60% of the atoms were converted into Feshbach molecules using an adiabatic ramp of the magnetic field down to 201 G [104]. After a short hold time ($\leq$10 ms) the molecules were converted back into atoms by a second magnetic field ramp and the atom number was measured using standard time of flight absorption imaging. By applying a blue-detuned light pulse during the hold time between the two magnetic field sweeps, a fraction of the molecules was photo-dissociated. In this sequence, the detected atom number consists of two parts: Atoms that were not converted into molecules by the first magnetic sweep (atomic background), and molecules that survived the laser pulse, were dissociated by the second magnetic sweep. Due to their high kinetic energy, atoms stemming from photo-dissociated molecules leave the trap immediately and are detected as a reduction of the final atom number. In addition, the atomic background was measured directly by skipping the second magnetic field ramp, since molecules remain invisible on absorption images taken with light resonant on the atomic transition.

[1]For detailed discussion of the experiment see the PhD thesis of Ulrich Schneider, who was working under the supervision of Immanuel Bloch.

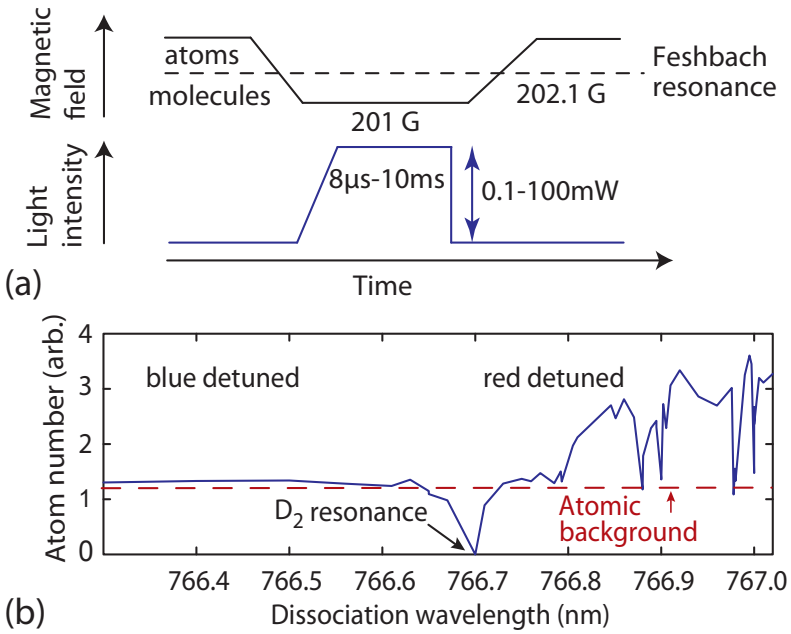

Figure 4.2: (a): Feshbach molecules are produced with an adiabatic magnetic field ramp over the Feshbach resonance at 202.1 G and after a hold time get dissociated by a second ramp in the opposite direction. During this hold time a light pulse of variable wavelength, intensity, and duration can photodissociate the molecules.
(b): Final atom number after the experimental sequence described in part (a). The intensities and durations of the photo-dissociation pulses were constant; only the wavelength was varied around the atomic D_2 transition at 766.7 nm.

4.3 Feshbach molecules in a laser field

This section is devoted to giving a description of our theoretical treatment of two interacting atoms in the field of a laser. We make clear where approximations are made and distinguish between ones made at the level of matter-light interactions, and at the level of the subsequent quantum mechanical scattering theory. We suppress most of the quantum numbers required to define all aspects of the wave function in order to present a clear account of the physical process taking place.

4.3.1 Blue and red laser detunings

An illustration of the stark difference between losses induced by blue and red detuned laser light is shown in fig. 4.2 (b). Here the remaining atom number following the experimental sequence shown in fig. 4.2 (a) is plotted as a function of of laser wavelength. Directly on the atomic resonance at 766.7 nm all atoms as well as all molecules are lost. For small detunings ($\leq$ 0.1 nm) around the resonance the remaining atom number quickly approaches a fixed value, the atomic background, which we attribute to atoms that have never been converted into molecules. For larger detunings ($>$ 0.1 nm), on the red detuned side of the atomic D_2 transition, the atom number rises further, except for sharp loss features that stem from narrow bound-bound transitions into bound molecular states in the excited potentials: the excitation of the molecule leads to further exothermic processes culminating in loss of the atoms from the trap. On the blue detuned side of the D_2 line, however, the Feshbach molecule can be excited into the continuum of scattering states. At asymptotically large internuclear separation these tend to the individual 4^2S and 4^2P atomic states. That is, after absorbing a photon the atoms are free to move apart before they decay back into the electronic ground state by spontaneously emitting a photon. In this process, they gain enough kinetic energy to escape their mutual short range attraction and (importantly for detection) the trap. The continuum nature of the final state is reflected by the observation that the atom number only starts to rise above the background level at much larger detunings (not shown here).

4.3.2 Coupling due to the laser field

When seeking to apply the results of scattering theory one usually starts with the time dependent Schrödinger equation

$$i\hbar\frac{\partial}{\partial t}|\Psi(t)\rangle = H|\Psi(t)\rangle, \tag{4.1}$$

and extracts the trivial time dependance leaving the time independent $|\psi\rangle$, such that

$$|\Psi(t)\rangle = e^{-\frac{i}{\hbar}Ht}|\psi\rangle. \tag{4.2}$$

A complication is that due to the laser field, $H(t) = H_e + H_0 + W(t)$ is a time dependent Hamiltonian. Here we have the electronic and nuclear kinetic energies, and interaction between the atoms and the electromagnetic field of the laser represented by H_e, H_0, and $W(t)$ respectively. In the Born-Oppenheimer approximation one considers the diatomic system with the internuclear separation R fixed. The total electronic Hamiltonian can be diagonalised defining the R dependent electronic states $|\alpha_i\rangle$ each satisfying

$$H_e|\alpha_i\rangle = V_i(R)|\alpha_i\rangle, \tag{4.3}$$

in which the operator H_0 is approximately diagonal. Here V_i denote the Born-Oppenheimer potentials. We must now incorporate the interaction with the laser field into this picture.

Using a classical field to represent the vector potential for a mono-chromatic plane wave with polarisation vector $\hat{\boldsymbol{\epsilon}}$ we have

$$\boldsymbol{\mathcal{A}} = \mathcal{A}\hat{\boldsymbol{\epsilon}}\left[e^{i(\boldsymbol{k}\cdot\boldsymbol{r}-\omega t)} + e^{-i(\boldsymbol{k}\cdot\boldsymbol{r}-\omega t)}\right]. \tag{4.4}$$

The Coulomb gauge condition gives the contribution to the Hamiltonian:

$$W = \frac{q^2\mathcal{A}^2}{2m_e} + \frac{i\hbar q}{m_e}\boldsymbol{\mathcal{A}}\cdot\nabla \approx \frac{i\hbar q}{m_e}\boldsymbol{\mathcal{A}}\cdot\nabla, \tag{4.5}$$

were have made the approximation that the field is weak enough to neglect second order terms. If we consider time averaging the couplings of $|\alpha_i\rangle$ induced by W we see

$$\begin{aligned}\langle W_{ij}\rangle_t &= \frac{1}{2\tau}\int_{t_0+\tau}^{t_0-\tau}\langle\alpha_i|W|\alpha_j\rangle \mathrm{d}t \\ &= \langle\alpha_i|\frac{1}{2\tau}\left(\int_{t_0-\tau}^{t_0+\tau} e^{\boldsymbol{k}\cdot\boldsymbol{r}}e^{\frac{it}{\hbar}\Delta_-} + e^{-\boldsymbol{k}\cdot\boldsymbol{r}}e^{\frac{it}{\hbar}\Delta_+}\,\mathrm{dt}\right)\frac{i\hbar q}{m}\mathcal{A}\hat{\boldsymbol{\epsilon}}\cdot\nabla|\alpha_j\rangle,\end{aligned} \tag{4.6}$$

with $\Delta_\pm = E_i(R) - E_j(R) \pm \hbar\omega$. Allowing τ to become large allows us to neglect the coupling unless Δ_+ or Δ_- is zero, corresponding to emission or absorption of a photon respectively. Motivated by this we can replace $W(t)$ with

$$\begin{aligned}\overline{W} &= \mathcal{A}\frac{i\hbar q}{m_e}\left(e^{i\boldsymbol{k}\cdot\boldsymbol{r}}\gamma_+ + e^{-i\boldsymbol{k}\cdot\boldsymbol{r}}\gamma_-\right)\hat{\boldsymbol{\epsilon}}\cdot\nabla \\ &\approx \mathcal{A}\frac{i\hbar q}{m_e}\left(\gamma_+ + \gamma_-\right)\hat{\boldsymbol{\epsilon}}\cdot\nabla, \end{aligned} \tag{4.7}$$

where $\gamma_\pm$ connects electronic states that differ in energy by an amount $\pm\hbar\omega$. In the final line the well-known dipole approximation [57] setting $\exp(\pm i\boldsymbol{k}\cdot\boldsymbol{r}) \approx 1$ has been used.

To arrive at our final form for the matrix elements of $\overline{W}$ we re-write the vector potential amplitude $\mathcal{A}$ in terms of the laser intensity I, and apply the Heisenberg equation of motion for a dynamical variable to the matrix elements of ∇, this yields

$$\langle\alpha_i|\overline{W}|\alpha_j\rangle \approx \sqrt{\frac{I}{2\epsilon_0 c}}\left(\gamma_+ + \gamma_-\right)\hat{\boldsymbol{\epsilon}}\cdot\boldsymbol{D}_{ij}. \tag{4.8}$$

Here $\boldsymbol{D}_{ij} = \langle\alpha_i|q\boldsymbol{r}|\alpha_j\rangle$ is the dipole matrix element. This form accounts for the time dependence of the electromagnetic field and also allows us to apply the tools of quantum mechanical scattering theory to the problem at hand.

4.3.3 Evolution of the diatomic wave function

Starting from eq. (4.1) with the Hamiltonian $H = H_0 + V + \overline{W}$ where the matrix elements of V include the Born-Oppenheimer potentials alluded to in eq. (4.3) as well as the Zeeman and hyperfine interactions $H_z(B)$, we can define a solution of the form in eq. (4.2). If we define the channel hamiltonians as

$$H_g = H_0 + V_g + H_{\mathrm{Z}}(B), \text{ and} \tag{4.9}$$

$$H_x = H_0 + V_x, \tag{4.10}$$

then, in the absence of the laser, the Feshbach molecular wave function satisfying the Schrödinger equation can be written as $|\phi(t)\rangle = \exp(-iH_g t/\hbar)|\phi\rangle$. By virtue of being the state from which the total wave function in the presence of the laser $|\Psi(t)\rangle = \exp(-iHt/\hbar)|\Psi\rangle$ originates, it defines the initial boundary condition for this problem.

By assuming that the laser pulse is long in comparison to the time over which the collision dynamics take place we can formulate the boundary condition as

$$\lim_{t\to-\infty}\left|\left|e^{-\frac{i}{\hbar}Ht}|\Psi\rangle - e^{-\frac{i}{\hbar}H_g t}|\phi\rangle\right|\right| = 0. \tag{4.11}$$

From this we may deduce that the $t = 0$ wave function is

$$|\Psi\rangle = \lim_{t\to-\infty} e^{\frac{i}{\hbar}Ht}e^{-\frac{i}{\hbar}H_g t}|\phi\rangle, \tag{4.12}$$

or equivalently [55],

$$|\Psi\rangle = \lim_{\epsilon\to0}\, i\epsilon\, G(E+i\epsilon)|\phi\rangle \tag{4.13}$$

$$= \lim_{\epsilon\to0}\, i\epsilon \begin{pmatrix} G_g & G_{gx} \\ G_{xg} & G_x \end{pmatrix}\begin{pmatrix} |\phi_b\rangle \\ 0 \end{pmatrix}, \tag{4.14}$$

where we have introduced the Green's operator $G(z) = (z - H)^{-1}$. For compactness of notation we leave the argument of the Green's operators implied. In this notation the Hamiltonian represented as:

$$H = \begin{pmatrix} H_g & \overline{W}_{gx} \\ \overline{W}_{xg} & H_x \end{pmatrix}, \tag{4.15}$$

clearly represents our system where an electronic ground state is coupled to an electronic excited state via the off diagonal elements of $\overline{W}$. The Lippmann-Schwinger equation [56] for the Green's function $G(z)$ allows us deduce that

$$G_g = \mathcal{G}_g + \mathcal{G}_g\overline{W}_{gx}\mathcal{G}_x\overline{W}_{xg}G_g \approx \mathcal{G}_g, \tag{4.16}$$

$$G_{xg} = \mathcal{G}_x\overline{W}_{xg}\left[\mathcal{G}_g + \mathcal{G}_g\overline{W}_{gx}G_{xg}\right] \approx \mathcal{G}_x\overline{W}_{x,g}\mathcal{G}_g, \tag{4.17}$$

and the channel Green's operators here are defined as $\mathcal{G}_{x(g)}(z) = (z - H_{x(g)})^{-1}$. The approximation made here is to neglect terms that are second order or higher in $\overline{W}$, this is distinct from the already neglected higher order terms in eq. (4.5) relating to the matter radiation coupling. Substituting eqs. (4.16) and (4.17) into (4.14) and applying the limit gives

$$|\Psi\rangle = \begin{pmatrix} |\phi_b\rangle \\ |\psi_x\rangle \end{pmatrix} = \begin{pmatrix} |\phi_b\rangle \\ \mathcal{G}_x(E+i0)\overline{W}_{xg}|\phi_b\rangle \end{pmatrix}. \tag{4.18}$$

4.3.4 Dissociation rate

The amplitude that the wave function evolves into a plane wave in the electronically excited state is obtained by applying $\langle\Phi| = (0, \langle\exp[-iE_{\phi_x}t/\hbar]\phi_x|)$ to the left of the full time dependent wave function giving

$$f(t) = \langle\Phi|e^{-\frac{i}{\hbar}Ht}|\Psi\rangle. \tag{4.19}$$

The probability of finding the system in the state $|\Phi_x\rangle$ is clearly $w(t) = |f(t)|^2$, so in order to obtain a rate we consider its partial derivative with respect to time

$$\dot{w}(t) = \dot{f}(t)f^*(t) + f(t)\dot{f}^*(t). \tag{4.20}$$

It can be shown [105] the $\dot{w}(0)$ is sufficient to define the transition rate here.

4.3.5 Connection with the Frank-Condon overlap integral

It is not yet clear how eqs. (4.18),(4.19) and (4.20) relate to the familiar Frank-Condon factor. By performing the matrix multiplications that are implied by eq. (4.19) one immediately obtains

$$f(0) = \langle\phi_x|\mathcal{G}_x(E+i0)\overline{W}_{xg}|\phi_b\rangle, \tag{4.21}$$

and the time derivative

$$\dot{f}(0) = -\frac{i}{\hbar}\Big[\langle\phi_x| + \langle\phi_x|V_x\mathcal{G}_x(E+i0)\Big]\overline{W}_{xg}|\phi_b\rangle. \tag{4.22}$$

We now introduce the electronically excited channel scattering states such that

$$|\phi_x^{\pm}\rangle = |\phi_x\rangle + \mathcal{G}_x(E \pm i0)V_x|\phi_x\rangle, \tag{4.23}$$

which in combination with eqs. (4.20) to (4.22) gives

$$\dot{w}(0) = \frac{2\pi}{\hbar}\left|\langle\phi_b|\overline{W}_{gx}|\phi_x^+\rangle\right|^2\delta(E - E_\phi). \tag{4.24}$$

This makes explicit how the Frank-Condon overlap factor, $\left|\langle\phi_b|\overline{W}_{gx}|\phi_x^+\rangle\right|^2$, follows logically from the full time dependent treatment of the problem, with the approximations that have been described earlier.

4.3.6 The classical Condon point and probing the system

In a simplified picture of photodissociation one would consider two atoms approaching one another, one atom may suddenly become electronically excited upon absorbing a photon. The point at which this would happen is referred to as the classical Condon point. Here the potential energy difference between the initial and final states is equal to the photon energy; the kinetic energy of the colliding pair is in that instant unchanged. Figure 4.3 illustrates such a transition, with the upper dashed line indicating the total energy after absorption of a photon.

In practice this picture remains useful in a quantum mechanical treatment, where the transition strength is estimated by the Franck-Condon integral. This is because the transition to the excited state is most strongly driven in the vicinity of the classical Condon point cf. sec. 4.3.5 and sec. 4.3.8. The local contribution to the Franck-Condon integral proportional to

$$I(E,r) = \left| \int_{r-a}^{r+a} \phi_b(r')\phi_x(E,r')\,\mathrm{d}r' \right|^2 \tag{4.25}$$

is presented in fig. 4.4. It is plotted for various scattering state energies E. In this illustrative calculation we have fixed a at 1 a_0, the singlet component of the Feshbach molecular wave function is $\phi_b(r)$, and the electronically excited scattering state with $\mathrm{B}^1\Pi_u$ symmetry into which it can be transferred is $\phi_x(E,r)$. The integral is seen to be strongly peaked around the classical Condon point.

4.3.7 Dipole allowed transitions

Here the absorption of a photon drives dipole allowed transitions from the $\mathrm{X}^1\Sigma_g^+$ (singlet) state into the $\mathrm{A}^1\Sigma_u^+$ and $\mathrm{B}^1\Pi_u$ states, and also from the $\mathrm{a}^3\Sigma_u^+$ (triplet) state into the $1^3\Sigma_g^+$ and $1^3\Pi_g$ states. Figure 4.1 shows the potential energy as a function of internuclear separation that these atom pairs would possess in each of these cases. However, the vast majority of the Feshbach molecule's probability density resides in the triplet component. This can be seen from the asymptotic behaviour of the Feshbach molecular wave function shown in fig. 4.3 (internuclear distance is represented on a logarithmically spaced axis). It is, though, concentrated in the halo region $r > 60$ a_0.

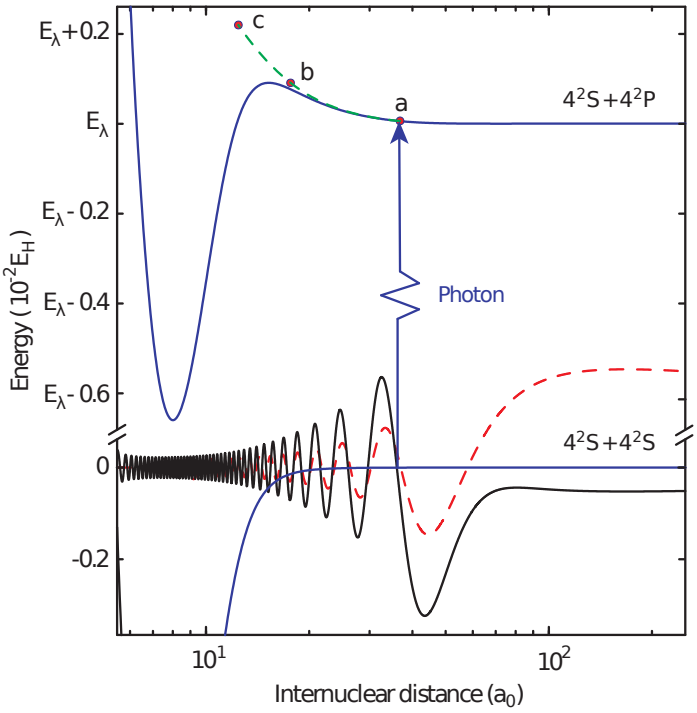

Figure 4.3: The singlet component (black solid) of the Feshbach molecular wave function is driven into an excited state with $B^1\Pi_u$ symmetry. The repulsive $B^1\Pi_u$ potential is shown as the upper solid blue line going to the $4^2S + 4^2P$ asymptote. The lower solid line going to the $4^2S + 4^2S$ asymptote is the $X^1\Sigma_g^+$ potential. Here E_λ is the energy of a photon driving the atomic D_2 transition. The red dashed line is the triplet component of the Feshbach molecular wave function. The upper green dashed line shows the energy of the atoms after the absorption of the photon, i.e., the kinetic energy is the difference between this and the $B^1\Pi_u$ potential curve. This kinetic energy increases as the Condon point moves to smaller radii. The green curve also indicates that the measurements probe the barrier region between c and a. When the Condon point is at a the photo-dissociation is suppressed due to the corresponding node in the large r part of the Feshbach molecular wave function [106]. If excited to point b the atoms are energetically over the top of the barrier.

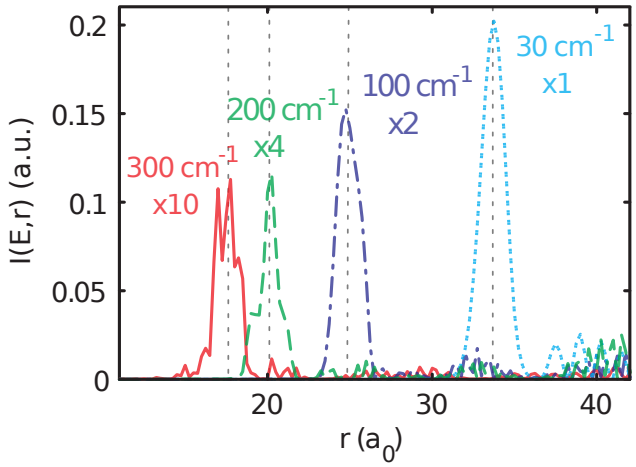

Figure 4.4: The local contribution to the Franck-Condon overlap integrals, within a bin of width 2 a_0 centred at r. As the detuning is increased from 30 cm^{-1} to 300 cm^{-1} the main contributing section moves inwards tracking the classical Condon point (marked by vertical dotted grey lines). For ease of comparison each line has been rescaled individually with $\times 10$ indicating it has been magnified by a factor of 10.

The Condon points that we are probing are at a shorter range than this, where the singlet component is dominant. Consequently transitions from the triplet component are neglected. Furthermore we need only consider transitions to the $B^1\Pi_u$ state, neglecting the $A^1\Sigma_u^+$. This is due to the different nature of their respective potential curves. The $B^1\Pi_u$ has a repulsive long range form that goes proportional to r^{-3}, connecting to an inner well. In the intermediate region joining these two is the barrier. On the other hand the $A^1\Sigma_u^+$ has a deeper inner well, and is attractive at long range, with no barrier. The result is that the associated Condon point is at a smaller internuclear separation where the singlet component of the molecular wave function is comparatively weak.

4.3.8 Photodissociation near potential maxima

We now go on to use the Franck-Condon integral (see eq. (4.24)) as the starting point for a qualitative investigation into how rapidly photodissociation varies with changes in the laser detuning. Especially the case when the kinetic energy in the excited state is close in magnitude to the maximum height of the potential barrier. To do this we replace the bound and scattering state wave functions with their WKB approximate forms, as have

been used previously in the context of laser assisted resonant collisions [80, 107]. Since we are only interested in peak spacings we neglect normalisation factors and say that the functional form of the photodissociation rate will be approximately proportional to the square of the following integral

$$I = \left| \int_{R_c-\Delta}^{R_c+\Delta} \sin[\zeta_x(r)] \sin[\zeta_g(r)] \, \mathrm{d}r \right|^2 , \tag{4.26}$$

where Δ extends the integral sufficiently far around the Condon point R_c. The WKB phase is accumulated between the inner turning point R_t and the point r, and is given by

$$\zeta_{x(g)}(r) = \frac{\pi}{4} + \int_{R_t}^{r} \sqrt{\frac{2\mu}{\hbar} T_n(r')} \, \mathrm{d}r'. \tag{4.27}$$

We further simplify by neglecting faster oscillating contributions to I, leaving

$$I \approx \left| \frac{1}{2} \int_{R_c-\Delta}^{R_c+\Delta} \cos[\zeta_x(r) - \zeta_g(r)] \, \mathrm{d}r \right|^2 , \tag{4.28}$$

and make a power series approximation to the argument about the Condon point R_c

$$\zeta_x(r) - \zeta_g(r) \approx b_0 + \frac{b_2}{2}(R - R_c)^2. \tag{4.29}$$

Extending the range of integration from 0 to ∞ we can then approximate the integral as

$$I \approx \left| \sqrt{\frac{\pi}{2b_2}} \cos\left(b_0 - \frac{\pi}{4}\right) \right|^2 . \tag{4.30}$$

Since we are interested in general statements about the spacing of photodissociation maxima or minima we consider the periodicity of I as the laser detuning E_ω is varied. We define the π-periodicity $P_\pi(E_\omega)$ as being equal to the energy, E'_ω, such that $E'_\omega < E_\omega$ and that the value of b_0 changes by π as the detuning goes from E'_ω to E_ω. For any particular fixed E_ω, b_0 is given by

$$b_0 = \zeta_x(R_c) - \zeta_g(R_c). \tag{4.31}$$

In fig. 4.5 we show the behaviour of $P_\pi(E_\omega)$ in the vicinity of a potential maximum $V_B = V_x(R_B)$. By this we mean that the kinetic energy of atoms in the electronically excited state is near the threshold for passing over the repulsive barrier in V_x (see point b in fig. 4.3). As E_ω approaches V_B the inner turning point decreases continuously towards R_B. When E_ω crosses this threshold R_t jumps suddenly to a point on the

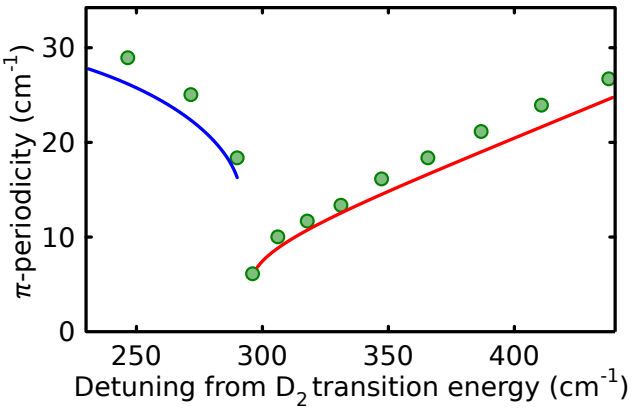

Figure 4.5: The periodicity of the photodissociation trace as the laser detuning is changed. The solid lines represent what is expected from the simplified WKB considerations outlined in the text. A break in the line and abrupt change in the trend is visible at a detuning equivalent to the height of the barrier in the excited state potential. The points are discreet samples of this periodicity, obtained by rigorous calculation of the photodissociation trace, and extraction of the minima spacings, cf. fig. 4.7.

inner repulsive wall of the potential. The potential contributions to the integral in eq. (4.27) are, then, very different on either side of the threshold. The result being that the trend of $P_\pi(E_\omega)$ changes abruptly at this point. We later use this as a method for determining the height of the potential barrier.

4.3.9 Detailed numerical calculations

In order to determine the initial ground state molecular wave function $|\phi_b\rangle$ we perform a coupled-channels calculation. This approach has been discussed in previously in chapter 3. Again here we use the Manolopoulos log-derivative propagation technique [77] to integrate the multichannel time independent Schrödinger equation numerically. The ground state Hamiltonian consists of the interatomic interaction in the Born-Oppenheimer approximation, the interaction of the valence electrons and atomic nuclei with the magnetic field, the hyperfine interaction, and the usual kinetic energy term relating to the relative nuclear motion. We solve for the Feshbach molecular binding energy and wave function. This wave function is then used to define the initial state from which Franck-Condon excitation creates an outgoing flux in the excited state.

Equation (4.18) gives

$$|\psi_x\rangle = \mathcal{G}_x(E + i0)\overline{W}_{xg}|\phi_b\rangle, \tag{4.32}$$

which represents the process described above. This equation can be rendered in to the form of a second order driven differential equation [108] for $|\psi_x\rangle$ with the driving term being the Feshbach molecular wave function multiplied by the dipole matrix element. Due to the combination of the long range nature of the Feshbach molecule and the rapid oscillations of the excited state wave function it is necessary to use numerical methods specifically designed for this problem. We numerically solve this equation in the close coupling approximation [55] using the linear piecewise reference potential method of Alexander [109]. The amplitude and thus photo-dissociation cross section can be extracted from the large internuclear separation $r \to \infty$, limit of $\psi_x(R)$, see also ref. [110].

4.4 Results and discussion

We now discuss the dependence of the photodissociation rate on the magnetic field strength and laser detuning. The inset to fig. 4.6 implies that the positions of atom number peaks do not strongly depend on the magnetic field strength at which the system is held between magnetic field sweeps. The main figure shows the rate for five separate magnetic field strengths.

The variation in rate is explained by the radial probability density amplitude in the region near to the classical Condon point. Here a higher magnetic field value gives a more weakly bound Feshbach molecule. As the more weakly bound state is more halo like, the bulk of the wave function sits at large internuclear separations leaving the inner region depleted. This suppresses the photodissociation rate for wavelengths of laser light that give Condon points in this inner region. Here the probability density is extracted from the singlet component of the Feshbach molecular wave function derived from numerical coupled-channels calculations. This observation supports the Frank-Condon model discussed above, and also serves as a direct measurement of the amplitude of the singlet component of the Feshbach molecular wave function.

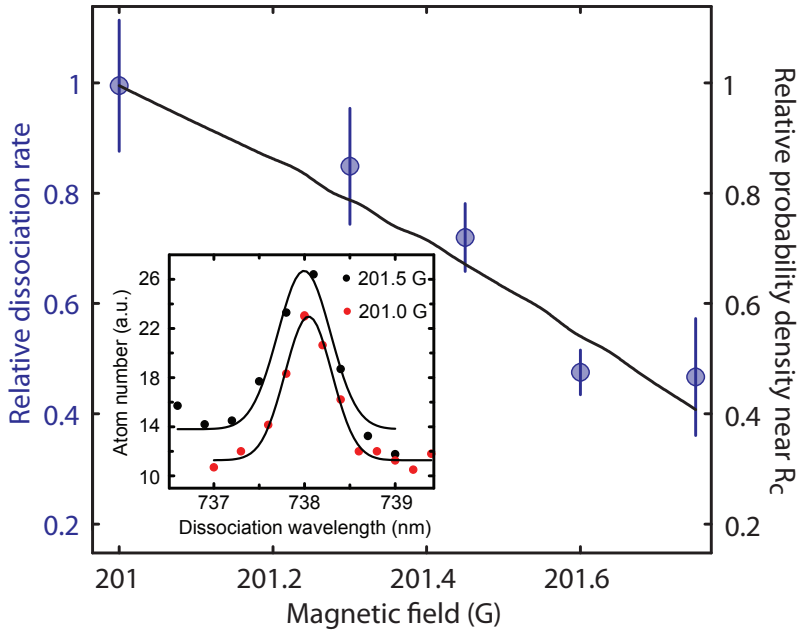

Figure 4.6: Photo-dissociation rate for different magnetic field strengths with all other parameters being identical. The rate is shown relative to the rate at $B = 201$ G. The solid line is the probability density at the Condon point of the singlet component of the molecular state relative to its value at $B = 201$ G. The variation of the rate with the magnetic field is explained by the probability of finding the atoms within the non-halo region where the classical Condon point is. The inset shows the remaining atom number for a range of dissociation wavelengths, and for two different magnetic field strengths. The figure shows that although moving closer to the Feshbach resonance decreases the atom loss rate during the pulse, it does not alter the shape of the feature, i.e., the two peaks coincide.

Since the detuning determines the internuclear separation at which a molecule to free atoms transition is most strongly driven, each measurement probes a different region of the $B^1\Pi_u$ potential. Starting with large separation, then through to the barrier, and then on to the region well characterised by conventional molecular spectroscopy. Figure 4.3 illustrates these points by showing the relevant transition from the molecular wave function, and the kinetic energy that the atom pair has after absorbing a photon.

If we neglect collisions between atoms and molecules, the surviving molecule number after the photodissociation pulse if given by $N(t) = N_0 \exp(-\sigma I t)$, where σ is proportional to the photodissociation cross section while t and I denote duration and intensity of the light pulse. This exponential behaviour was verified experimentally for several detunings (not shown). In order to systematically measure the dependence of atom loss on detuning, we recorded a series of scans in laser frequency, each individual scan with a fixed intensity and pulse duration. The results of these scans are shown in fig. 4.7, in rescaled atom numbers $\widetilde{N} = (N/N_0)^n$, where N_0 denotes the maximum atom number in that data set and $n \propto 1/It$. This is equivalent to extrapolating the measurement to an arbitrary laser duration and intensity and additionally compensates for different mean atom numbers. The resulting roughly continuous plot can be compared to the results of our theoretical calculations. While the above rescaling precludes a quantitative point-wise comparison between the experimental and theoretical atom loss data, fig. 4.7, however, shows an excellent qualitative agreement on the shape of the spectrum. In order to extract quantitative information we extract the positions of atom number peaks, which remain unaffected by the above rescaling. Figure 4.7 (b) shows the spacing of these peaks versus the peak position. The plot shows where one expects the photodissociation cross section to be minimal, but also represents samples of the π-periodicity as discussed in sec. 4.3.8. Also shown are the expected peak spacings arising from our rigorous numerical model. We find good agreement between the experimental data and the calculated values using the newly constructed potential (see below) alongside our coupled-channels calculation for the Feshbach molecular state. Furthermore the figure shows more structure than is immediately apparent from the raw trace. The measured spectrum can be split into roughly three regions.

In the first section the photo-dissociation minima are entirely determined by the nodes of the long range Feshbach molecular wave function: The lowest detuning atom number peak in fig. 4.7 (b) corresponds to the process indicated by point a in fig. 4.3. At

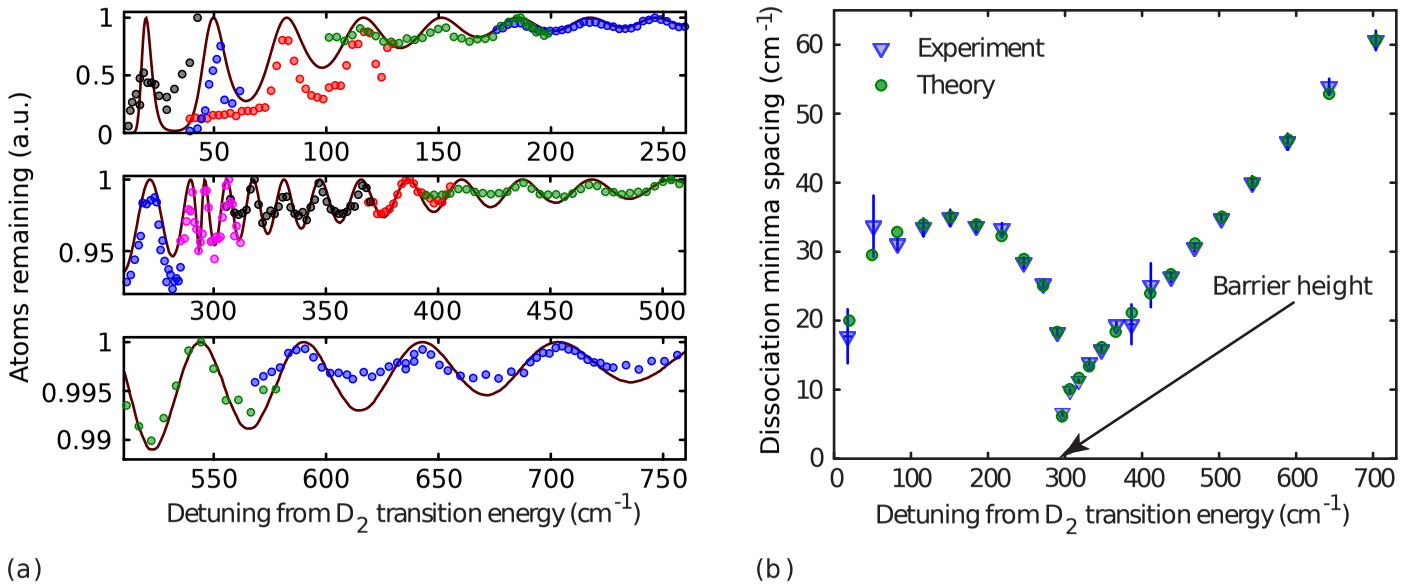

Figure 4.7: (a): The extrapolated number of atoms remaining after the dissociation laser has been applied $\widetilde{N}$, where coloured circles represent different data sets. Each one has been processed separately, as described in the text. The solid line represents the theoretical prediction calculated for a fixed pulse time and intensity.
(b): The energy spacing of the peaks in atom numbers versus the position of those peaks. The experimental data is represented by the blue triangles. The green circles are the predicted spacings based on the theoretical calculation. The point at which there is a stark change in trend is marked by the arrow. This coincides with the detuning required to give enough kinetic energy to pass over the top of the barrier in the $B^1\Pi_u$ potential. At this energy the classical Condon point is at b in fig. 4.3.

this point, the photo-dissociation rate is suppressed by the presence of a pre-asymptotic nodal point in the singlet component of the molecular wave function [106]. Here the overall shape of the excited state wave function plays no part other than locally determining the position of the Condon point. This further verifies the accuracy of our coupled channels model for the Feshbach molecular wave function.

In the second region the atoms are excited to a position on the repulsive part of the potential, approaching the barrier. This corresponds to the region between points b and c in fig. 4.3.

Third is the region (between b and c) where the kinetic energy of the atoms is such that they can pass over the top of the potential barrier. The second and third region are split by the point were the photon is absorbed around a Condon point to the right of the barrier, see point b in fig. 4.3. At this point the kinetic energy is great enough for the atoms to just pass over the top of the barrier. Here a structure is observed that is consistent with that arising from our simplified WKB analysis displayed in fig. 4.5. With this in mind, the sharp downwards kink visible in the peak position spacing is indicative of the height of the local maximum of the $B^1\Pi_u$ potential. This is a direct measurement of the potential barrier height which does not rely on comparison with a model potential. This value is confirmed by comparison with the height of the barrier extracted from our constructed potential indicated by the arrow in fig. 4.7 (b).

To arrive at satisfactory agreement between experiment and theory we had to construct a $B^1\Pi_u$ potential by combining data from several sources [76, 92, 93, 96, 111, 112] in addition to our photodissociation data. In adjusting the parameters determining the shape of the potential we found that there was an initial mismatch between the long and short range parts of the potential due to the value for the ground state dissociation energy used in refs. [92, 93]. This showed up as a noticeable disagreement between the observed and calculated peak positions and spacings, albeit with the trends being generally similar. The problem was remedied by using the improved value from ref. [76]. This shift also directly improved low detuning behaviour of the peak spacing due to the improved quality of the potential in the intermediate barrier region. The other parameters determining the shape of the barrier could then be fine tuned affecting mainly the three points lying immediately to the low detuning side of the sharp downwards kink in fig. 4.7 (b). The detailed construction of the $B^1\Pi_u$ (leading to the 1_u) potential is

further elucidated in appendix B.1. Tables B.1 and B.2 give the parameters and spline nodes needed to fully recreate the potential energy curve that we constructed.

In order to arrive at a global best fit for the form of the potential, a procedure would have to be adopted where all the conventional spectroscopic data, the photodissociation data, and the long range measurements, were combined. However, due to the potential barrier, it is justified to treat the deep inner part of the potential separately from the barrier and long range regions. Our measurement then provides an elegant way to confirm that the two have been accurately connected. A further point here is that we have performed a measurement capable of directly probing just one of the excited state potentials using a single photon absorption process. This simplifies the analysis greatly when compared to multi-photon processes or measurements with more than one possible final state. In principle the technique and simplifications exploited here could also be used to study the $B^1\Pi_u$ Born-Oppenheimer potential for other alkali metal atoms.

Because of the similarity of the short range wave function of a Feshbach molecule and an on-site pair of atoms in an optical lattice, our results can be used to predict the most suitable wavelengths for blue-detuned optical lattices. This minimises losses due to the singlet component of the on site diatomic wave function and thereby minimises heating. In order to have full predictive power at more extreme blue detunings, reliable 4^2S+4^2P potentials of triplet character are required. In addition to this, as the Condon point moves further inwards, and the kinetic energy of the final state increases, the core interaction may become important.

We have gained a good understanding of the processes involved in the photodissociation of Feshbach molecules. By systematically investigating the dependance of this process on the magnetic field strength and dissociating laser detuning we have gained insight into qualities of the Feshbach molecular state, and the excited state interactions. This was done while describing a convenient procedure for contributing to the construction of $B^1\Pi_u$ Born-Oppenheimer potentials for alkali metal atoms.

5

Helium-4 trimers, a toy model

5.1 Introduction

The scattering processes in ultra-cold gases consisting of alkali metal atoms are influenced by those bound states that are near to the threshold for dissociation into free particles. The highest excited diatomic bound state wave function has the general form of: an inner part that probes the properties of the potential well, and an exponentially decaying part that is sensitive to the $-C_6/r^6$ tail of the potential. The exponential tail contains a large proportion of the total probability distribution and becomes more dominant as the molecular binding energy moves towards the threshold. A system sharing these features is that of ^{4}He, which we study in this chapter. The ^{4}He potential is of interest in this context as it only supports one bound state. This makes it simpler to handle than the alkali metal atomic interactions. In addition, the only bound state of $^4He_2$ is close to threshold, giving it similar properties to that of a weakly bound alkali metal dimer, i.e. its wave function consists mainly of the exponentially decaying section probing the long range $-C_6/r^6$ tail. For this reason it is often referred to as a halo molecule, being very different to what one would usually consider as being a molecule. The ^{4}He potential also supports a weakly bound three body ground state, and is expected to support an excited three body state. Both the ^{4}He dimer and trimer states have been studied experimentally [41], and theoretically [113, 114]; making this a convenient system to test our proposed methods, before applying them to the alkali metal atomic interactions where an *ab initio* treatment would be considerably more difficult.

Given that these systems have the properties discussed above it would seem possible to model them approximately, so long as the approximations recreate near threshold properties. To this end we employ pseudo-potential methods [115] to model the three body Hamiltonian, with the pseudo-potential set up to mimic the low energy two body bound state and scattering properties. We work throughout with the approximation that all but s-wave states are excluded.

We begin in section 5.2 by illustrating two methods to solve the two body problem for realistic ^{4}He potentials. First by efficiently allocating mesh points depending on the depth of the potential well at each point of a spatial grid [116]. Second we employ a technique that exploits the fall off in the strength of the potential using Green's function techniques for a dimer system. This approach is similar to the one that will be used in the later pseudo-potential model for the dimer. In section 5.3 we introduce the use of pseudo-potentials [115] by applying them to the helium dimer. We solve the Schödinger equation, using a Green's function technique, for the ^{4}He pseudo-potential that we parameterise by comparison with the more detailed models. We then go on, in section 5.4, to use Faddeev techniques [117] with the pseudo-potential from the previous section to study the ^{4}He trimer. We calculate the binding energies, wave functions, and radial probability densities of the trimer states and compare them to those calculated using realistic potentials [114].

5.2 The two body system with realistic potentials

5.2.1 The C_6 optimisation of the grid

In this section we employ the method outlined in ref. [116]. The s-wave radial Schrödinger equation for two atoms interacting through a potential $V(r)$ at inter-atomic separation r is

$$\left[-\frac{\hbar^2}{mr}\frac{d^2}{dr^2}r + V(r)\right]\psi(r) = E_{2\mathrm{b}}\psi(r). \tag{5.1}$$

Here m is the atomic mass, ψ is the bound state wave function, and $E_{2\mathrm{b}}$ is the two body bound state energy. A method is required to allow both the inner well, and the outer $-C_6/r^6$ part of the potential, to be adequately resolved on the same spatial grid. In order to achieve this we use a non-homogeneously spaced grid in the discrete variable representation of the Hamiltonian. This grid can be generated via a coordinate

transformation $y = u(r)$ where $u(r)$ is a function that is strictly monotonic, i.e. it has an inverse $U(y)$. In this context it is convenient to consider a function that preserves the norm under the transformation u, it can be seen that $\phi(y) = \sqrt{U'(y)}\, r\psi(r)$ satisfies this requirement. This results in the kinetic energy operator becoming

$$T = -\frac{\hbar^2}{m}\left[p(y)\frac{d^2}{dy^2} + q(y)\frac{d}{dy}\right]. \tag{5.2}$$

Here $p(y) = [U'(y)]^{-2}$ and $q(y) = -U''(y)[U'(y)]^{-3}$.

A suitable transformation can be motivated by considering the period of wave function oscillations estimated using the WKB method. The resulting coordinate transformation equation is

$$u(r) = -\frac{1}{2}\left(\frac{R_0}{r + R_s}\right)^2. \tag{5.3}$$

The free parameters R_0 and R_s can be adjusted to give an optimal fit for the problem at hand. The Hamiltonian of this system is set up in the transformed coordinates, and is analysed in terms of a basis set expansion, where the basis states are box states in the coordinate y. The problem is then solved through taking the eigenvalues, to give the bound state energy of the dimer, and the corresponding eigenvector to give the wave function. This is then transformed back into the r coordinate. The dashed curve in fig. 5.1 shows the result of this method implemented for the ^{4}He dimer system, using the TTY [113] potential shown by the solid line. This potential has an analytic form derived from perturbation theory, and compares well to semi-empirical potentials [118] and *ab initio* calculations [119]. The plot shows how a significant proportion of the wave function probes the outer part of the potential.

5.2.2 Solving the bound state equation using Green's function techniques

An alternative way to solve the Schrödinger equation is by using Green's function techniques [56]. This method is similar to the one we will later go on to use in the case of the three-body problem. The free particle Green's function is defined as [56]

$$G_0(z) = (z - H_0)^{-1}, \tag{5.4}$$

with H_0 being the free particle Hamiltonian, and where z is a generally complex number with the dimensions of energy. The stationary Schrödinger equation,

$$(E_{2\mathrm{b}} - H_0)|\psi\rangle = V|\psi\rangle, \tag{5.5}$$

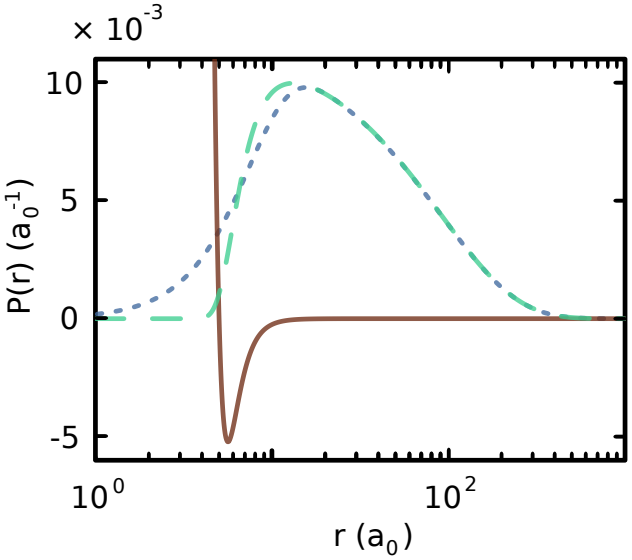

Figure 5.1: The radial probability densities for the helium dimer calculated using the transformed grid method (green dashed) and using the pseudo-potential method (blue dotted). The shape of the TTY [113] potential (brown) is also shown in comparison to the large spatial extent of the dimer.

can be re-written in integral equation form by multiplying eq. (5.5) from the left by the free particle Green's operator $G_0(z)$, evaluated at $z = E_{2b}$. This gives

$$|\psi\rangle = G_0(E_{2b})V|\psi\rangle. \tag{5.6}$$

Using the wave function [56]

$$\phi(r) = \sqrt{|V(r)|}\psi(r), \tag{5.7}$$

in the position representation, results in the following equation:

$$\int \mathrm{d}^3r'\, v(r)\langle \boldsymbol{r}|G_0(E_{2b})|\boldsymbol{r}'\rangle w(r')\,\phi(r') = \phi(r). \tag{5.8}$$

Here $w(r') = \sqrt{|V(r')|}\mathrm{Sign}(V(r'))$, and $v(r) = \sqrt{|V(r)|}$. The integral over the solid angle projects out the s-wave symmetry. The kernel of the integral is evaluated on a grid, and its eigenvalues are determined while E_{2b} is varied parametrically. Once a unit eigenvalue has been found the parameter E_{2b} recovers a physical bound state energy, and the associated eigenvector corresponds to the function of eq. (5.7). Given

the numerical function $\phi(r)$ the bound state wave function can be determined through eq. (5.6).

The significance of using $\phi(r)$ as defined in eq. (5.7) is that as the potential decays relatively quickly, the grid size needed to calculate the product of $\psi(r)$ with $\sqrt{|V(r)|}$ is smaller than that required to calculate $\psi(r)$ directly. This method is a textbook technique when calculating scattering states [56], and, due to the large extent of the wave function in the systems that we consider, it is useful here. The result of this calculation matches the dashed curve in fig. 5.1.

5.3 The two body system with a pseudo-potential

We now apply the Green's function method for the Schrödinger equation to a separable pseudo-potential.

5.3.1 The separable pseudo-potential

The ^{4}He system that we are currently considering has a single s-wave two-body bound state. Accordingly, we replace the realistic potential by a single separable term [115]

$$V = |\chi\rangle A \langle\chi|. \tag{5.9}$$

Here V takes on the form of a projection operator, meaning that there can be at most one bound state [120]. In the following we treat the functional form of the form factor χ as arbitrary, so long as the associated Schrödinger equation has similar long range behaviour to that of the exact bound state wave function, in so far as it is determined by correctly recovering the s-wave scattering length. Due to its convenience in analytical calculations, we choose a Gaussian form factor which is given in the momentum space representation by [121]

$$\langle \boldsymbol{p}|\chi\rangle = \left(\frac{\sigma^2}{\pi\hbar^2}\right)^{3/4} e^{\frac{-p^2\sigma^2}{2\hbar^2}}. \tag{5.10}$$

Here $\boldsymbol{p}$ is the relative momentum of the two atoms with

$$\langle \boldsymbol{r}|\boldsymbol{p}\rangle = \frac{e^{i\boldsymbol{p}\cdot\boldsymbol{r}/\hbar}}{(2\pi\hbar)^{3/2}}. \tag{5.11}$$

In order to set the parameters A and σ we first need equations relating them to a, the s-wave scattering length, and $E_{2\mathrm{b}}$, the ^{4}He dimer bound state energy.

5.3.2 Scattering properties

The zero momentum limit of the T-matrix determines the s-wave scattering length [55] through the following general relation:

$$\langle \boldsymbol{p}' = 0|T(0)|\boldsymbol{p} = 0\rangle = \frac{a}{2\pi^2\hbar m}. \tag{5.12}$$

The T-matrix can be calculated using the Lippmann Schwinger equation [56]

$$T(z) = V + VG_0(z)T(z)\ . \tag{5.13}$$

For the separable potential this can be written out as an infinite geometric series. Using eq. (5.9), this gives

$$T(z) = |\chi\rangle A\langle\chi| + |\chi\rangle A\langle\chi|G_0(z)|\chi\rangle A\langle\chi| + \dots\ , \tag{5.14}$$

which can be summed to produce

$$T(z) = |\chi\rangle\tau(z)\langle\chi|, \tag{5.15}$$

where

$$\tau(z) = \frac{A}{1 - A\langle\chi|G_0(z)|\chi\rangle}. \tag{5.16}$$

The matrix element in the denominator, $\langle\chi|G_0(z)|\chi\rangle$, can be calculated using eq. (5.10) and the following representation of the free particle Green's function

$$G_0(E_{2\mathrm{b}}) = \int \frac{|\boldsymbol{p}\rangle\langle\boldsymbol{p}|}{E_{2\mathrm{b}} - p^2/m}\,\mathrm{d}^3p. \tag{5.17}$$

Given the form factor of eq. (5.10), one finds

$$\langle\chi|G_0(z)|\chi\rangle = \left(\frac{\sigma^2}{\pi\hbar^2}\right)^{3/2} 4\pi \int_0^\infty \frac{e^{-p^2\sigma^2/\hbar^2}}{z - p^2/m}\,p^2\,\mathrm{d}p. \tag{5.18}$$

This taken with eqs. (5.12) and (5.15) in the limit $z \to 0$ gives the desired relation

$$A = \frac{\hbar^2}{2\sigma^2 m}\left(\frac{\sigma\pi^{1/2}}{a} - 1\right)^{-1}, \tag{5.19}$$

which allows us to eliminate A in favour of a and σ.

5.3.3 Bound state spectrum

In order to eliminate the remaining model parameter σ we begin by inserting eq. (5.9) into eq. (5.6) and multiplying by $\langle\chi|$ from the left. This leads to a transcendental equation for $E_{2\mathrm{b}}$,

$$[1 - A\langle\chi|G_0(E_{2\mathrm{b}})\ |\chi\rangle]\,\langle\chi|\psi\rangle = 0. \tag{5.20}$$

Carrying out the integral of eq. (5.18) we arrive at the following equation for the bound state energy:

$$\frac{2A\sigma^2 m}{\hbar^2}\left[xe^{x^2}\mathrm{erfc}(x) - 1\right] = 1, \tag{5.21}$$

where $x = \sqrt{m\sigma^2\pi|E_{2\mathrm{b}}|}/\hbar$ and $\mathrm{erfc}(x) = \frac{2}{\sqrt{\pi}}\int_x^\infty \exp(-u^2)\,\mathrm{d}u$ is the complementary error function. This equation is solved numerically to determine σ, and so all the model parameters are eliminated in favour of physical quantities.

5.3.4 The dimer wave function

Given the bound state energy, the dimer wave function associated with the separable potential can be obtained through eq. (5.6). In order to convert $\langle\boldsymbol{p}|\psi\rangle$ into the spatial wave function we perform a three dimensional Fourier transform. Integrating the solid angle part of the Fourier integral we get

$$\psi(r) = \sqrt{\frac{2}{\pi\hbar^3}}\int_0^\infty j_0\left(pr/\hbar\right)\psi(p)\,p^2\,\mathrm{d}p, \tag{5.22}$$

where j_0 is the spherical Bessel function of zeroth order. In order to more accurately treat the oscillating factors, we perform partial integration giving

$$\begin{aligned}\psi(r) =& \sqrt{\frac{2}{\pi\hbar^3}}\left[-\frac{\hbar^2 p}{r^2}\cos(pr/\hbar)\psi(p)\right]_{p=0}^{p=\infty} \\ &+ \sqrt{\frac{2}{\pi\hbar^3}}\frac{\hbar^2}{r^2}\int_0^\infty \cos\left(pr/\hbar\right)\frac{\mathrm{d}}{\mathrm{d}p}\left[p\psi(p)\right]\,\mathrm{d}p.\end{aligned} \tag{5.23}$$

The remnant integral is split as a sum and the cosine integrated exactly between mesh points, i.e. the $\frac{\mathrm{d}}{\mathrm{d}p}\big(p\psi(p)\big)$ is approximated by a difference across each interval.

5.3.5 Comparison of pseudo-potential with realistic potentials

The wave functions calculated using the different methods are displayed in fig. 5.1. The two exact treatments produce the same result and so only the transformed grid wave

Method	$\lvert E_{2b}\rvert$	$\langle r\rangle$	σ	a
Green's function	1.321	97.7	–	188.2
Transformed grid	1.321	97.7	–	–
Pseudo-potential	1.321	97.6	6.3	188.2

Table 5.1: Binding energies (mK) and bond lengths (a_0) for the three models. Also shown are the parameters used to set up the pseudo-potential, σ and a (a_0).

function is plotted. The pseudo potential is expected to reproduce the long distance behaviour of the wave function, by virtue of being set up to reproduce the binding energy of the dimer. This is visible as the pseudo-potential wave function is seen to converge with those of the realistic treatments at a radius of approximately $15\,a_0$ (a_0 being the Bohr radius). Note that this is a logarithmic plot, and that the wave functions actually coincide for the majority of inter-atomic separations shown here. The bound state energies and bond lengths calculated for the exact treatments show good agreement with those calculated for the same potential in refs. [114], and [113]. These values are displayed in table 5.1. The bound state energies and scattering lengths from the exact treatments are used to set up the pseudo-potential approach, and so it is not surprising that these are in agreement, however alongside the good agreement of the radial probability densities the bond lengths also match well. The value of σ that is used to produce these results is $6.3\,a_0$.

5.4 The three-body system

The three particle problem is considerably more challenging than the two particle problem. An obvious indicator of this is given by considering the extra degrees of freedom. Also, unlike in the two particle case, the problem can no longer be reduced to that of a single particle experiencing some potential. As a result the boundary condition of the problem is less clearly defined. In the two particle case taking the interparticle separation towards infinity in some sense weakens the interaction strength, and eventually leads to two free particles, where the wave function is entirely determined by the free propagator. In the three particle case there is no simple analogy. Removing one particle to infinity does not leave a non-interacting system, and the wave function is

not determined by a free propagator alone. A method for summing over the possible interactions is required. This is provided by the Faddeev approach which we follow here. For a full description of the mathematical difficulties arising in the quantum mechanical three body problem see the [53, 120] and references therein.

Given that the properties of the helium dimer are well reproduced by the separable potential we will attempt to use pairwise pseudo-interactions to model the three body state. The general momentum space Faddeev treatment for the separable potential is explained in ref. [122].

5.4.1 Faddeev approach for three particles

In general, the three-body Hamiltonian with pairwise interactions in Jacobi coordinates is given by [56]:

$$H = -\frac{\hbar^2}{6m}\nabla^2_{\mathbf{R}} - \frac{3\hbar^2}{4m}\nabla^2_{\boldsymbol{\rho}} - \frac{\hbar^2}{m}\nabla^2_{\mathbf{r}} + V(\boldsymbol{r}) + V(\boldsymbol{\rho}+\boldsymbol{r}/2) + V(\boldsymbol{\rho}-\boldsymbol{r}/2). \tag{5.24}$$

Here V is the two body potential used earlier, and the Jacobi coordinates are explained in fig. 5.2. Potentials that depend on the coordinates of all three particles simultaneously are neglected throughout this work. This type of interaction is short range in the sense that it vanishes when one particle is taken far away from the other two. As a result it does not contribute to the normal mathematical difficulties usually associated with the quantum mechanical three body problem. That is not to say that it will not at some level have an effect, rather that due to its short range nature it is reasonable to neglect it in a first approximation.

Working in the centre of mass frame and introducing the notation $V_i = V(\boldsymbol{r}_{jk})$ [where (i,j,k) is any permutation of the numbers $1,2,3$ and $\boldsymbol{r}_{jk}$ is the coordinate vector between particles j and k] the three-body equivalent of eq. (5.6) becomes

$$G_0(E_{3\mathrm{b}})(V_1+V_2+V_3)|\psi\rangle = |\psi\rangle. \tag{5.25}$$

Here $E_{3\mathrm{b}}$ is the total energy of the three atom system. Following the Faddeev method [117], eq. (5.25) can be written as the sum of three Faddeev components:

$$|\psi\rangle = |\psi_1\rangle + |\psi_2\rangle + |\psi_3\rangle. \tag{5.26}$$

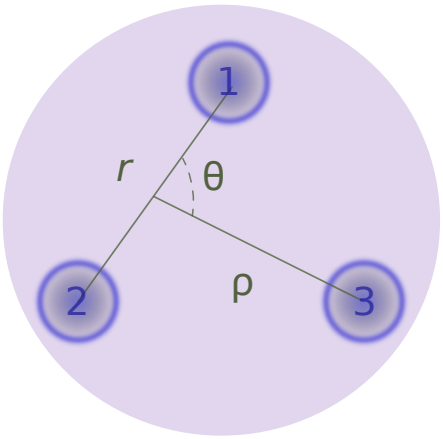

Figure 5.2: An illustration of the Jacobi coordinate system for three particles. Here $\mathbf{r}$ is the vector from particle 2 to particle 1, $\boldsymbol{\rho}$ is the vector from the centre of mass of the two particle sub-system to the third particle, and $\mathbf{R}$ (not shown) is the centre of mass coordinate. The conjugate variables to $\mathbf{r}$ and $\boldsymbol{\rho}$, are $\boldsymbol{p}$ and $\boldsymbol{q}$ respectively.

Here

$$|\psi_1\rangle = G_0(E_{3b})V_1|\psi\rangle, \tag{5.27}$$

and the other components with indices 2 and 3 are defined similarly. These equations can be combined to give

$$|\psi_1\rangle = [1 - G_0(E_{3b})V_1]^{-1}\,(|\psi_2\rangle + |\psi_3\rangle), \tag{5.28}$$

where the $[1 - G_0(E_{3b})V_1]^{-1}$ term can be seen in terms of eq. (5.14) to result in

$$|\psi_1\rangle = G_0(E_{3b})T_1(E_{3b})(|\psi_2\rangle + |\psi_3\rangle). \tag{5.29}$$

Here $T_1(E_{3b})$ is the T-matrix that describes the scattering of the particle 2-3 subsystem, with particle 1 as a spectator.

5.4.2 Three identical bosons

As the system we consider is one of three identical Bose atoms, the Faddeev equations can be transformed into one another through cyclic permutation of the atomic indices. This action is represented by a unitary operator $\mathcal{U}$ such that $\mathcal{U}\psi(\mathbf{R}, \boldsymbol{\rho}, \mathbf{r})$ gives

$\psi(\mathbf{R}, \boldsymbol{\rho}', \mathbf{r}')$ where

$$\begin{aligned} \boldsymbol{\rho}' &= -\frac{1}{2}\boldsymbol{\rho} + \frac{3}{4}\boldsymbol{r}, \\ \boldsymbol{r}' &= -\boldsymbol{\rho} - \frac{1}{2}\boldsymbol{r}. \end{aligned} \tag{5.30}$$

This means that eq. (5.29) can be expressed as

$$|\psi_1\rangle = G_0(E_{3\mathrm{b}})T_1(E_{3\mathrm{b}})(\mathcal{U}|\psi_1\rangle + \mathcal{U}^2|\psi_1\rangle), \tag{5.31}$$

and that eq. (5.26) becomes

$$|\psi\rangle = |\psi_1\rangle + \mathcal{U}|\psi_1\rangle + \mathcal{U}^2|\psi_1\rangle. \tag{5.32}$$

5.4.3 Faddeev approach with a separable potential

In the separable potential approximation the T-matrix, $T_1(E_{3\mathrm{b}})$, is represented in terms of the two body T-matrix for scattering between atoms 2 and 3 via the interaction V_1 [115],

$$T_1(E_{3\mathrm{b}}) = \int |\boldsymbol{q}, \chi\rangle \tau \left(E_{3\mathrm{b}} - \frac{3}{4m}q^2 \right) \langle \boldsymbol{q}, \chi| \, \mathrm{d}^3 q. \tag{5.33}$$

Here the possible momenta, $\boldsymbol{q}$, of the third spectator particle is integrated over all possible values, the argument of the two body T-matrix τ is the energy of the interacting atoms i.e. the total energy with the kinetic energy of the spectator subtracted. This expression allows us to separate out the $\boldsymbol{\rho}$ and $\boldsymbol{r}$ parts of the wave function by substituting eq. (5.33) into eq. (5.31), which gives the Faddeev component as:

$$|\psi_1\rangle = G_0(E_{3\mathrm{b}})|f, \chi\rangle. \tag{5.34}$$

The amplitude $f(\boldsymbol{q})$ is determined by the equation,

$$f(\boldsymbol{q}) = \tau(\tilde{E}_{3\mathrm{b}})\langle \boldsymbol{q}, \chi|(\mathcal{U} + \mathcal{U}^2)G_0(E_{3\mathrm{b}})|f, \chi\rangle, \tag{5.35}$$

where

$$\tilde{E}_{3\mathrm{b}} = E_{3\mathrm{b}} - \frac{3}{4m}q^2. \tag{5.36}$$

Writing the right hand side of Eq. (5.35) in the momentum representation, the amplitude $f(\boldsymbol{q})$ is determined by the integral equation,

$$f(\boldsymbol{q}) = \tau(\tilde{E}_{3\mathrm{b}}) \int \mathcal{K}(\boldsymbol{q}, \boldsymbol{q}'; E_{3\mathrm{b}}) f(\boldsymbol{q}') \, \mathrm{d}^3 q', \tag{5.37}$$

where the kernel is given by

$$\mathcal{K}(\boldsymbol{q},\boldsymbol{q}';E_{3\mathrm{b}}) = \langle \boldsymbol{q},\chi|(\mathcal{U}+\mathcal{U}^2)G_0(E_{3\mathrm{b}})|\boldsymbol{q}',\chi\rangle. \tag{5.38}$$

The kernel $\mathcal{K}$ can be calculated by combining eqs. (5.10), (5.38), and the following representation of $G_0(E_{3\mathrm{b}})$:

$$G_0(E_{3\mathrm{b}}) = \int \frac{|\boldsymbol{q},\boldsymbol{p}\rangle\langle\boldsymbol{q},\boldsymbol{p}|}{E_{3\mathrm{b}} - \frac{3}{4m}q^2 - \frac{1}{m}p^2}\,\mathrm{d}^3p\,\mathrm{d}^3q. \tag{5.39}$$

As we are considering s-wave states, $f(\mathbf{q}')$ has rotational symmetry, and so the solid angle in eq. (5.38) can be integrated over. Replacing $\mathcal{K}(\boldsymbol{q},\boldsymbol{q}';E_{3\mathrm{b}})$ with $\mathcal{K}(q,q';E_{3\mathrm{b}})$ we have

$$f(q) = \tau(\tilde{E}_{3\mathrm{b}})\int_0^\infty \mathcal{K}(q,q';E_{3\mathrm{b}})f(q')\,q'^2\,\mathrm{d}q', \tag{5.40}$$

and for $\mathcal{K}(q,q';E)$,

$$\begin{aligned}\mathcal{K}(q,q';E_{3\mathrm{b}}) =& \frac{4\sigma^3}{\sqrt{\pi}\hbar^3}\frac{1}{qq'}e^{\frac{\sigma^2}{\hbar^2}\left[-mE_{3\mathrm{b}}+\frac{3}{8}(q'^2+q^2)\right]}\\ &\times\left[\mathrm{Ei}\left(\frac{\sigma^2}{\hbar^2}(mE_{3\mathrm{b}}-q'^2-q^2+qq')\right)\right.\\ &\left.-\mathrm{Ei}\left(\frac{\sigma^2}{\hbar^2}(mE_{3\mathrm{b}}-q'^2-q^2-qq')\right)\right],\end{aligned} \tag{5.41}$$

where the principal value integral $\mathrm{Ei}(x) = \int_{-\infty}^{x}\frac{e^u}{u}\,\mathrm{d}u$ is known as the exponential integral function.

5.4.4 Trimer binding energies

The binding energies are calculated here by discretising the integral in eq. (5.40) and evaluating the integral's kernel on a quadratic mesh in q and q'. This is then equivalent to a matrix equation of the form $\underline{F} = \underline{\underline{K}}(E_{3\mathrm{b}})\ \underline{F}$. The correct energy is found by calculating the trace of $[\underline{\underline{K}}(E_{3\mathrm{b}}) - \underline{\underline{I}}]^{-1}$, where $\underline{\underline{I}}$ is the identity matrix, while $E_{3\mathrm{b}}$ is varied parametrically. When $\underline{\underline{K}}(E_{3\mathrm{b}})$ has a unit eigenvalue, the trace becomes infinite. This calculation is made for a range of parameters $E_{3\mathrm{b}}$, and any energy that causes the trace to become singular is a value of $E_{3\mathrm{b}}$ that satisfies eq. (5.40).

The three-body bound state energies calculated for the case of pairwise TTY potentials in ref. [114], can be reproduced, to an excellent degree of accuracy, with an

σ	E_{g}	$\langle r_i \rangle$	$\langle r_{ij} \rangle$	$\sqrt{\langle r_{ij}^2 \rangle}$	E_{e}	$\langle r_i \rangle$	$\langle r_{ij} \rangle$	$\sqrt{\langle r_{ij}^2 \rangle}$
6.30	143.1	9.99	16.93	19.50	2.359	95.58	155.76	187.0
8.02	96.95	12.44	21.09	24.22	2.089	109.6	178.2	221.6
6.79	126.4	10.71	18.14	20.87	2.264	99.04	161.3	200.4
Ref. [114]	126.4	10.49	18.16	20.71	2.277	93.67	150.7	183.7

Table 5.2: The binding energies of the helium trimer states (mK), ground (E_{g}) and excited (E_{e}), for different values of the range parameter σ: $6.30\,a_0$ recreates the two body bound state energy and scattering length calculated in section 5.2, the value $8.02\,a_0$ is consistent with the same diatomic helium properties quoted in ref. [114], while $6.79\,a_0$ recreates the three body ground state energy from ref. [114]. Here $\langle r_{ij} \rangle$ is the average atom-atom distance, and $\langle r_i \rangle$ is the average distance of a helium atom from the centre of mass, both quoted in units of a_0, while $\sqrt{\langle r_{ij}^2 \rangle}$ is the root mean square of the atom-atom distance in units of a_0.

adjustment of the σ parameter away from that which optimises the two body interaction, i.e. to $\sigma = 6.79\,a_0$, see table 5.1. The energies calculated are -126.4 mk, and -2.26 mk for the ground and excited states respectively. The ground state value is chosen to be the same as that calculated in ref [114], and the excited state energy agrees to within around 0.5 %.

5.4.5 The momentum space Faddeev component

Once the trimer binding energies are found, the factor $|f\rangle$ can be calculated in order to obtain the first Faddeev component $|\psi_1\rangle$, and hence $|\psi\rangle$. To this end, the eigenvector corresponding to the unit eigenvalue, at each binding energy, is determined using matrix diagonalisation. That eigenvector is the amplitude $|f\rangle$ in the momentum representation. This allows the first Faddeev component $\psi_1(\boldsymbol{q}, \boldsymbol{p})$ to be calculated through eq. (5.34).

5.4.6 Faddeev component in coordinate space

Starting from eq. (5.34) and using eq. (5.39), the first non-normalised Faddeev component can be Fourier transformed in six dimensions leading to

$$\psi_1(\rho, r) \propto \int e^{i\boldsymbol{q}\cdot\boldsymbol{\rho}/\hbar} e^{i\boldsymbol{p}\cdot\boldsymbol{r}/\hbar} \frac{f(q)g(p)}{E_{3\mathrm{B}} - \frac{3}{4m}q^2 - \frac{1}{m}p^2}\, \mathrm{d}^3q\, \mathrm{d}^3p. \tag{5.42}$$

Integrating over the two sets of azimuthal angles, the problem is now one of calculating a two dimensional sine transform

$$\psi_1(\rho, r) \propto \int_0^\infty \int_0^\infty pq \, \sin(q\rho/\hbar) \sin(pr/\hbar) \times \frac{f(q)g(p)}{E_{3\mathrm{B}} - \frac{3}{4m}q^2 - \frac{1}{m}p^2} \, \mathrm{d}p \, \mathrm{d}q. \tag{5.43}$$

This is integrated numerically.

The three Faddeev components can now be combined to give the entire wave function depending on the two Jacobi lengths ρ and r and also the angle between the $\boldsymbol{\rho}$ and $\mathbf{r}$ vectors. This is done by two dimensionally interpolating the first Faddeev component. Using eq. (5.30) with the expression of the full wave function of eq. (5.32), this gives

$$\psi(\boldsymbol{\rho}, \mathbf{r}) = \psi_1(\boldsymbol{\rho}, \mathbf{r}) + \mathcal{U}\psi_1(\boldsymbol{\rho}, \mathbf{r}) + \mathcal{U}^2\psi_1(\boldsymbol{\rho}, \mathbf{r}). \tag{5.44}$$

For this system the six dimensional Jacobi coordinates (excluding centre of mass) can be transformed to the six dimensional analogue of spherical coordinates, i.e. five hyper-angles and one hyper-radius [123]. Due to rotational symmetry this can be reduced to the following set of two hyper-angles and one hyper-radius:

$$\begin{aligned} R &= \sqrt{\frac{1}{2}r^2 + \frac{2}{3}\rho^2}, \\ \theta &= \frac{\mathbf{r} \cdot \boldsymbol{\rho}}{r\rho}, \\ \phi &= \arctan\left(\frac{2\rho}{\sqrt{3}r}\right). \end{aligned} \tag{5.45}$$

The wave function is often represented in terms of the hyper-radial probability density $P(R)$ where two angular variables are averaged out. To calculate $P(R)$, the quantity $R^5|\psi(R, \theta, \phi)|^2$ is multiplied by what remains of the six dimensional solid angle element, which is proportional to

$$\mathrm{d}\Omega = \sin^2\phi \cos^2\phi \, \mathrm{d}(\cos\theta) \, \mathrm{d}\phi, \tag{5.46}$$

and is then integrated over the hyper-angles. The result of this calculation is presented in fig. 5.3. Even the helium trimer ground state is seen to have a large spatial extent. This wave function is dwarfed however by that of the excited state which can be seen to extend to considerably larger hyper-radii. These trimers can then be considered

the three atom version of the halo molecules discussed earlier. This large extent also justifies our exclusion of three atom potential terms in the Hamiltonian, since there is very little probability density in the region where these interactions would be large.

For the purpose of comparison the quantities calculated in table 5.2 are shown with the corresponding values taken from ref. [114]. The numbers show that the properties of the trimer ground state are recreated to within about 1 %, and those of the excited state to within about 7 %, when the pseudo-potential is set up to recreate the ground state binding energy and diatomic scattering length exactly. The difference between the values increases when the only information used to set up the pseudo-potential is the scattering length and dimer binding energy. Then the error is around 20 %.

5.5 Outlook

We have shown that, due to the long range nature of the dimer wave function, the ^{4}He trimer can be reasonably modelled using pseudo-potentials that mimic the low energy scattering and bound state properties. In light of these results we intend to use pseudo potentials in the description of three-body collisions in ultracold gases of alkali metal atoms in the vicinity of a Feshbach resonance. This control over the atom-atom interactions allows studies of near threshold three-body quantum physics, such as three-body recombination into arbitrarily weakly bound dimer states.

The pseudo-potentials will again be set up in terms of diatomic properties. To this end we intend to include several bound states of the exact two-body potential in a separable potential model [56]. We shall see that pseudo-potential models used in the description of three atom collisions in ultracold gases can be applied using methods [124] similar to the Faddeev technique for bound states used in this chapter.

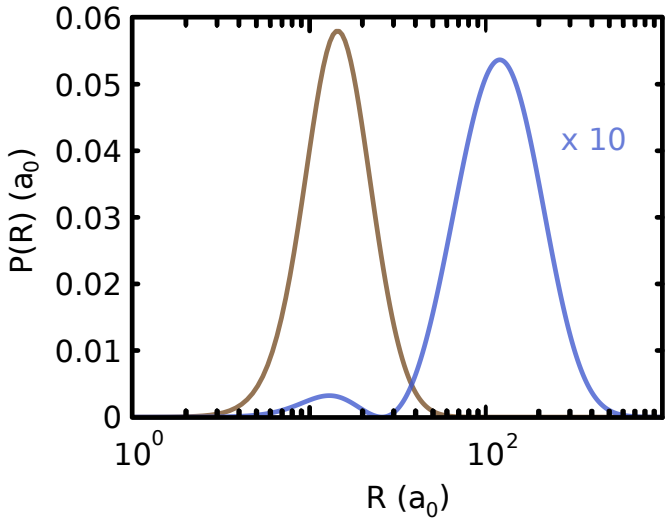

Figure 5.3: Plot of the hyper-radial probability densities for the ground (brown) and first excited (blue) states of the helium trimer. The excited state wave function has been magnified by a factor of ten. The plot shows the large spatial extents of both states.

6

Three-body scattering and Efimov's effect in Potassium-39

6.1 Introduction

Three body scattering has an important role to play in many trapped ultracold gas experiments. Three body recombination is a process where three atoms collide, two of which then form a molecule, the third atom and the molecule then recede from one another. The binding energy of the molecule is transferred into kinetic energy of the final state. If the energy released is sufficiently large, then the atom and molecule are lost from the trap. This process is then a possible loss and heating mechanism. For processes such as evaporative cooling, a large scattering length is desirable as it facilitates thermalisation within the sample. One may choose to use a Feshbach resonance to tune the scattering length to some conveniently large value. However, the three body recombination rate has a non-trivial dependence on the scattering length. If an unfortunate choice of scattering length is made then there may be an anomalously large three body recombination rate – heating and atom loss may hinder evaporative cooling. On a historical note, the attempts to achieve Bose-Einstein condensation of Caesium [125] were blighted by this very problem.

The study of Efimov's effect [39] in alkali metal atoms [13, 42, 43, 44, 45, 46, 47, 48, 49, 50, 51, 52] is one example where three body recombination is not seen as an obstacle. In fact, we shall see that the three body recombination rate can be analysed, giving up information regarding the spectrum of trimer states. Given our previous discussion of

two particle scattering it should not be surprising that the existence of weakly bound trimer states has a strong effect on the near threshold three body scattering properties.

In this chapter we use the coupled channels model, that we developed and tested rigorously in chapters 3 and 4, to investigate in detail the near 400 G *aa* channel *s*-wave Feshbach resonance in ^{39}K [126]. Chapters 3 and 4 were concerned with ^{40}K, but since we are working within the Born-Oppenheimer approximation it is a trivial matter to adapt our calculation so that it is valid for ^{39}K. Motivated by the usual treatment of Feshbach resonant scattering (see chapter 2), we then proceed by setting up a simplified two channel model that recreates the essential near threshold properties of the two atom system. Extending the ideas laid out in chapter 5 and ref. [127], we then use this as the starting point for a three-body recombination calculation for comparison with the experimental observations of ref. [13].

6.2 Feshbach resonance in the diatomic system

In this section we give a detailed characterisation of the Feshbach resonance that we are concerned with. We look at the near threshold molecular physics and scattering. The standard parameterisation of the Feshbach resonance is used; revealing that this resonance is especially broad and has a negative background scattering length.

6.2.1 Single atom eigenstates

The hyperfine and Zeeman states are shown in fig. 6.1. A notable difference here when compared to the single atom spectrum of ^{40}K shown in fig. 3.1, is the conventional nature of hyperfine splitting; the $f = 2$ state is above the $f = 1$ state. The eigenstates are now labelled from a to h in order of increasing energy. It is immediately obvious when comparing figs. 3.1 and 6.1 that the latter represents a simpler system. By this it is meant that there are fewer possible spin states available, because of ^{39}K having a smaller nuclear spin quantum number.

6.2.2 Diatomic scattering channels

It is instructive to see what are the relevant diatomic spin combinations. Since we are considering a gas of ultracold atoms prepared in the $|\{f = 1, m_f = 1\}\rangle$ state, rotational symmetry of the Hamiltonian about $\boldsymbol{B}$ suggests that we need only consider spin states

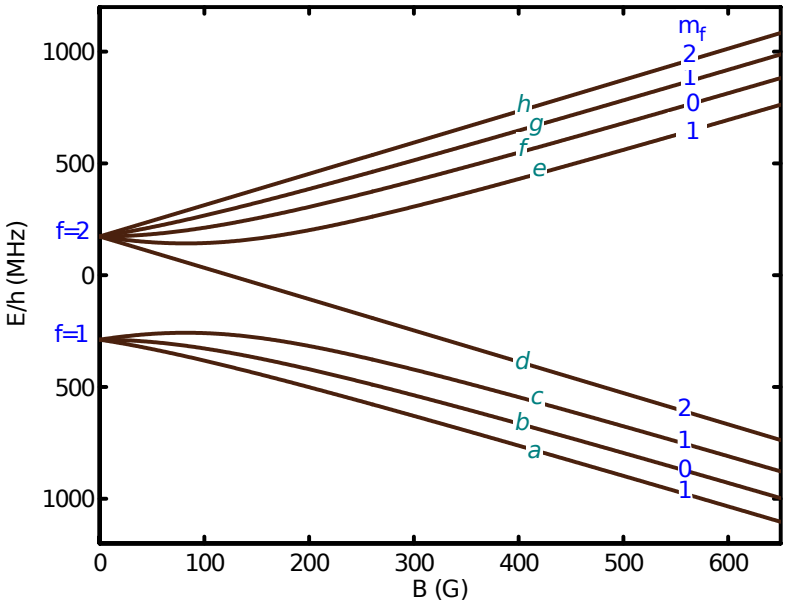

Figure 6.1: The energy eigenvalues of the single ^{39}K atomic Zeeman and hyperfine Hamiltonian as a function of applied magnetic field. We label the states from a to r in order of increasing energy. Also shown are the m_f quantum numbers, and the $B = 0$ states, f, with which they correspond.

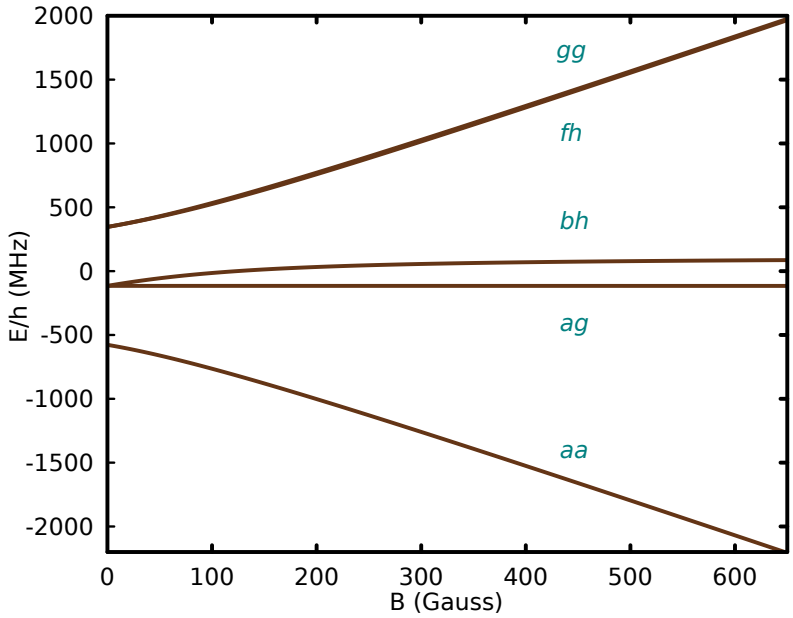

Figure 6.2: Energies of the diatomic scattering thresholds that have the same $M_F = m_{f1} + m_{f2}$ as the aa threshold. These spin combinations are coupled together during a collision.

with $M_f = m_{f1} + m_{f2} = 2$. Also, because the atoms are bosons, we need only consider combinations that give a symmetric spin wave function. The diatomic spin states that are coupled to the aa state are the ag, bh, fh, and gg states. The energies of their corresponding scattering thresholds are shown in fig. 6.2. We are assuming here that only s-wave collisions need be taken into account. In fact this was verified by performing coupled channels calculations that included higher partial waves. We found no significant difference when compared to the s-wave only results discussed here.

6.2.3 Near threshold molecular physics

We can now examine the near threshold molecular bound states. It is well known [55, 56] that such states have a strong influence over the diatomic scattering properties. It is also the case that they form an important part of the final target state in the three body recombination process which we will go on to model. With this in mind we suppose that the more closely any approximate model can reproduce binding properties the better that model is. Unlike with our previous example of ^{4}He, ^{39}K supports many s-wave

molecular bound states. We concentrate on just a few of them which are energetically close to the threshold.

First and foremost fig. 6.3 shows that the bound state responsible for the 400 G. Feshbach resonance starts out at $B = 0$ at a depth of around $E/h = -400$ MHz. The energy of this bound state remains approximately constant as the magnetic field moves up to around 100 G. By examining the molecular wave function, calculated using our rigorous coupled channels model, we see that this is explained by identifying the dominant spin component. The likelihood of finding the molecule in a particular combination of states is shown in fig. 6.4. The majority of the wave function exists, at small $|\boldsymbol{B}|$, in the aa spin state combination giving it the same magnetic moment as the aa continuum states. The trajectory of the molecular binding energy then goes through an avoided crossing as the magnetic field strength is increased. This avoided crossing is responsible for the bound state then being forced towards the scattering threshold. This gives rise to the Feshbach resonance where the bound state eventually becomes degenerate with the threshold. The trajectory is explained by again considering the spin properties of the molecule. As the avoided crossing is traversed the dominant spin component becomes that which we identify with the $\{ag, bh\}$ label. This means that the spin wave function is a symmetric mixture of the ag and bh diatomic states.

The bound state immediately below this one is also interesting as it shares the avoided crossing with the Feshbach molecular state. Beginning at around $E/h = -1000$ MHz it progresses roughly linearly towards the avoided crossing where it then decreases in magnetic moment and becomes approximately constant in energy as the magnetic field strength is increased further. Again examining the molecular wave function projected onto the separated atoms spin eigenstates explains these features fully. The molecular wave function is dominated by its $\{ag, bh\}$ component in the linearly increasing region, and its aa component in the constant energy region. It smoothly moves between the two through the avoided crossing.

When the molecular state gets very close to threshold the energy can be seen to bend away, as the component in the aa channel becomes once again dominant. This can be seen more clearly in the inset of fig. 6.5. At the point of the Feshbach resonance, where the molecular state is fully degenerate with the threshold, the aa component can be seen to make up 100% of the molecule. Figure 6.4 shows that spin states other than

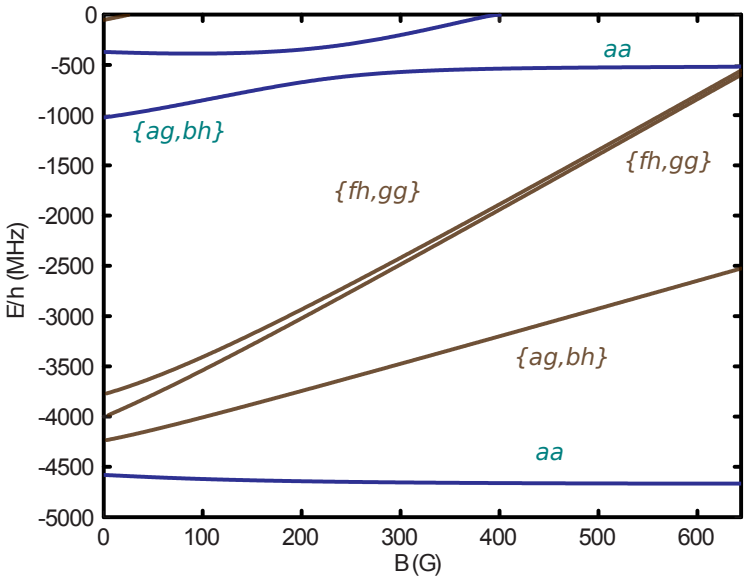

Figure 6.3: Near aa threshold vibrational s-wave bound states. The nature of the spin wave functions are indicated. Blue lines indicate levels that are included in the two-channel Feshbach model. All energies are relative to the aa scattering threshold.

the two combinations that we have identified play a very small part in the constitution of the Feshbach molecule.

Given the above observations, we say that the Feshbach molecule can be modelled by a bound state with $\{ag, bh\}$ spin characteristic coupled to both a bound state that belongs to the aa channel, and the aa scattering continuum. We thus identify the $\{ag, bh\}$ bound state as being the bare resonance state [27]. The energy of the bare resonance state $E_{\mathrm{res}}(B)$ is indicated in fig. 6.5. It can be seen to cross the aa entrance channel threshold at B_{res}, close to the actual resonance position B_0 which is shifted away from B_0 due to coupling between the bare resonance state and the aa scattering continuum.

6.2.4 Background channel scattering

The non-resonant contribution towards the scattering amplitude is determined here by the entrance channel interaction in the absence of coupling. Since our entrance channel is characterised by the maximally stretched aa state, which is an $S = 1$ triplet state, we may say that the background is determined by the triplet Born-Oppenheimer potential.

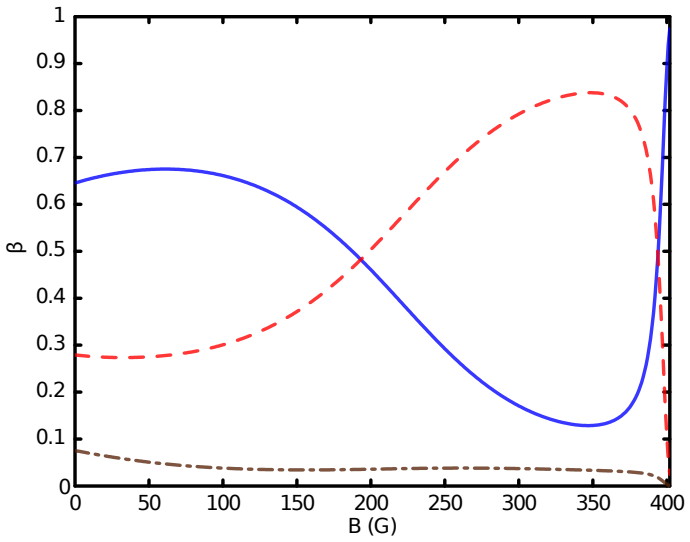

Figure 6.4: Make up of the bound state wave function responsible for the resonance. The solid line shows the proportion in the entrance channel component, the dashed line shows the closed channel, and the dash-dot line represents the proportion in the spin states that are neglected from the two channel.

We calculate that the two highest vibrational states supported by the triplet potential are at E/h =-514 MHz and E/h =-4701 MHz. These can be seen to approximately agree with the two states in fig. 6.3 that are labelled as aa. Similarly the triplet scattering length is $-33.41a_0$, this is seen to be very similar to the value of $a_{\rm bg} = -29.51a_0$ extracted by fitting the resonance formula (2.30) to coupled channels data.

6.2.5 Scattering near the aa threshold

A useful quantity that can be derived from the S-matrix is the scattering phase shift $\delta(E, B)$. Here it is defined as $S = \exp[2i\delta(E, B)]$, where S is the well known scattering matrix element for elastic scattering [55]. The S-matrix is subject to the constraint $|S| = 1$ and so $\delta(E, B)$ is a real number. In fig. 6.5 we display molecular binding energies below the threshold, and above threshold we represent continuum states by plotting $\sin^2[\delta(E, B)]$. The closed channel bare resonance state is indicated, above the threshold it is associated with a rapid change in the phase shift. The inset shows an expanded plot of the region immediately around the Feshbach resonance. As mentioned the molecular

state bends away from the threshold, above zero energy the trend is reversed, with the trajectory converging with that of the bare resonance state.

6.3 Approximate model

We wish to produce an approximate two channel model which reproduces the main features of the coupled-channels results. The two channels represent the background channel and the "closed" channel. The Hamiltonian contains terms that couple these two channels together, causing the avoided crossing seen in fig. 6.3.

6.4 Two-Channel Model Hamiltonian

In order to set up a model system that contains the crucial information given in the previous section we begin by defining the two channel Hamiltonian

$$H = \begin{pmatrix} H_{\mathrm{bg}} & W|\phi_{\mathrm{res}}\rangle\langle\phi_{\mathrm{res}}| \\ |\phi_{\mathrm{res}}\rangle\langle\phi_{\mathrm{res}}|W & |\phi_{\mathrm{res}}\rangle\langle\phi_{\mathrm{res}}| \end{pmatrix}. \tag{6.1}$$

This is consistent with the usual two channel model of a Feshbach resonance within the single resonance approximation [27]. It is sometimes convenient to replace the coupling term by making use of

$$W|\phi_{\mathrm{res}}\rangle = \xi_0|\chi_0\rangle. \tag{6.2}$$

Here $|\phi_{\mathrm{res}}\rangle$ is the bare resonance state and ξ_i is a strength parameter for the form factor $|\chi_i\rangle$ ($i \in \{0, 1, \ldots, n\}$) where the $i = 0$ element parameterises inter-channel coupling. The $i > 0$ elements are used in the construction of a separable potential for the background channel Hamiltonian

$$H_{\mathrm{bg}} = H_0 + V_{\mathrm{bg}} \approx H_0 + \sum_{i=1}^{n} |\chi_i\rangle\xi_i\langle\chi_i|, \tag{6.3}$$

where $H_0 = -\frac{\hbar^2}{2\mu}\nabla^2$ is the kinetic energy operator. As used in our ^{4}He example we use Gaussian form factors,

$$\langle \boldsymbol{p}|\chi_i\rangle = \frac{e^{-p^2\sigma_i^2/2\hbar^2}}{(2\pi\hbar)^{3/2}}, \tag{6.4}$$

where the width parameters σ_i are chosen along with ξ_i to reproduce the correct two body scattering behaviour and bound state spectrum.

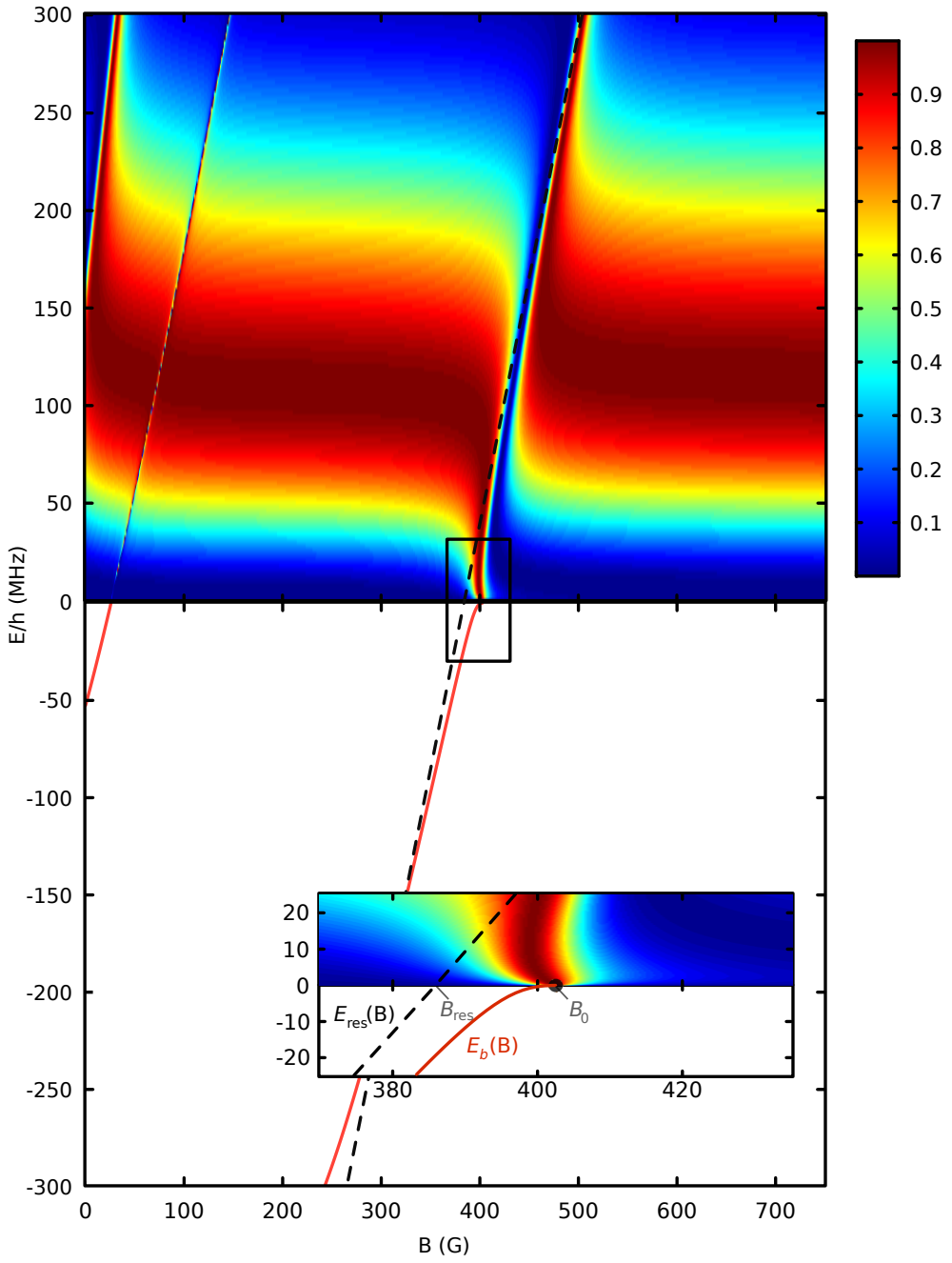

Figure 6.5: The correspondence between the bound state spectrum and the scattering phase shift $\delta(E, B)$. Red lines are molecular bound state energies relative to the aa threshold, black dashed lines are the closed channel bound state energies. The boxed area is shown in an expanded form in the inset. The colour bar indicates the value of $\sin^2[\delta(E, B)]$. The shift in resonance position from the closed channel threshold crossing $B_{\rm res}$ to the resonance position B_0 due to interaction with the entrance channel continuum is indicated.

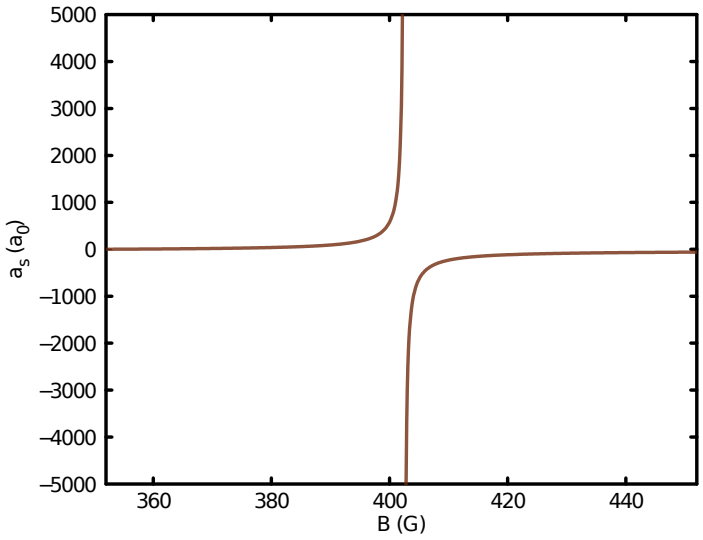

Figure 6.6: The variation of the s-wave scattering length with applied magnetic field for the ^{39}K 402 G aa resonance.

The greater the value of n, the number of terms in the representation of the background scattering channel potential, the greater the maximum number of molecular bound states that the model system can support. Also, more form factors afford us more free parameters when fitting to the scattering phase shift and resonance parameters.

6.4.1 Parameterising the model interaction

In order that our model of the diatomic system recreates as close as possible the results of coupled channels calculations in Sec. 6.2 we adjust the set of parameters that determine the inter-channel coupling and the separable expansion of the background potential. It is possible to reduce the dimensionality of the fitting problem by first deriving analytical constraints by the insistence that the scattering length recovers the form of eq. (2.30). Beyond this we perform a numerical least squares fit to both the molecular bound state spectrum, and scattering phase shift.

6.5 Three-body scattering

We now reintroduce the three body problem with the intention of using the diatomic model of the previous section to model the pairwise interactions. Other studies, see for example [128, 129], have looked into various aspects of the three body problem in the context of alkali metal atoms. Unlike here, though, they do not attempt to account for the intrinsic two-channel nature of magnetically tuneable Feshbach resonances. Also other approaches work in the limit of infinite scattering length, which is not the case here.

6.5.1 Three body arrangement-channel operators

We now define the arrangement-channel Hamiltonians h_α ($\alpha = 1, 2$ or 3) in such a way that each one represents three atoms, two of which interact via V_α, and the third is a spectator,

$$h_\alpha = h_0 + V_\alpha. \tag{6.5}$$

Here the kinetic energy term, h_0, is represented by

$$|\mathrm{bg}\rangle \left[-\frac{\hbar^2}{\frac{4}{3}m}\nabla_\rho^2 - \frac{\hbar^2}{m}\nabla_r^2 \right] \langle \mathrm{bg}|. \tag{6.6}$$

The projector on to the three atom entrance channel spin state, $|\mathrm{bg}\rangle$, has been introduced here. It corresponds to having all three atoms in the internal state that we have labelled as a. We also define the channel Green's operators as

$$g_\alpha(z) = (z - h_0 - V_\alpha)^{-1}, \tag{6.7}$$

and the full three-body Green's operator as

$$G(z) = (z - H)^{-1} = \left(z - h_0 - \sum_{\alpha=1}^{\alpha=3} V_\alpha \right)^{-1}. \tag{6.8}$$

The interaction operator represents two particle interactions embedded in the space of three particles. In the context of the two channel model, eq. (6.1),

$$\begin{aligned} V_\alpha =& |\mathrm{bg}\rangle V_\alpha^{\mathrm{bg}} \langle \mathrm{bg}| + |\phi_{\mathrm{res}}, \mathrm{cl}\rangle_\alpha E_{\mathrm{res}}(B)\, {}_\alpha\langle \phi_{\mathrm{res}}, \mathrm{cl}| + \ldots \\ & W_\alpha |\phi_{\mathrm{res}}, \mathrm{cl}\rangle_\alpha\, {}_\alpha\langle \phi_{\mathrm{res}}, \mathrm{cl}| + |\phi_{\mathrm{res}}, \mathrm{cl}\rangle_\alpha\, {}_\alpha\langle \phi_{\mathrm{res}}, \mathrm{cl}| W_\alpha. \end{aligned} \tag{6.9}$$

The ket representing two atoms having the spin and spacial characteristic of the bare Feshbach resonance state, and the other atom α being a spectator in the internal state a, is $|\phi_{\rm res}, {\rm cl}\rangle_\alpha$.

6.5.2 The matrix elements of the three-body S-operator

We now require a method for calculating the S-matrix for scattering events involving three atoms. We begin by considering only the scattering process where atoms in channel α, consisting of a pair in the $m^{\rm th}$ bound state supported by V_α and a third free particle, $|\boldsymbol{q}, \phi_m\rangle_\alpha$, interact and develop into the configuration described by channel β and in the n^{th} bound state supported by the interaction V_β, $|\boldsymbol{q}, \phi_n\rangle_\beta$. We refer to this as rearrangement scattering, and the matrix-elements are given by

$$S_{\beta n,\alpha m}(\boldsymbol{q'};\boldsymbol{q}) = \lim_{t\to\infty} {}_\beta\langle \boldsymbol{q}, \phi_n | e^{ih_\beta t} e^{-iHt} | \boldsymbol{q}, \phi_m + \rangle_\alpha. \tag{6.10}$$

Making use of the fact that $|\boldsymbol{q}, \phi_n\rangle_\beta$ and $|\boldsymbol{q}, \phi_m+\rangle_\alpha$ are eigenstates of h_β and H respectively and that the latter is a scattering state defined as

$$|\boldsymbol{q}, \phi_m+\rangle_\alpha = \lim_{\epsilon\to 0} \; i\epsilon\, G(E_m + i\epsilon) |\boldsymbol{q}, \phi_m\rangle_\alpha, \tag{6.11}$$

we can rewrite eq. (6.10) as

$$S_{\beta n,\alpha m}(\boldsymbol{q'};\boldsymbol{q}) = \lim_{\substack{t\to\infty \\ \epsilon\to 0}} \; e^{i(E_{\beta n} - E_{\alpha m})t} \, {}_\beta\langle \boldsymbol{q'}, \phi_n | i\epsilon\, G(E_{\alpha m} + i\epsilon) | \boldsymbol{q}, \phi_m \rangle_\alpha. \tag{6.12}$$

Using similar arguments we also have

$$S_{\beta n,0}(\boldsymbol{q'};\boldsymbol{q},\boldsymbol{p}) = \lim_{\substack{t\to\infty \\ \epsilon\to 0}} \; e^{i(E_{\beta n} - E_0)t} \, {}_\beta\langle \boldsymbol{q'}, \phi_n | i\epsilon\, G(E_0 + i\epsilon) | \boldsymbol{q}, \boldsymbol{p} \rangle_0, \tag{6.13}$$

$$S_{0,\alpha m}(\boldsymbol{q'},\boldsymbol{p'};\boldsymbol{q}) = \lim_{\substack{t\to\infty \\ \epsilon\to 0}} \; e^{i(E_0 - E_{\alpha n})t} \, {}_0\langle \boldsymbol{q'}, \boldsymbol{p'} | i\epsilon\, G(E_{\alpha n} + i\epsilon) | \boldsymbol{q}, \phi_n \rangle_\alpha, \text{ and} \tag{6.14}$$

$$S_{0,0}(\boldsymbol{q'},\boldsymbol{p'};\boldsymbol{q},\boldsymbol{p}) = \lim_{\substack{t\to\infty \\ \epsilon\to 0}} \; e^{i(E_{0f} - E_{0i})t} \, {}_0\langle \boldsymbol{q'}, \boldsymbol{p'} | i\epsilon\, G(E_{0i} + i\epsilon) | \boldsymbol{q}, \boldsymbol{p} \rangle_0; \tag{6.15}$$

representing three-body recombination, break up and free-free scattering respectively. Here the subscripts 'i' and 'f' have been introduced to remove the ambiguity in whether we are talking about the energy of the initial or final partition with all atoms unbound ie. $E_{0i} = \frac{3}{4}\frac{\boldsymbol{q}^2}{2\mu} + \frac{\boldsymbol{p}^2}{2\mu}$ and $E_{0f} = \frac{3}{4}\frac{\boldsymbol{q'}^2}{2\mu} + \frac{\boldsymbol{p'}^2}{2\mu}$. In our model the subscript 0 indicates that all three of the atoms are free, in the spin state $|{\rm bg}\rangle$, and as such $|\boldsymbol{q},\boldsymbol{p}\rangle_0$ is an eigenstate of h_0.

6.5.3 The transition operator $U_{\beta\alpha}$

Following the method of [54] we use the resolvent equations:

$$G(z) = g_\alpha(z) + g_\alpha(z)\overline{V}_\alpha G(z), \text{ and} \tag{6.16}$$

$$G(z) = g_\alpha(z) + G(z)\overline{V}_\alpha g_\alpha(z). \tag{6.17}$$

Inserting eq. (6.16) into eq.(6.17) we can write the full three-body Green's function as the set of equations

$$G(z) = g_\beta(z)\delta_{\alpha\beta} + g_\beta(z)U_{\beta\alpha}(z)g_\alpha(z), \text{ and} \tag{6.18}$$

$$U_{\alpha\beta}(z) = (1-\delta_{\alpha\beta})(z-h_0) + V - V_\alpha - V_\beta + \delta_{\alpha\beta}V_\alpha + \overline{V_\beta}G(z)\overline{V_\alpha}, \tag{6.19}$$

where $\overline{V_\alpha} = V - V_\alpha = \sum_{\beta=1}^{\beta=3} V_\beta - V_\alpha$. By using eqs. (6.16) and (6.17), one can show that the transition operators can be expressed as the coupled equations

$$U_{\alpha\beta}(z) = (1-\delta_{\beta\alpha})(z-h_0) + \sum_{\substack{\gamma \\ \gamma\neq\alpha}} U_{\beta\gamma}(z)g_\gamma(z)V_\gamma(z), \text{ and} \tag{6.20}$$

$$U_{\alpha\beta}(z) = (1-\delta_{\beta\alpha})(z-h_0) + \sum_{\substack{\gamma \\ \gamma\neq\beta}} V_\gamma(z)g_\gamma(z)U_{\gamma\alpha}(z). \tag{6.21}$$

The motivation for this partitioning of the Green's function in eq. (6.18) becomes clear when we use it to evaluate eq. (6.12)

$$\begin{aligned} S_{\beta n,\alpha m}(\boldsymbol{q'};\boldsymbol{q}) = \lim_{\substack{t\to\infty \\ \epsilon\to 0}} e^{i(E_{\beta n}-E_{\alpha m})t}\langle \boldsymbol{q'}, \phi_n | i\epsilon\, g_\beta(E_{\alpha m}+i\epsilon)\delta_{\alpha\beta}|\boldsymbol{q},\phi_m\rangle \ldots \\ + \ \langle \boldsymbol{q'}, \phi_n | i\epsilon\, g_\beta(E_{\alpha m}+i\epsilon)U_{\beta\alpha}(E_{\alpha m}+i\epsilon)g_\alpha(E_{\alpha m}+i\epsilon)|\boldsymbol{q},\phi_m\rangle. \end{aligned} \tag{6.22}$$

The first term of eq. (6.22) is the matrix element of an operator that is diagonal in the partition indices α and β, it has been extracted from the full Green's function and, on-shell, represents the process where no scattering takes place. Hence, unlike some other formulations, no off diagonal (in α and β) parts of G are lost from the second term which represents scattering. The result of this is a greater symmetry in the resulting

equations. Evaluating eq. (6.22), and the similar expressions for eqs. (6.13-6.15) gives

$$\begin{aligned}
S_{\beta n,\alpha m}(\boldsymbol{q'};\boldsymbol{q}) =&\delta_{\alpha\beta}\delta_{mn}\delta(\boldsymbol{q'}-\boldsymbol{q})\dots \\
&- 2\pi i\delta(E_{\beta n}-E_{\alpha m})\,{}_\beta\langle \boldsymbol{q'},\phi_n|U_{\beta\alpha}(E_{\alpha m}+i0)|\boldsymbol{q},\phi_m\rangle_\alpha, && (6.23)\\
S_{\beta n,0}(\boldsymbol{q'};\boldsymbol{q},\boldsymbol{p}) =&-2\pi i\delta(E_{\beta n}-E_0)\,{}_\beta\langle \boldsymbol{q'},\phi_n|U_{\beta 0}(E_0+i0)|\boldsymbol{q},\phi\rangle_0, && (6.24)\\
S_{0,\alpha m}(\boldsymbol{q'},\boldsymbol{p'};\boldsymbol{q}) =&-2\pi i\delta(E_0-E_{\alpha m})\,{}_0\langle \boldsymbol{q'},\boldsymbol{p'}|U_{0\alpha}(E_{\alpha m}+i0)|\boldsymbol{q},\phi_m\rangle_\alpha, \text{ and} && (6.25)\\
S_{0,0}(\boldsymbol{q'},\boldsymbol{p'};\boldsymbol{q},\boldsymbol{p}) =&\delta(\boldsymbol{q'}-\boldsymbol{q})\delta(\boldsymbol{p'}-\boldsymbol{p})\dots \\
&- 2\pi i\delta(E_{0i}-E_{0f})\,{}_0\langle \boldsymbol{q'},\boldsymbol{p'}|U_{00}(E_{0i}+i0)|\boldsymbol{q},\boldsymbol{p}\rangle_0 && (6.26)
\end{aligned}$$

respectively.

It is now clear that on the energy shell the operator $U_{\beta\alpha}(z)$ gives useful information about the S-matrix, having removed the three-body kinematical delta-functions. $U_{\beta\alpha}(z)$ off-shell is also sometimes useful, for example in order to analyse three-body recombination we make use of the rearrangement transition operator half off-shell. This is because we find it convenient to first consider $U_{\beta\alpha}$, $(\alpha,\beta\neq 0)$, and then use eqs. (6.20 & 6.21) to recover any other process that we may be interested in.

6.5.4 Probing Efimov states

For the kind of well behaved Born-Oppenheimer potentials that we have considered in this work, there exist a finite number of bound states supported by that potential [56]. Surprisingly, under certain conditions, three particles interacting pairwise via these same potentials can give rise to an infinite number of bound states. This is often referred to as Efimov's effect [39]. In fact it can be demonstrated mathematically that if the scattering length is infinite then the number of bound states $N(E)$ which are lower in energy than E increases logarithmically as $E\to 0$ as [39]

$$\lim_{E\to 0} N(E) \propto \ln(|E|). \tag{6.27}$$

Expressed another way: the number of bound states existing between any negative energy and the threshold $E=0$ is infinite. A further striking characteristic is related to the relative depth of successive bound states, which obey

$$\lim_{n\to\infty}\frac{E_{n+1}}{E_n}\approx\frac{1}{515.035}. \tag{6.28}$$

When the scattering length is large in magnitude, but finite, the shadow of this affect can be seen. The bound states vary smoothly in energy as the scattering length is changed. Figure 6.7 gives a cartoon sketch of the continuation of Efimov states off resonance. On the negative scattering length side of the $a_s = \infty$ limit the trimer energy levels progress towards the threshold for three free particles. At the point where the trimer state is degenerate with the threshold the three-body recombination rate peaks sharply. When the scattering length is large and positive we must include the well-known universal dimer with binding energy

$$E_{\text{dimer}} = -\frac{\hbar^2}{m a_s^2}. \tag{6.29}$$

The threshold is now the energy of one dimer, plus one free atom. For every interception of the trimer state with this atom dimer threshold there is an associated three-body recombination minimum. The minimum arises as a result of destructive interference between different decay pathways [130]. These peaks and troughs in the $K_3(a_s)$ then allow us to infer the existence of underlying trimer states.

6.5.5 Calculating the three-body recombination rate

Solving the system of equations (6.21) for our model interaction allows us to predict the dependence of the three-body recombination rate, K_3, on the applied magnetic field strength. A Fermi golden rule argument leads to the following expression for K_3 in terms of the matrix elements of the transition operators [127]

$$K_3 = \sum_n \frac{12\pi m}{\hbar}(2\pi\hbar)^6 q_f \int \mathrm{d}\Omega_f \; |\,{}_1\langle \boldsymbol{q_{fn}}, \phi_n | U_{1,0}(z) | 0 \rangle|\,. \tag{6.30}$$

The zero momentum limit of the entrance channel three body state is $|0\rangle$. This expression is for a thermal ultracold gas of identical bosons, and must be divided by 3!=6 when describing a BEC. This accounts for the zero energy limit of the entrance channel $|0\rangle$ being already symmetric with respect to permutations of the atoms [131, 132, 133]. The integral in this expression is over all possible directions of the vector $\boldsymbol{q}_{fn}$. Here we are working in the zero collisional energy limit and so the momentum in the final state $\boldsymbol{q}_{fn} = 2\sqrt{m|E_n|/3}$.

We numerically solve the for the matrix elements of $U_{1,0}$. The calculations are similar in many ways to those described in chap. 5 for the solution of the Faddeev

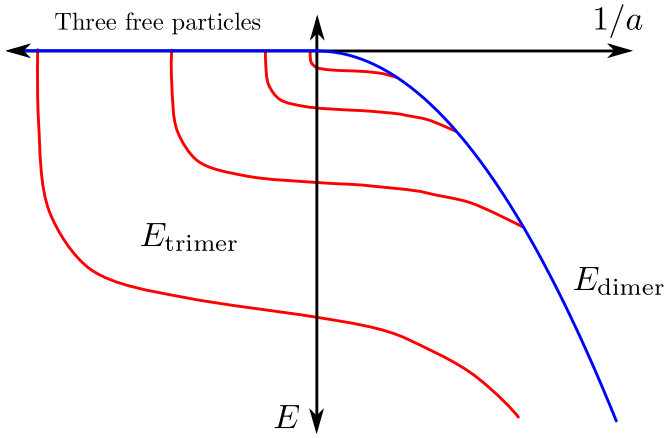

Figure 6.7: A cartoon sketch of Efimov states, see text for discussion.

equations. For a detailed explanation of what is done, including all of the intermediate algebraical detail, see ref. [127]. In summary, the problem is reduced to that of solving a set of coupled Fredholm integral equations of the second kind. The integrals are approximated using gaussian quadrature allowing linear algebra techniques to be used in gaining the solution. The kernels of the Fredholm equations contain matrix elements of the two body Green's operator, and as such contain singularities at energies corresponding to those of diatomic bound states. This provides little further complication as the singularities can be treated analytically by contour integration, leaving behind a numerically well defined and stable integral kernel. A major difference between the method used here and that used in ref. [127] is that here we use a greater number of separable terms in the expansion of the background scattering potential. This should allow background channel scattering to be better approximated. On one further point of distinction: a detailed consideration of the spin wave function under permutation of the atoms, shows that the approximation that ${}_\alpha\langle \mathrm{cl}|\mathrm{cl}\rangle_\beta = \delta_{\alpha\beta}$ is not valid here. Instead we do not neglect terms where $\alpha \neq \beta$ and instead use the form ${}_\alpha\langle \mathrm{cl}|\mathrm{cl}\rangle_\beta = 1/4 + 3\delta_{\alpha\beta}/4$, this is deduced from the coupled-channels results.

6.6 Results and discussion

The numerical results of this calculation are shown in fig. 6.8, where we compare against the published data of ref. [13]. Rather than plot K_3 versus the magnetic field strength we instead plot against the s-wave scattering length of the diatomic system using the

mapping of eq. (2.30). The agreement between experiment and theory is satisfactory on the positive scattering length side of the resonance. The experiment was performed using a sample that was in general a mixture of a BEC and a thermal gas. In order to allow for this we show curves for both of these cases individually, we indicate that the expected values lie in the shaded region between these two curves.

The position of the trough in K_3 at larger scattering length shows excellent agreement with the experimental data. Whereas the lower a trough shows only qualitative agreement. There are several possible explanations for this. Firstly there are fewer data points in this region and so it could be simply that the feature has not been sufficiently experimentally resolved. Otherwise it could be a signature of the limits facing our simplified model.

When the calculation is carried out far from the resonance the Feshbach molecular bound state, which will be the dominant recombination target state, is more deeply bound. As a result of this the wave function becomes progressively shorter range, it's properties become less universal, and it becomes more sensitive to the functional form of the interatomic potential. Our approximate model is based on accounting for the dominant pole contributions to the channel Green's functions, as well as some important scattering quantities for the parameterisation of near threshold background scattering. It does not aim to recreate the functional form of the interatomic potential explicitly, and so it does not recover the long range C_6/r^6 behaviour. If the Feshbach molecule becomes slightly shorter ranged then its wave function will be dominated by oscillations determined by the long range C_6 coefficient in the classically allowed region rather than by the exponentially decaying tail at larger internuclear separation in the classically forbidden region. This will have obvious implications for wave function overlap factors. In addition to remnant sensitivity to the functional form of the background scattering potential there is the treatment of inter-channel coupling. The preceding sections have highlighted the significant simplification in going from the full coupled channels calculation to the simplified two channel model. The form of the coupling term is entirely arbitrary and is parameterised so as to give correct values for a limited number of near threshold characteristics. This is wholly inadequate for the description of the shorter range parts of molecular wave functions which could again have a knock on effect in the calculation due to poor representation of the target states.

The good agreement between the troughs is encouraging. There is a general migration of the data points from the BEC values at lower scattering lengths to values expected for a thermal gas at higher scattering lengths. This gradual shift is expected due to heating effects within the experiment [13].

On the negative a_s side of the scattering length the story is very much different. There is no notable agreement between experiment and theory. An important comment on the experimental trace is that it fails to display the expected $K_3(a_s) \propto a_s^4$ scaling [134]. This is expected in the region of an Efimov state induced three body recombination maximum. In ref. [13] they interpret the data such that they identify two peaks. One narrower peak at larger a_s values, and a broader peak at lower a_s values. They speculate that this lower peak is due to resonant four body collisions that are analogous to the three body collisions discussed here. It is hypothesised that this peak may be obscuring the general a_s^4 scaling. It now appears that this argument is highly unlikely as these four body features have been identified clearly in the caesium system and have been found to be very narrow in comparison to their nearby trimer induced resonances [135]. We would argue that this lack of a_s^4 scaling is a strong argument suggesting that the experiment or its analysis has not succesfully extracted the K_3 coefficient. It should be pointed out that the extraction of the rate coefficient is a challenging and involved task, see the supplementary material published alongside ref. [13]. Putting these considerations aside the mentioned shortcomings in our theoretical model of course also apply to the negative scattering length side of the resonance. It is entirely possible that the detrimental effects, on accurately calculating recombination to more deeply bound target states within our model, are more significant here. There is no Feshbach molecular state on this side of the resonance and so recombination must go to more deeply bound states. Within our model we can only include the more deeply bound aa channel states. These states are still in molecular physics terms extremely weakly bound. It is however conceivable that dependence on the C_6/r^6 form is starting to have an effect. Something we have neglected throughout this work is the contribution from forces that are purely three body in nature. It has been suggested [136] that these may have an effect when trying to resolve Efimov features.

Finally, we note that a recent study [135], focussed on the caesium system, which surveyed the relationship between Efimov features observed on the positive, and negative side of resonances. They considered data reported by groups working with caesium

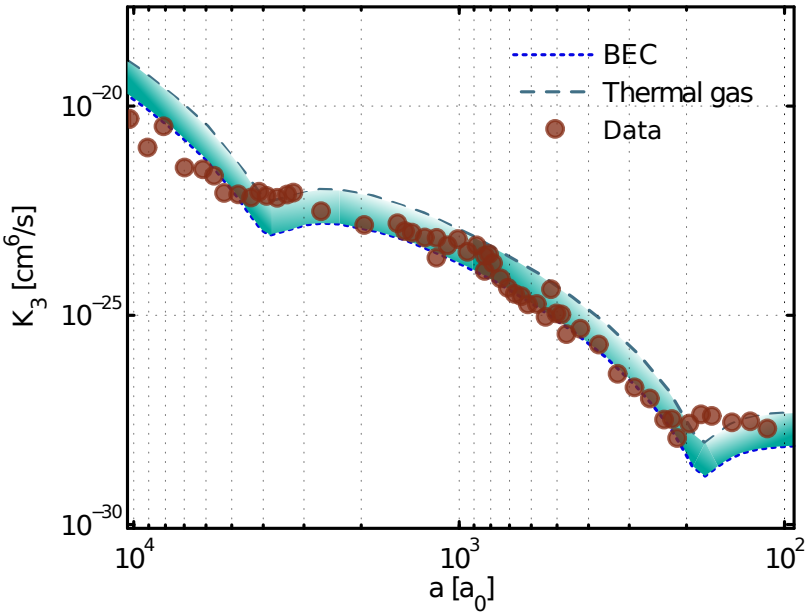

Figure 6.8: Three body recombination rate constant, K_3, versus the diatomic $s-wave$ scattering length $a(B)$. The shaded region indicates what is predicted if the gas is somewhere between a pure BEC (dotted line) and a thermal gas (dashed line). The brown circles represent experimental observations, data is supplied by M. Zaccanti [13].

and lithium alongside the potassium data. It appeared that, when analysed in the context of universal Efimov scalings, that the potassium experiment was something of an outlier.

7

Prospects for near threshold three-body calculations using realistic potential models

7.1 Introduction

In sec. 6.6 we discussed some of the limitations caused by assuming that the near threshold few body physics is insensitive to the detailed shape of the local potential. In this chapter we explore a method that I believe could be applied to exploring the effects of the details of the local Born-Oppenheimer potential on the few body physics. We will largely focus on a simplified version of a Born-Oppenheimer potential, but the arguments given in this chapter can be applied to any realistic potential, and can be used in "exact" treatments of three atom scattering.

Concerning exotic trimer states, it has been suggested [137] that the best understood Efimov system is that of ^{4}He. It benefits from being considerably simpler than the alkalis, there being no atomic hyperfine splitting, for example. Another system which is currently attracting significant attention is that of ytterbium. There are a large number of distinct isotopes that can be combined in a trapped ultracold gas experiment. Effectively the interaction strength can be tuned by altering the reduced-mass of the colliding pair. Of course, unlike with Feshbach resonances, this tuning is limited as only certain discrete reduced-masses are realisable. We shall see that the analysis introduced here is particularly suited to near threshold systems where the reduced mass can be

varied systematically.

7.1.1 Few-body calculations and separable potentials

Similar to previous chapters we define a separable potential as a potential that can be written as a summation of terms, each of which take the form $|\chi_i\rangle\langle\chi_j|$. Where the kets, $|\chi_i\rangle$, are scattering form factors. These can be chosen in many different ways [138, 139, 140, 141]. The choice depends in part on how the expansion is physically or mathematically motivated. A separable potential leads to a T-matrix represented by a sum of separable terms. This form greatly facilitates the solution of the integral equations that result from the Faddeev [53] or AGS [54] treatments of the quantum mechanical few-body problem.

A separable potential can never be introduced such that the associated T-matrix, $T(z)$ converges with, in a mathematically rigorous sense, the T-matrix derived from the local potential $T_L(z)$ [142]. The reason for this is rooted within the fact that the separable potential leads to a separable T-matrix. Unless z is in the point spectrum of $(H_0 + V)$ the T-matrix derived from the local potential is not a compact operator[1]. Whereas in the separable approximation it is compact, and so the two can never be made to rigorously converge. However our intention is to solve the few-body problem. The kernel, $K(z)$ of the relevant integral equations has the form $G_0(z)T_L(z)$. The Lippmann-Schwinger equation implies that this shares the compactness of $G_0(z)V$, which can be demonstrated by the direct calculation of its Hilbert-Schmidt operator norm [56]. The convergence of the $T(z)$ with $T_L(z)$ can be monitored for specific values of z, as a means for motivating the expansion, and testing for the convergence of the model. Ultimately, monitoring the convergence of few-body observables as separable terms are added to the potential is the true test of whether the calculation is converging. It is remarkable that this can be done exactly, even though the two-body T-matrix will never be represented exactly within this approach.

[1]For our purposes, a compact operator can be approximated by an operator of finite rank [115].

7.2 The zero energy separable expansion

7.2.1 Eigenfunction expansion of the kernel

If the potential has definite sign then the kernel can be made Hermitian for $z \leq 0$ simply by multiplying the integral equation by $\sqrt{|V|}$. As a result of this we may apply the results of the spectral theorem, and can make an expansion in the eigenfunctions of the kernel which form a complete set [140]. When the potential changes sign in places, slightly more consideration is needed. However it can be shown that polar kernels [56, 143] can be treated in much the same way. Reference [140] showed that these ideas could be expanded to cover the kernel when z is not negative real or zero.

We now make use of this spectral decomposition, but find it convenient to consider the eigenfunctions of the operator $VG_0(z)$ directly [141],

$$|\chi_{n,z}\rangle = \lambda_n(z) V G_0(z) |\chi_{n,z}\rangle, \tag{7.1}$$

the adjoint equation is

$$\langle\psi_{n,z}| = \mu_n(z) \langle\psi_{n,z}| V G_0(z). \tag{7.2}$$

Since the λ_n are real and the $|\chi_n(z)\rangle$ can be taken to be real then one can show that

$$\lambda_n(z) = \mu_n(z), \text{ and,} \tag{7.3}$$

$$|\chi_{n,z}\rangle = V|\psi_{n,z}\rangle. \tag{7.4}$$

The form factors can be calculated using the equation

$$|\psi_{n,z}\rangle = \lambda_{n,z} G_0(z) V |\psi_{n,z}\rangle. \tag{7.5}$$

For appropriate values of z this is equivalent to the bound state Schrödinger equation for the potential $\lambda_{n,z}(z)V$. We define the normalisation of the form factors by reference to the orthonormality condition

$$\langle\chi_{n,z}|G_0(z)|\chi_{m,z}\rangle = -\delta_{n,m}. \tag{7.6}$$

Given this statement it is clear that

$$|\chi_{n,z}\rangle = -\lambda_{n,z} \sum_m \frac{|\chi_{m,z}\rangle\langle\chi_{m,z}|}{\lambda_{n,z}} G_0(z)|\chi_{n,z}\rangle. \tag{7.7}$$

We choose to perform the spectral decomposition of G_0V for a particular value of z, say $z = -|x|$ where x is real, we retain the same form factors for all subsequent calculations. A comparison of eq. (7.7) with eq. (7.1) leads to an approximated potential being represented by,

$$V_{\text{sep}} = -\sum_{n=1}^{n=N} \frac{|\chi_n\rangle\langle\chi_n|}{\lambda_n}. \tag{7.8}$$

We have truncated the series after some number of terms N, which could be determined by the convergence of the three-body observables being considered.

7.2.2 Application to near threshold collisions physics

The problem is now one of choosing an appropriate set of form factors for the problem at hand. We do this by solving the eigenvalue problem associated with eqs. (7.4) and (7.5). The T-matrix, in certain regions, is dominated by the poles that correspond with bound states of the system. A common approach is to evaluate the form factors with z corresponding to the position of one of these poles [141]. We however do not follow this here.

The alternative approach that we propose is that of evaluating it in the limit that z approaches zero from below. There are now consequences for the interpretation of eq. (7.5). We may now see eq. (7.5) as being satisfied by zero-energy bound states ($l > 0$) or half bound states [56] ($l = 0$) in the mass scaled system with reduced mass $\mu_n = \lambda_n\mu$, where μ is the reduced mass of the system being considered. A preliminary test of convergence relevant for ultracold collisions is to monitor the value of the on-shell T-matrix at threshold. Equivalently, for s-wave collisions, we can analyse the convergence of the scattering length as new form factors are added. Figure 7.1 shows the sequence of divergences in the scattering length as the reduced mass is varied.

The major advantage motivating the use of eigenfunctions with $z = 0$ is that for a large class of potentials eq. (7.5) can be solved analytically [145, 146]. If this were not the case, then there would be a significant amount of numerical work required in order to obtain the form factors.

7.2.3 Mass scaling in the model interaction

The eigenvalue λ_n tells us how much the reduced mass would have to change by, in order for there to be to a bound state degenerate with the scattering threshold. A property

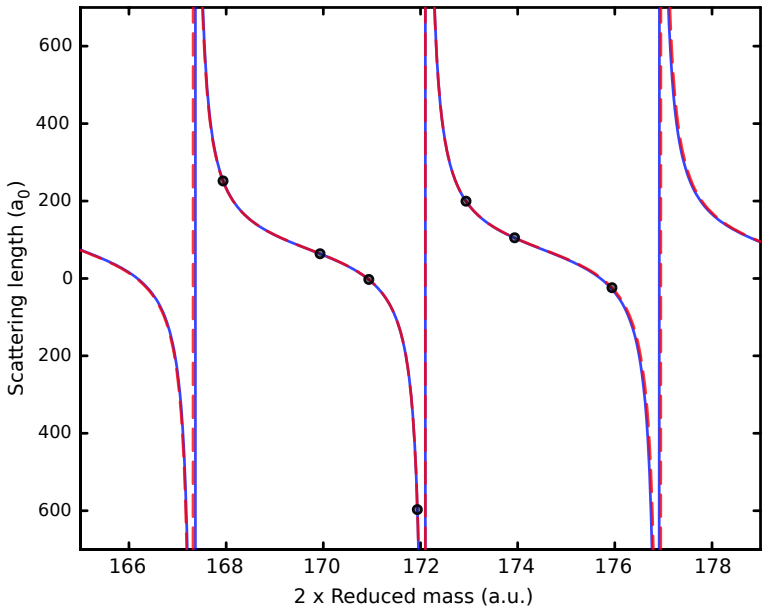

Figure 7.1: The s-wave scattering length calculated using the Yb potential of ref. [144] as the reduced mass of the colliding atoms is varied continuously (solid blue line). The circles show the physically realisable combinations using pairs of identical bosons. The dashed red line is the scattering length produced using the C_6 and flat bottom potential, set up to mimic the ^{172}Yb system.

of this approximate interaction is that if one were to consider continuously changing the mass of the system, then this interaction would correctly recover the divergences in the scattering length. The bound state and scattering state wave functions in the vicinity of the divergence would also be exactly recovered. In the limit of $N \to \infty$ then the value of the scattering length would also be correct at intermediate reduced-masses. We also note that apart from a trivial dependance of the λ_n on μ the approximate interaction would not need to be recalculated for each isotopic combination (assuming that the original Born-Oppenheimer interaction exhibited mass-scaling). In this sense the approximate interaction would inherit the mass scaling property of the local potential.

7.2.4 The T-matrix for $V_{\rm sep}$

By inserting $V_{\rm sep}$ into the Lippmann-Schwinger equation for the T-matrix and iterating we arrive at the expression

$$T = \sum_{n=1} \frac{|\chi_n\rangle\langle\chi_n|}{-\lambda_n} + \sum_{m,n} \frac{|\chi_m\rangle\langle\chi_m|}{-\lambda_m} G_0(z) \frac{|\chi_n\rangle\langle\chi_n|}{-\lambda_n} + \dots \ . \tag{7.9}$$

Studying this expression allows one to conclude that

$$T = \sum_{m,n} |\chi_m\rangle \Delta_{m,n}(z) \langle\chi_n|, \tag{7.10}$$

where Δ is a matrix of numbers to be determined. If we now substitute this T-matrix into the Lippmann-Schwinger equation we get

$$\begin{aligned} \sum_{m,n} |\chi_m\rangle \Delta_{m,n}(z) \langle\chi_n| = & \sum_n \frac{|\chi_n\rangle\langle\chi_n|}{-\lambda_n} \dots \\ & + \sum_n \frac{|\chi_n\rangle\langle\chi_n|}{-\lambda_n} G_0(z) \sum_{m',n'} |\chi_{m'}\rangle \Delta_{m',n'}(z) \langle\chi_{n'}|. \end{aligned} \tag{7.11}$$

Comparing coefficients here allows Δ to be determined via the solution of

$$\Delta(z) \ = -\lambda^{-1} - \lambda^{-1}\gamma\Delta(z), \tag{7.12}$$

$$[\lambda]_{m,n} = \delta_{m,n}\lambda_n, \text{ and} \tag{7.13}$$

$$[\gamma]_{m,n} = \langle\chi_m|G_0(z)|\chi_n\rangle, \tag{7.14}$$

which is

$$[-\Delta(z)^{-1}]_{m,n} = \delta_{m,n}\lambda_n + \langle\chi_m|G_0(z)|\chi_n\rangle. \tag{7.15}$$

For the special case of $z = -x$, Δ is a diagonal matrix.

7.2.5 The scattering amplitude for V_{sep}

Assuming that $V(\boldsymbol{r})$ is a central interaction we may factor out the angular dependence of the form factors and write the T-matrix elements

$$\langle \boldsymbol{r}|T(z)|\boldsymbol{r}'\rangle = \sum_{n_l,k_l} Y_l^m(\hat{\boldsymbol{r}})Y_l^m(\hat{\boldsymbol{r}'})^\dagger \chi_{n_l}(\boldsymbol{r})\Delta_{n_l,k_l}(z)\chi_{k_l}(\boldsymbol{r}'). \tag{7.16}$$

Here we have defined

$$\langle \boldsymbol{r}|\chi_n\rangle = Y_l^m(\hat{\boldsymbol{r}})\chi_n(r) = Y_l^m(\hat{\boldsymbol{r}})V(r)\psi_n(r). \tag{7.17}$$

The scattering state $|\boldsymbol{p}+\rangle$ [55] that evolves from an incident plane wave $|\boldsymbol{p}\rangle$ will be given by

$$|\boldsymbol{p}+\rangle = |\boldsymbol{p}\rangle + G_0(z)T(z)|\boldsymbol{p}\rangle. \tag{7.18}$$

Here we adopt the convention $\langle \boldsymbol{r}|\boldsymbol{p}\rangle = (2\pi\hbar)^{-3/2}e^{\frac{\boldsymbol{p}\cdot\boldsymbol{r}i}{\hbar}}$. Using the partial wave decomposition of $|\boldsymbol{p}+\rangle$, $|\boldsymbol{p}\rangle$, and $\langle \boldsymbol{r}|G_0(z)|\boldsymbol{r}'\rangle$, we see that

$$|\boldsymbol{p}\rangle = (\mu p)^{-1/2}\sum_{l,m}|E_p,l,m\rangle Y_l^m(\hat{\boldsymbol{p}})^\dagger, \tag{7.19}$$

$$|\boldsymbol{p}+\rangle = (\mu p)^{-1/2}\sum_{l,m}|E_p,l,m+\rangle Y_l^m(\hat{\boldsymbol{p}})^\dagger, \tag{7.20}$$

$$\langle \boldsymbol{r}|G_0(z)|\boldsymbol{r}'\rangle = \frac{2\mu}{\hbar}\sum_{l,m}\frac{1}{rr'}Y_l^m(\hat{\boldsymbol{r}})Y_l^m(\hat{\boldsymbol{r}'})^\dagger G_{l,p}^0(r,r'), \text{ and,} \tag{7.21}$$

$$G_{l,p}^0(r,r') = -\frac{1}{p}\hat{j}_l\left(\frac{pr_<}{\hbar}\right)\hat{h}_l^+\left(\frac{pr_>}{\hbar}\right). \tag{7.22}$$

Here the Green's function relations are obtained by contour integration [56], $\hat{h}_l^+$ and $\hat{j}_l$ are defined as in [55], $r_> = \text{Max}\{r,r'\}$ and $r_< = \text{Min}\{r,r'\}$. With the definition

$$\langle \boldsymbol{r}|E,l,m+\rangle = i^l\left(\frac{2\mu}{\pi p\hbar}\right)\frac{1}{r}Y_l^m(\hat{\boldsymbol{r}})\psi_{l,p}^{(+)}(r), \tag{7.23}$$

we can write the partial wave Lippmann-Schwinger equation as

$$\psi_{l,p}^{(+)}(r) = \hat{j}_l\left(\frac{pr}{\hbar}\right) + \frac{2\mu}{\hbar}\int_0^\infty G_{l,p}^0(r,r')V(r')\psi_{l,p}^{(+)}(r')\,\mathrm{d}r'. \tag{7.24}$$

By taking the limit that r tends to infinity and comparing with

$$\lim_{r\to+\infty}\psi_{l,p}^{(+)}(r) = \hat{j}_l\left(\frac{pr}{\hbar}\right) + \frac{p}{\hbar}f_l(p)\hat{h}_l^{(+)}\left(\frac{pr}{\hbar}\right), \tag{7.25}$$

we get the following expression for the partial wave scattering amplitude,

$$f_l(p) = -\frac{2\mu}{p^2}\int_0^\infty \hat{j}_l\left(\frac{pr}{\hbar}\right) V(r)\psi_{l,p}^{(+)}(r)\,\mathrm{d}r. \tag{7.26}$$

This is related to the scattering amplitiude in:

$$\lim_{r\to+\infty}\langle \boldsymbol{r}|\boldsymbol{p}+\rangle = (2\pi\hbar)^{-3/2}\left(e^{i\boldsymbol{p}\cdot\boldsymbol{r}/\hbar} + f(p\hat{\boldsymbol{r}}\leftarrow\boldsymbol{p})\frac{1}{r}e^{ipr/\hbar}\right) \tag{7.27}$$

by $f(p\hat{\boldsymbol{r}}\leftarrow\boldsymbol{p}) = \sum_l (2l+1)f_l(p)P_l(\hat{\boldsymbol{p}}'\cdot\hat{\boldsymbol{p}})$.

By inserting the T-matrix (7.16) into the eq. (7.18) and performing the partial wave decomposition we arrive at

$$\begin{aligned}\psi_{l,p}^{(+)}(r) &= \hat{j}_l\left(\frac{pr}{\hbar}\right) + \frac{2\mu}{\hbar}\ldots \\ &\int_0^\infty\int_0^\infty r'r''G_{l,p}^0(r,r')\sum_{m,n}\chi_m(r')\Delta_{m,n}(\frac{p^2}{2\mu})\chi_n(r'')\hat{j}_l\left(\frac{pr''}{\hbar}\right)\,\mathrm{d}r'\mathrm{d}r.\end{aligned} \tag{7.28}$$

Once again taking the limit of $r\to\infty$ we obtain

$$\begin{aligned}f_l(p) &= -\frac{2\mu}{p^2}\ldots \\ &\int_0^\infty\int_0^\infty \mathrm{d}r\mathrm{d}r''\,rr'\sum_{n,m}\chi_{n,l}(r)\Delta_{n,m}\left(\frac{p^2}{2\mu}\right)\chi_{m,l}(r')\hat{j}_l\left(\frac{pr}{\hbar}\right)\hat{j}_l\left(\frac{pr'}{\hbar}\right).\end{aligned} \tag{7.29}$$

Taking the limit of zero collision energy, and taking advantage having set up the form factors at $x=0$ (where Δ is diagonal), we arrive at the following expressions for the scattering length a_l:

$$a_l = -\frac{\hbar}{p}^{2l} f_l(p), \tag{7.30}$$

$$a_l = \frac{1}{(2l+1)!!}\sum_n \frac{\omega_{n,l}^2}{\lambda_n(\mu)-1},\ \text{where} \tag{7.31}$$

$$\omega_{n,l} = 2\mu\int_0^\infty \chi_{n,l}(r)r^{l+2}\,\mathrm{d}r. \tag{7.32}$$

Here the usual caveats regarding the long range nature of the potential and the magnitude of l apply [55]. Due to the normalisation requirements and definition of χ the integral (7.32) is actually independant of μ. The only mass dependence of the scattering length in this parameterisation is the simple dependence of $\lambda_n(\mu) = \mu_n/\mu$.

7.3 Evaluating the two-body T-matrix

7.3.1 Insensitivity to the details of the short range potential

Having said that we want to discuss the contributions made by the detailed form of the interaction, we start by including the long range C_6/r^6 contribution. Approximate treatments can be highly effective in the analysis of ultracold collisions. As demonstrated in chap. 3 quantum defect theories have been put to good effect in the study of ultracold gases. Crucial is the distinct separation in energy scales when it comes to solving the Schrödinger equation near to the scattering threshold. The inner region of the potential is deep, propagation of the time independent wave function is well approximated by the WKB solution, and can be seen to depend only weakly on energy [146]. A logical conclusion to draw is that any potential that gives the correct short range phase shift and has the correct asymptotic behaviour is a good starting point when modelling realistic interactions in ultracold gases. In order for the simplified interaction to inherit the mass scaling of the Born-Oppenheimer potential, i.e., the same potential can be used for different isotopes, then Levinson's theorem [56] must be taken into account. This implies that the simplified potential must contain the same number of bound states as the original detailed Born-Oppenheimer potential.

A potential that models the inner phase shift and recovers the correct long range form of the interaction is the following:

$$V_m(r) = \begin{cases} -C_6/r_{\rm m}^6 & ,\text{for } r \leq r_{\rm m} \\ -C_6/r^6 & ,\text{for } r \geq r_{\rm m}. \end{cases} \tag{7.33}$$

Here $r_{\rm m}$ is a parameter, fixed at a value that gives the model interaction the correct number of bound states, and the correct scattering length. With these two constraints we can expect the model to represent, within a good approximation, the physical properties of near threshold collisions and highly excited molecular bound states, whilst maintaining the correct form where it is most likely to have an effect.

Figure 7.2 shows the potential of ref. [144] and our simplified version, it also presents the wave functions of their respective highest bound states. It is immediately obvious that in the outer region these wave functions are virtually indistinguishable. In this plot the main difference between the wave functions is that there is no strongly repulsive core in our simplified version meaning that the wave function is present at lower internuclear

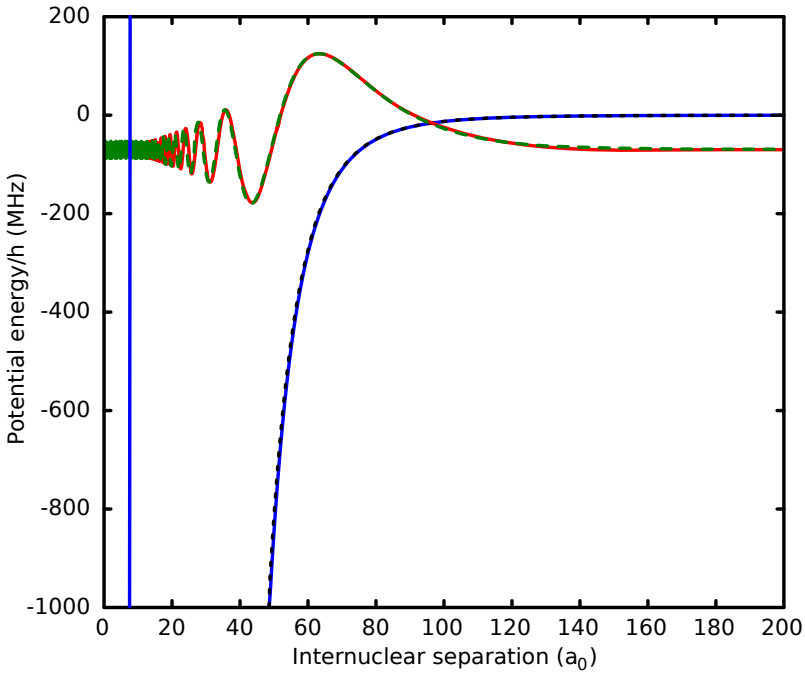

Figure 7.2: Red line: A bound state wave function supported by the Lennard-Jones potential. Green line: The corresponding flat-bottom-C_6 wavefuntion 1% higher in energy. Blue line: The Lennard-Jones potential, the remaining line is the C_6 flat bottom model.

separations. At small separations the amplitude is seen to be very small and so we assume that this will not prove to be critical.

7.3.2 Modeling the form factors

Figure (7.1) illustrates the behaviour of the s-wave scattering length as the reduced mass varies. Dominant features in this behaviour are the divergences when a bound state is close to the scattering threshold. We compare the scattering length derived from the potential of ref. [144] to that which we obtain using our simplified flat bottom-C_6 potential. It is clear that the difference between the two is small. The parameter $r_{\rm m}$ has been selected such that it places the central divergence at the correct mass value.

We are now in a position to give the explicit form of the form factors used to represent our simplified local potential,

$$\chi_{n,l}(r) = N_{n,l} \begin{cases} \frac{1}{r} V_n(r) i^l \sqrt{\frac{2\mu_n}{\hbar}} \sqrt{\frac{1}{2\hbar}} \sqrt{r} J_{l+1/2}(k_n r) & , \\ \text{for } r \leq r_{\rm m}, & \\ & \\ \zeta_{n,l} \frac{1}{r} V_n(r) i^l \sqrt{\frac{2\mu_n}{\hbar}} \sqrt{\frac{1}{2\hbar}} \sqrt{r} J_{(2l+1)/4}\left(\bar{k}_n / r^2\right) & , \\ \text{for } r \geq r_{\rm m}, & \end{cases} \tag{7.34}$$

with $\zeta_{n,l}$, k_n, and $\bar{k}_n$ being constants given by

$$\zeta_{n,l} = \frac{J_{l+1/2}\left(k_n r_n\right)}{J_{(2l+1)/4}\left(\bar{k}_n / r_n^2\right)}, \tag{7.35}$$

$$k_n = \sqrt{\frac{2\mu_n C_6}{r_n^6}}, \text{ and} \tag{7.36}$$

$$\bar{k}_n = \sqrt{\frac{2\mu_n C_6}{4\hbar^2}}, \text{ respectively.} \tag{7.37}$$

The set of normalisation constants N_n are determined by the condition (7.6).

From our previous few body calculations we expect that an important task is to obtain the matrix elements $\langle \chi_m | G_0(z) | \chi_n \rangle$. Separating out partial-waves we consider

$$\langle \chi_{m,l} | G_0 \left(\frac{p^2}{2\mu} \right) | \chi_{n,l} \rangle = - \frac{2\mu}{\hbar p} \ldots \int_0^\infty {\rm d}r' \int_0^\infty {\rm d}r \; r r' \hat{j}_l \left(\frac{p r_<}{\hbar} \right) \hat{h}_l^+ \left(\frac{p r_>}{\hbar} \right) \chi_{n,l}(r') \chi^\dagger_{m,l}(r). \tag{7.38}$$

It now makes sense to split this integral over the r-r' plane into rectangular sections, allowing the simpler region where the potential is flat, to be treated analytically.

$$\langle \chi_{m,l}|G_0\left(\frac{p^2}{2\mu}\right)|\chi_{n,l}\rangle = -(I_1+I_2+I_3+I_4), \tag{7.39}$$

where the individual portions are given by

$$I_1 = \int_0^{r_m} dr\ r g_{1,n}(r)\chi_{m,l}(r), \tag{7.40}$$

$$I_2 = \int_{r_n}^{\infty} dr\ r g_{3,n}(r)\chi_{m,l}(r), \tag{7.41}$$

$$I_3 = \int_{r_n}^{\infty} dr'\ r' g_{3,m}(r')\chi_{n,l}(r'), \tag{7.42}$$

$$I_4 = \int_{r_n}^{\infty} dr'\ r' g_{2,m}(r')\chi_{n,l}(r'), \text{ and} \tag{7.43}$$

$$I_5 = \int_{r_m}^{r_n} dr\ r g_{1,n}(r)\chi_{m,l}(r). \tag{7.44}$$

The inner integrals have been replaced with the functions

$$\begin{aligned} g_{1,n}(r) =& \frac{1}{p}\hat{h}_l^+\left(\frac{pr}{\hbar}\right)\int_0^r dr'\ r'\chi_{n,l}(r')\hat{j}_l\left(\frac{pr'}{\hbar}\right) + \dots \\ & \frac{1}{p}\hat{j}_l\left(\frac{pr}{\hbar}\right)\int_r^{r_n} dr'\ r'\chi_{n,l}(r')\hat{h}_l^+\left(\frac{pr'}{\hbar}\right), \end{aligned} \tag{7.45}$$

$$\begin{aligned} g_{2,m}(r') =& \frac{1}{p}\hat{h}_l^+\left(\frac{pr'}{\hbar}\right)\int_{r_m}^{r'} dr\ r\chi_{m,l}(r)\hat{j}_l\left(\frac{pr}{\hbar}\right) + \dots \\ & \frac{1}{p}\hat{j}_l\left(\frac{pr'}{\hbar}\right)\int_{r'}^{\infty} dr\ r\chi_{m,l}(r)\hat{h}_l^+\left(\frac{pr}{\hbar}\right), \text{ and} \end{aligned} \tag{7.46}$$

$$g_{3,n}(r) = \frac{1}{p}\hat{h}_l^+\left(\frac{pr}{\hbar}\right)\int_0^{r_n} dr'\ r'\chi_{n,l}(r')\hat{j}_l\left(\frac{pr'}{\hbar}\right), \tag{7.47}$$

where the further subdivisions are motivated by the case distinction in the partial wave greens function eq. (7.22).

Figure 7.3 show how well the scattering length is recreated as the number of eigenfunctions in the expansion of V_{sep} is increased. It is clear the representation is very bad unless the the V_{sep} has enough terms to reproduce the correct number of bound states. This is because the scattering length is strongly influenced by its divergences for larger and smaller mass combinations, see fig. 7.1. After the immediate divergences have been included the scattering length then converges as extra form factors are added.

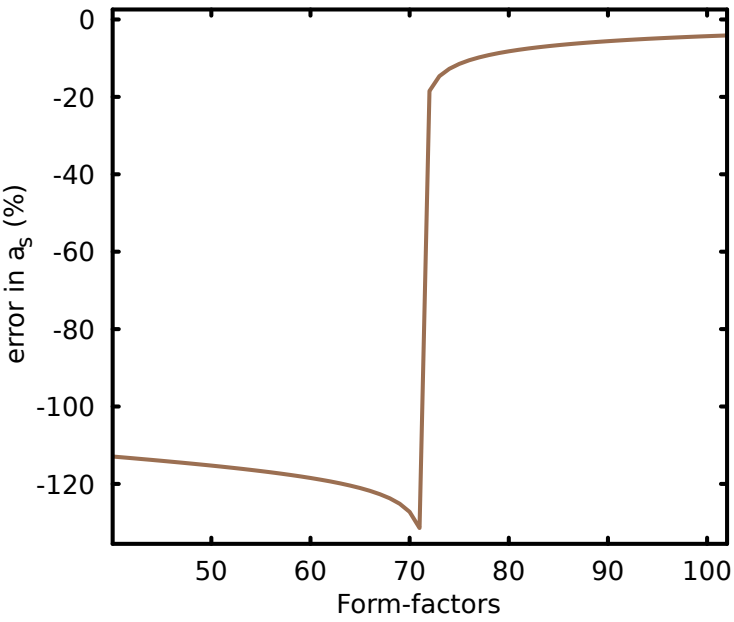

Figure 7.3: The convergence of the scattering length for the separable expansion as the number of form factors is increased. The sudden jump marks the number of form factors required to recreate all of the s-wave bound states supported by the potential.

7.3.3 Iterative corrections to the T-matrix

One interesting thing that has arisen from our discussion is that there is a one to one correspondence between some of our form factors and bound states supported by the potential. For a given mass system, μ, each of the λ_n that correspond to a critical mass $\mu_c < \mu$ adds a bound state to the system. The terms with larger critical masses do not add further bound states. So in this sense we can add bound states one by one into our system until we reach the highest excited state. Also, we have analytical expressions for the terms in the potential required to do this. It is possible to prove [56, 140] that if neither V or $-V$ supports bound states, then the kernel has a convergent Neumann series. Consequently the series can be used to calculate the corresponding T-matrix. Similarly if we weaken our potential so that it no longer can support bound states the remnant interaction can be treated iteratively. So if $V = V_{\rm rem} + V_{\rm sep}$, where $V_{\rm sep}$ has at least as many terms as V supports bound states, the Lippman-Schwinger equation for the T-matrix becomes

$$T(z) = V_{\rm rem} + V_{\rm sep} + V_{\rm rem}G_0(z)T(z) + V_{\rm sep}G_0(z)T(z). \tag{7.48}$$

If we multiply both sides from the left by $[1 - V_{\rm rem}G_0(z)]$ and rearrange we get

$$T(z) = T_{\rm rem}(z) + [1 - V_{\rm rem}G_0(z)]^{-1}V_{\rm sep}[1 + G_0(z)T(z)]. \tag{7.49}$$

Here we have identified $T_{\rm rem}(z) = [1 - V_{\rm rem}G_0(z)]^{-1}V_{\rm rem}$ as a remnant T-matrix. We now use the relation

$$[1 - V_{\rm rem}G_0(z)]^{-1} = 1 + T_{\rm rem}(z)G_0(z) \tag{7.50}$$

to rewrite eq. (7.49) as

$$\begin{aligned}[1 + G_0(z)T(z)] =&[1 + G_0(z)T_{\rm rem}(z)]\dots \\ &+ G_0(z)[1 + T_{\rm rem}(z)G_0(z)]V_{\rm sep}[1 + G_0(z)T(z)].\end{aligned} \tag{7.51}$$

By inserting our expression (7.8) for $V_{\rm sep}$, and performing some matrix algebra, we arrive at our final expression for the T-matrix

$$T(z) = T_{\rm rem}(z) + \sum_{ij} |\overline{\chi}_i(z)\rangle \overline{\Delta}_{ij}(z) \langle\overline{\chi}_j(z)|. \tag{7.52}$$

Here we have introduced

$$|\overline{\chi}_i(z)\rangle = [1 + T_{\rm rem}(z)G_0(z)]|\chi_i\rangle, \tag{7.53}$$

and,

$$[-\overline{\Delta}(z)]^{-1}_{ij} = \delta_{ij} + \langle\chi_i|G_0(z)|\overline{\chi}_j(z)\rangle. \tag{7.54}$$

The level of approximation now comes down to how many terms we include from the series

$$T_{\rm rem}(z) = \sum_{n=0}^{\infty}[V_{\rm rem}G_0(z)]^n V_{\rm rem}. \tag{7.55}$$

We now see the effect on the convergence of the scattering length with the number of form factors used in $V_{\rm sep}$, with a first order approximation to $T_{\rm rem}$, that is

$$T_{\rm rem}(z) \approx V_{\rm rem}. \tag{7.56}$$

We apply this directly to eq. (7.52) with $V_{\rm rem}$ being the difference between our separable approximation and the local potential. Because of the local nature of the potential this results in having to evaluate numerically a set of integrals over three dimensional space. A more convenient approach can be arrived at if we recognise that $V_{\rm rem}$ is made up of the terms that we have neglected in our expansion using a complete set of functions,

$$V_{\rm rem} = -\sum_{n=N}^{\infty}\frac{|\chi_n\rangle\langle\chi_n|}{\lambda_n}. \tag{7.57}$$

The first order correction now only involves using $\langle\chi_m|G_0(z)|\chi_n\rangle$, which we have already calculated.

Figure 7.4 shows the convergence properties of the separable model using the different first order approximations to $T_{\rm rem}$. We see that the rate of convergence is significantly improved in both cases. When we use the local potential directly it is equivalent to using (7.57) with an infinite number of terms. It is not surprising, therefore, that it gives the higher rate of convergence. The numerical difficulty in calculating it, though, is significant. The use of the separable remnant interaction is far simpler to implement, and it does increase convergence significantly. The maximum accuracy is of course bounded by the accuracy of the expansion of the potential. So one might ask what the point of using the iterative form is, when one could just keep all of the separable terms in $T_{\rm sep}$ and achieve the same accuracy. The answer, of course, is that it reduces

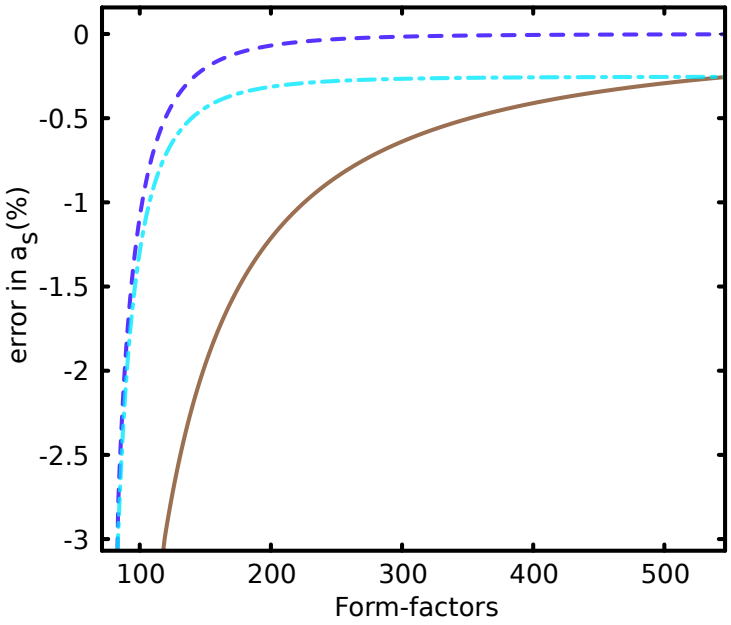

Figure 7.4: The convergence of the scattering length for the separable expansion using different first order corrections to the T-matrix. The dashed line uses the first order local potential correction, the dash dot line uses the first order separable correction assuming 540 form factors, the solid line has no first order correction and represents the continuation of the line shown in fig. 7.3. The convergence of the first order separable correction is bounded by the convergence of the solid line at 540 form factors.

the dimensionality of the matrices that have to be inverted when constructing the two body T-matrix. Carrying out a summation is significantly more efficient than performing matrix operations. A further point is that it would not be difficult to go beyond first order in this correction. This would be prohibitively difficult however when using the potential in its local form due to the dimensionality of the integrals that would have to be carried out. Finally, the separation of the bound state terms will also have beneficial consequences for calculating the three body transition operators [54].

7.4 Outlook

We have demonstrated in detail, an efficient and systematic method for representing inter atomic interactions using realistic Born-Oppenheimer potentials. We have dis-

cussed their application to systems where many different reduced masses are available. The method leads to a formulation of the T-matrix that depends only trivially on the reduced mass of the interacting particles, and is particularly suited to the study of the three body problem. The remaining difficulties to be worked out are purely numerical. The main task being the systematic calculation of the matrix elements $\langle\chi_m|G_0(z)|\chi_n\rangle$ for the relevant values of z.

7. PROSPECTS FOR NEAR THRESHOLD THREE-BODY CALCULATIONS USING REALISTIC POTENTIAL MODELS

8

Conclusions and Outlook

This thesis has focussed on Feshbach resonances and their application in experiments utilising ultracold gases. We have developed new computer codes, and analytical models, to describe the interaction of two and three atoms at low temperature in the presences of magnetic fields and laser fields. In this chapter we summarise the results so far and point out possible next steps for this research.

In chapter three we constructed a new numerically solved model for collisions involving potassium atoms in the presence of a magnetic field. We made detailed comparisons of the resulting data with both new experimental measurements and simplified near threshold models. We found that our model was extremely robust and could characterise resonances in a manner that fitted well with empirical observations. The computer codes developed to make these molecular and scattering calculations are, of course, not restricted to potassium. It has been applied to other systems not discussed here. Mainly these calculations aimed at testing the code, but also to support the work of experimental groups. In particular we applied the code to heteronuclear collisions between sodium and potassium with the intention of aiding the discovery of new Feshbach resonances. This would not only yield the obvious benefits of magnetic tuneability but would provide much needed near threshold information for the fine-tuning of Born-Oppenheimer potentials.

The fourth chapter took the model of atoms in a magnetic field one step further. We considered what would happen if, after the Feshbach molecules had been associated via a magnetic sweep, a laser pulse was applied. We successfully modelled the photodissociation of weakly bound Feshbach molecules. This allowed us to fully explain new

experimental observations. Further to this, our analysis allowed the experimental data to be used as a spectroscopic tool. It allowed us to construct a new Born-Oppenheimer potential. New analytical results based on a semi-classical approximation were derived. The semi-classical description paved the way for a direct measurement of the height of the potential barrier in the final state interaction potential. Again the code developed to calculate photodissociation rates is not limited to this particular molecule. This method could in principle be used to gain information about electronically excited state diatomic potentials for other alkali metal species. A separate point is that this work helps to optimise optical lattice wavelengths; this can only help increase the longevity and accuracy of experiments.

Chapter 5 gave an introduction to how we go about solving the three body problem for an atomic system. We used a pseudo-potential model to describe ^{4}He – comparing the results to more detailed theoretical calculations, and empirical data. Despite its simplicity, the pseudo-potential was able to qualitatively reproduce two and three body properties. Here we also gave an account of the resulting integral equations and discussed their numerical solution. Similar methods are later applied in the study of ^{39}K.

Three body recombination is the subject of chapter 6. Specifically its use to probe Efimov states. We extended the methods described in chapter 5, combined with the two channel Feshbach resonance model of chapter 2. This gave a two channel model for the two body physics, where the channel Hamiltonians had potential terms represented by pseudo-potentials. We solved the AGS equations numerically, calculating the three body recombination rate. Our predicted rate compared well with experiment on the positive scattering length side of the resonance. This gives some level of confirmation that the experiment had successfully detected a signature indicating the presence of weakly bound trimer states. The negative scattering length side of the Feshbach resonance did not compare well with the empirically extracted data. We suggested some reasons why this may be the case. As we pointed out in the chapter, the methods we used here could be applied to other three body processes. An extension of this work could take the form of a detailed study of free-free scattering, or probably more interestingly: atom-dimer scattering/relaxation. Here we have taken advantage of the symmetries introduced when one has three identical bosons. It would be interesting

to set up the model for interspecies collisions or for collisions in multi spin component fermionic gases.

The seventh chapter of this thesis was an attempt to give a detailed description of how near threshold three body calculations could be carried out using more realistic pairwise potentials. We discussed the mathematical motivation behind making a separable expansion of the potential. We then went on to show the form taken by the T-matrix. We derived results important for analysing the two body physics, and discussed how changing the mass of the system affects the equations. We discussed the ytterbium system which we would see as a prime candidate for a first application of these methods. A key advantage of the expansion suggested here is that the form factors are known analytically for a large class of potentials. This could also allow further analytical work to be carried out on three body scattering, and other multichannel problems.

Appendix A

Experimental determination of Feshbach resonances

A.1 Introduction

This appendix provides detailed descriptions of the experiments performed for the determination of ^{40}K Feshbach resonances. The descriptions are provided by the respective groups.

A.1.1 Amsterdam data

In Amsterdam the positions of the Feshbach resonances were determined by observing peaks in atomic loss [35]. State selective detection was used to distinguish between losses in the different spin channels. Approximately 10^6 atoms in a magnetic trap are loaded into a single pass optical dipole trap. The optical dipole trap is created by focusing 1.9 W from a fibre laser ($\lambda = 1.07$ μm) to a 19 μm waist acting as optical tweezers [66]. The transferred cloud consists of a mixture of atoms in the magnetically trappable spin states g, h, i, and j in the notation of fig. 3.1. The tweezers are then used to move the cloud into the centre of a Feshbach coil. As the cloud consists of fermions in different spin states it can be evaporatively cooled by reducing the intensity of the trapping light. Around 10^4 atoms remain at a final temperature of about 1 μK when the optical trap is released. This is verified by applying a magnetic field gradient of 100 G cm^{-1}, causing the Stern-Gerlach effect to separate the different spin states. Atom detection is carried out using standard absorption imaging.

The Feshbach measurements are made with a cloud containing just the required spin states. This requires a procedure to remove unwanted spin components. Firstly, all atoms except those in the most populated state j are removed from the sample. Unwanted states are adiabatically transferred to the upper hyperfine manifold ($f = 7/2$) using microwave sweeps, and are subsequently removed by resonant light at the $^2S_{1/2},\ f = 7/2 \rightarrow {}^2P_{3/2}, f = 5/2$ optical transition (D_2-line). Secondly, the desired states are populated by means of Landau-Zener transfers employing radio frequency sweeps at an offset field of 18 G. The remaining density of the spin mixture is about 10^{12} cm^{-3}. After holding the atoms for 1-5 s at a designated magnetic field, the Feshbach coil is switched off and a Stern-Gerlach pulse applied. Determination of the remaining fraction of atoms in each spin state was again performed using absorption imaging.

The measured loss features are listed in tables 3.1 and 3.2. The loss feature of the 102.10 G *de* resonance is shown in more detail in fig. A.1. For the cases of narrow and isolated s-wave resonances, which show a symmetric atom loss profile, the Feshbach resonance location B_0 is determined by fitting to a Lorentz function . The loss rate as a function of magnetic field was not measured. The p-wave resonances and some of the broader s-wave resonances show an asymmetric profile. Here the position of the peak in atomic loss is reported. For the broader p-wave resonances the doublet feature [62] due to magnetic dipole-dipole interactions is also resolved. The assignment to s- or p-wave resonances is simplified by state dependent detection: if only one spin state shows losses at a certain field, an s-wave resonance can be excluded in view of fermionic nature of the atoms. In general comparison with our coupled channels calculations allowed the experimentalists to unambiguously assign the channel labels of the Feshbach resonance.

A.1.2 Munich data

The widths of the Feshbach resonances were measured by observing the expansion of an *ab* mixture in a flat-bottom two-dimensional (2D) optical lattice [68]. First, the atoms are harmonically confined in a red-detuned crossed beam optical dipole trap, where typically $2 \times 10^5 - 3 \times 10^5$ atoms are evaporatively cooled to temperatures of $T/T_F = 0.13(2)$, where T_F is the Fermi temperature. Subsequently, a band-insulating state is prepared by ramping up a three-dimensional (3D) simple-cubic blue-detuned optical lattice with a depth of 8 E_R, where 1 $E_R = \hbar^2/(4\mu\lambda^2)$ is the recoil energy,

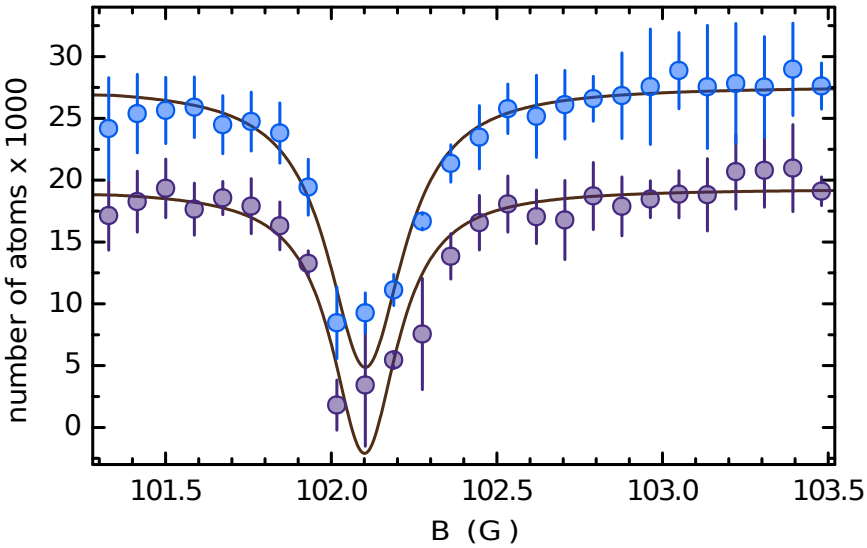

Figure A.1: Example of a loss feature around an *s*-wave resonance observed after holding a *de* spin mixture for 3 s in an optical dipole trap (expanded view of fig. 3.2). Light blue circles denote atoms in the *d* state, dark blue circles denote atoms in the *e* state. The number of atoms is recorded for both spin states and each fitted with a Lorentz distribution (solid line). The average of the centre values of the fits to the loss features is listed as the experimental value for B_0 in table 3.1. Data from A. Ludewig.

with $\lambda = 738$ nm the wavelength of the lattice light corresponding to $\lambda/2 = 369$ nm lattice spacing. By lowering the power of the red-detuned trap to about 10% of its initial power, the dipole potential is adjusted to compensate for the anti-confinement of the lattice, thus flattening the bottom of the optical lattice potential and allowing the atom cloud to expand in 3D. By increasing the vertical lattice to a depth of 20 E_R vertical tunnelling of the atoms is suppressed and the expansion can be studied under quasi-2D confinement without the influence of gravity. The loading procedure results in a well-known density distribution of the atoms with Gaussian core radius R_0 which is independent of the interactions between the atoms [68]. The core expansion velocity v_c depends on the interaction between the atoms and is varied from non-interacting to strongly interacting by varying the scattering length from zero to a very large value ($a \to \infty$) with the aid of the Feshbach resonance at 202 G. In the non-interacting limit the expansion shows the characteristic ballistic behaviour of an ideal band insulator. In the presence of interactions the core expansion velocity v_c is reduced by diffusive motion under the influence of collisions. To determine v_c the dependence of the core radius on time was measured with phase-contrast imaging, using the scaling function

$$R_c = \sqrt{R_0^2 + v_c^2 t^2}. \tag{A.1}$$

Within experimental error this function was found to describe the expansion for all interaction strengths investigated. Around the zero crossing of the Feshbach resonance ($a = 0$) the expansion velocity $v_c(B)$ shows a pronounced peak as a function of magnetic field. From the position of the peak the zero crossing of the *ab* resonance at $B_0 + \Delta B = 209.1(2)$ G was determined . The centre of the resonance B_0 was determined by measuring the loss feature in a similar fashion to the Amsterdam experiment (see A.1.1). With $B_0 = 202.1$ G, the implied width of the resonance is $\Delta B = 7.0(2)$ G. The accuracy of these measurements is limited by the magnetic field calibration. The uncertainties in determining the expansion velocities are much smaller. The vicinity of the *p*-wave resonance in the *bb* channel at 198.8 G can give rise to some broadening and shift of the function $v_c(B)$. Therefore, for measurements of the crossover from ballistic to diffusive expansion in an optical lattice an interesting alternative is offered by the *s*-wave resonance at $B_0 = 178$ G in the *cd* channel. It is well separated by 55 G from the *p*-wave resonance in the *cc* channel at $B_0 = 233$ G.

A.1.3 Zurich data

In Zurich the zero-crossing of the scattering length was determined through the observation of Bloch oscillations in an optical lattice as a function of magnetic field. At vanishing interactions these oscillations can be maintained for many thousand cycles. A small amount of interaction, however, leads to collisions, and to the dephasing of oscillations of different atoms. Thus, the dephasing of Bloch oscillations constitutes an excellent observable for locating the zero crossing, as demonstrated in [69] for the bosonic case. Combined with an independent measurement of the resonance position, it can be used to determine the resonance width. The starting point of this experiment is a degenerate Fermi gas of typically 2×10^4 atoms loaded in a one-dimensional optical lattice of depth $5E_R$, where E_R is the recoil energy. It is necessary to limit the filling of the band because of the fermionic nature of the atoms; they would otherwise lead to a complete occupation of the entire Brillouin zone (band-insulating state) and prevent observation of the oscillations. After excitation, the atoms are allowed to oscillate for up to 750 ms, and this is repeated for different values of the offset magnetic field. The quasi-momentum distribution after a time-of-flight expansion was measured. A moment is chosen where the atoms are left at the band centre after the oscillation. There, $a = 0$ corresponds to the smallest measured root mean square (rms) momentum spread. Using the literature values for B_0 [10, 61, 70, 147] and the background scattering length $a_{bg} = 174\ a_0$, with $a_0 = 0.0529$ nm the Bohr radius, a Gaussian dip was fitted to the rms momentum width:

$$q_{rms}(B) = q_0 + \Delta q \exp\left[-\frac{1}{2}\left(\frac{a_{bg}}{\Delta a}\right)^2 \left(1 - \frac{\Delta B}{B - B_0}\right)^2\right]. \tag{A.2}$$

The four remaining parameters are determined by the fit: q_0 the rms momentum for dephased oscillations, q, the maximum change in rms momentum without interactions, δa the width of the low dephasing regions around $a = 0$. The values $\Delta B = 7.5(1)$ G for the *ab* resonance at 202.1 G and $\Delta B = 7.6(1)$ G for the *ac* resonance at 224.21(5) G are obtained. The accuracy is limited by the magnetic field calibration, the uncertainty of the resonance position and the width of the dip. Compared to experimental values obtained at JILA [147], the width of the *ac* resonance differs. However, it is consistent with the value of the on-site-interaction U extracted from lattice modulation spectroscopy in a three-dimensional optical lattice [148]. Additionally there is a previously

unreported p-wave Feshbach resonance in the cc channel which shows the characteristic doublet feature due to magnetic dipole-dipole interactions [62]. With $B_0 = 232.8(2)$ G and $B0 = 233.4(2)$ G for $|m_l| = 1$ and $|m_l| = 0$ respectively. Here m_l is projection of the orbital angular momentum on the magnetic field axis. The assignment of the loss features to a p-wave resonance is confirmed by the suppression of either the $|m_l| = 0$ or the $|m_l| = 1$ resonance when the experiments are realised in a one-dimensional geometry, depending on the relative orientation of the magnetic field axis and the extension of the gas [149].

Appendix B

The $B^1\Pi_u$ potential from photodissociation spectroscopy

B.1 Construction of the potential

All parameters used to construct the potential described here are given in tables B.1 & B.2. The zero of energy is the $4^2S_{1/2} + 4^2P_{3/2}$ asymptote. The $B^1\Pi_u$ potential (and its 1_u limit) is constructed from four segments that connect smoothly at the joining radii R_i.

Firstly, representing the repulsion at very small internuclear separations we use the form

$$V_{\text{core}} = A\exp(-Br) - D_e. \tag{B.1}$$

Secondly, the deep potential well is formed using cubic spline interpolation of the points $\{(r_i, V_i)\}$. Spectroscopic data relevant to this region was collected in ref. [92] where it was used to construct an empirical potential curve. It was necessary to take into account a more recent value for the dissociation energy of the $X^1\Sigma_g^+$ potential from ref. [111]. We found that these points were then satisfactory to describe the inner well so long as it was not used too close to the peak of the barrier. R_2 was adjusted to reflect this. Thirdly, the barrier region itself is constructed using the addition of terms representing the exchange energy

$$V_{\text{ex}} = A_{\text{ex}}\exp(-B_{\text{ex}}r), \tag{B.2}$$

Construction of the $B^1\Pi_u$ potential			
Repulsive core			
R_1	$= 6.2631$	a_0	
A	$= 50.545842$	E_{H}^{-1}	
B	$= 1.3660218$	a_0^{-1}	
D_e	$= 9.64396 \times 10^{-3}$	E_{H}	[111]
Dispersion series			
R_2	$= 13.4271$	a_0	
R_3	$= 36.5752$	a_0	
C_3^{Σ}	$= 16.872$	$E_{\mathrm{H}} a_0^3$	[96]
C_3^{Π}	$= 8.436$	$E_{\mathrm{H}} a_0^3$	[96]
C_6^{Σ}	$= 9365$	$E_{\mathrm{H}} a_0^6$	[96]
C_6^{Π}	$= 6272$	$E_{\mathrm{H}} a_0^6$	[96]
$C_8^{\Sigma-}$	$= 1.975 \times 10^6$	$E_{\mathrm{H}} a_0^8$	[112]
$C_8^{\Pi-}$	$= 2.893 \times 10^5$	$E_{\mathrm{H}} a_0^8$	[112]
$C_8^{\Sigma+}$	$= 6.712 \times 10^6$	$E_{\mathrm{H}} a_0^8$	[112]
$C_8^{\Pi+}$	$= 7.623 \times 10^5$	$E_{\mathrm{H}} a_0^8$	[112]
C_{10}	$= -5.0365209 \times 10^7$	$E_{\mathrm{H}} a_0^{10}$	
α	$= 0.7331322$	a_0^{-1}	
β	$= 0.8830127$	a_0	
δ	$= 2.6292788 \times 10^{-4}$	E_{H}	
λ	$= 1.4488569 \times 10^4$	a_0	[150]
Exchange interaction			
A_{ex}	$= -7.0228988$	E_{H}	
B_{ex}	$= 0.70704443$	a_0^{-1}	

Table B.1: Constants for construction of the $B^1\Pi_u$ potential.

and the long range dispersion contribution

$$V_{d,1} = h_\Pi \frac{C_3^\Pi}{r^3} f_3 - \frac{C_6^\Pi}{r^6} f_6 - \frac{C_8^{\Pi+}}{r^8} f_8 + \frac{C_{10}}{r^{10}} f_{10} - \frac{\delta}{3}. \tag{B.3}$$

The damping terms are given by

$$f_n = \{1 - \exp[-\alpha(r - n\beta)]\}^n, \tag{B.4}$$

The retardation effect due to the finite speed of light is taken into account by including the terms

$$h_x = \cos(r_t) + r_t \sin(r_t) - \delta_{\Pi,x} r_t^2 \cos(r_t), \tag{B.5}$$

with $r_t = 2\pi r/\lambda$, and $\delta_{x,y}$ being the Kronecker delta.

Finally, the long range section is described using the Movre-Pichler model [96, 151, 152] which takes into account the atomic spin-orbit interaction. This arises since one atom is in the 4^2P electronically excited state. This is implemented by taking the $n = 3$ value from

$$V_{\mathrm{MP}} = 2\sqrt{\frac{-a}{3}} \cos\left[\frac{\phi}{3} + (n-1)\frac{2\pi}{3}\right] - \frac{p}{3} \tag{B.6}$$

where we have defined

$$\phi = \cos^{-1}\left(\frac{-b}{2\sqrt{\frac{-a^3}{27}}}\right), \tag{B.7}$$

$$b = \frac{2p^3 - 9pq + 27\nu}{27}, \tag{B.8}$$

$$a = \frac{3q - p^2}{3}, \tag{B.9}$$

$$p = -\left(V_{d,1} + V_{d,2} + V_{d,3}\right), \tag{B.10}$$

$$q = V_{d,1}V_{d,2} + V_{d,1}V_{d,3} + V_{d,2}V_{d,3} - \frac{\delta^2}{3}, \tag{B.11}$$

and,

$$\nu = -V_{d,1}V_{d,2}V_{d,3} + \left(V_{d,1} + V_{d,2} + V_{d,3}\right)\frac{\delta^2}{9} + \frac{2\delta^3}{27}. \tag{B.12}$$

Here the dispersion series are given

$$V_{d,2} = -h_\Pi \frac{C_3^\Pi}{r^3} f_3 - \frac{C_6^\Pi}{r^6} f_6 - \frac{C_8^{\Pi-}}{r^8} f_8 - \frac{\delta}{3}, \tag{B.13}$$

r (a_0)	V $\left(10^{-3}E_{\mathrm{H}}\right)$	r (a_0)	V $\left(10^{-3}E_{\mathrm{H}}\right)$	r (a_0)	V $\left(10^{-3}E_{\mathrm{H}}\right)$	r (a_0)	V $\left(10^{-3}E_{\mathrm{H}}\right)$
6.1788319	1.2410582	6.5577276	-3.3539503	8.5402393	-9.1356071	11.011434	-2.3188511
6.1849584	1.1395413	6.5845617	-3.6240043	8.7122044	-8.8004750	11.116314	-2.0720071
6.1933109	1.0218698	6.6127187	-3.8983321	8.8582802	-8.4684685	11.223272	-1.8302252
6.2028484	8.9103829×10^{-1}	6.6421984	-4.1768381	8.9896162	-8.1396241	11.332877	-1.5936785
6.2132589	7.4877264×10^{-1}	6.6731899	-4.4594174	9.1111256	-7.8139965	11.445504	-1.3625447
6.2244971	5.9623155×10^{-1}	6.7055042	-4.7459836	9.2260209	-7.4916221	11.561533	-1.1370243
6.2365460	4.3427343×10^{-1}	6.7395193	-5.0364500	9.3356250	-7.1725556	11.681531	-9.1732698×10^{-1}
6.2493735	2.6358263×10^{-1}	6.7754241	-5.3307300	9.4414497	-6.8568471	11.805875	-7.0368497×10^{-1}
6.2629398	8.4726421×10^{-2}	6.8132186	-5.6287553	9.5444398	-6.5445559	11.935132	-4.9636261×10^{-1}
6.2772923	-1.0182498×10^{-1}	6.8532808	-5.9304440	9.6449732	-6.2357321	12.070437	-2.9563781×10^{-1}
6.2922211	-2.9563781×10^{-1}	6.8959886	-6.2357321	9.7438059	-5.9304440	12.212544	-1.0182498×10^{-1}
6.3079058	-4.9636261×10^{-1}	6.9413420	-6.5445559	9.8413158	-5.6287553	12.362511	8.4726421×10^{-2}
6.3241575	-7.0368497×10^{-1}	6.9902859	-6.8568471	9.9378808	-5.3307300	12.522155	2.6358263×10^{-1}
6.3413540	-9.1732698×10^{-1}	7.0431983	-7.1725556	10.033879	-5.0364500	12.693302	4.3427343×10^{-1}
6.3591174	-1.1370243	7.1008349	-7.4916221	10.129310	-4.7459836	12.878593	5.9623155×10^{-1}
6.3778257	-1.3625447	7.1645187	-7.8139965	10.224741	-4.4594174	13.081693	7.4877264×10^{-1}
6.3971009	-1.5936785	7.2359503	-8.1396241	10.320361	-4.1768381	13.308092	8.9103829×10^{-1}
6.4173210	-1.8302252	7.3179644	-8.4684685	10.416170	-3.8983321	13.566930	1.0218698
6.4384859	-2.0720071	7.4154743	-8.8004750	10.512735	-3.6240043	13.875558	1.1395413
6.4604067	-2.3188511	7.5396293	-9.1356071	10.610056	-3.3539503	14.272223	1.2410582
6.4830834	-2.5706114	7.7287909	-9.4738148	10.708322	-3.0882886	...	...
6.5068940	-2.8271331	8.0048232	-9.6439574	10.807722	-2.8271331	...	...
6.5318384	-3.0882886	8.3042125	-9.4738148	10.908822	-2.5706114	...	...

Table B.2: Values of the $B^1\Pi_u$ at discrete radial separations. Values at intermediate points can by evaluated by cubic spline interpolation. These points were derived by the combination of the data presented refs. [76, 92, 93].

and,

$$V_{d,3} = h_\Sigma \frac{C_3^\Sigma}{r^3} f_3 - \frac{C_6^\Sigma}{r^6} f_6 - \frac{C_8^{\Sigma+}}{r^8} f_8 - \frac{\delta}{3}. \tag{B.14}$$

The process of comparing this potential to the experimental data is discussed in the main text.

B. THE $B^1\Pi_U$ POTENTIAL FROM PHOTODISSOCIATION SPECTROSCOPY

References

[1] M. H. Anderson, J. R. Ensher, M. R. Matthews, C. E. Wieman, and E. A. Cornell. **Observation of Bose-Einstein Condensation in a Dilute Atomic Vapor**. *Science*, **269**(5221):198–201, 1995. 15

[2] K. B. Davis, M. O. Mewes, M. R. Andrews, N. J. van Druten, D. S. Durfee, D. M. Kurn, and W. Ketterle. **Bose-Einstein Condensation in a Gas of Sodium Atoms**. *Phys. Rev. Lett.*, **75**:3969–3973, Nov 1995. 15

[3] S. N. Bose. **Plancks Gesetz und Lichtquantenhypothese**. *Zeitschrift für Physik A Hadrons and Nuclei*, **26**:178–181, 1924. 15

[4] A. Einstein. **Quantentheorie des einatomigen idealen Gases**. *Sitzungsber. Preuss. Akad. Wiss., Phys. Math. Kl.*, **1**:3, 1925. 15

[5] J. H. Metcalf and P. van der Straten. *Laser Cooling and Trapping*. Springer, 1999. 15

[6] E. Fermi. **Sulla quantizzazione del gas perfetto monoatomico.** *Ren. R. Accad. Lincei*, **3**:145, 1926. 15

[7] E. Fermi. **Zur Quantelung des Idealen Einatomigen Gases**. *Z. Phys.*, **36**:902, 1926. 15

[8] P. A. M. Dirac. **On the Theory of Quantum Mechanics.** *Proc. Roy. Soc. London A*, **112**:661, 1926. 15

[9] B. DeMarco and D. S. Jin. **Onset of Fermi Degeneracy in a Trapped Atomic Gas**. *Science*, **285**(5434):1703–1706, 1999. 15, 35

[10] T. Loftus, C. A. Regal, C. Ticknor, J. L. Bohn, and D. S. Jin. **Resonant Control of Elastic Collisions in an Optically Trapped Fermi Gas of Atoms**. *Phys. Rev. Lett.*, **88**(17):173201, 2002. 15, 35, 36, 137

[11] M. Greiner, C. A. Regal, and D. S. Jin. **Emergence of a molecular Bose-Einstein condensate from a Fermi gas**. *Nature (London)*, **426**:537–540, 2003. 15, 35

[12] K.-K. Ni, S. Ospelkaus, M. H. G. de Miranda, A. Pe'er, B. Neyenhuis, J. J. Zirbel, S. Kotochigova, P. S. Julienne, D. S. Jin, and J. Ye. **A High Phase-Space-Density Gas of Polar Molecules**. *Science*, **322**(5899):231–235, 2008. 15, 35

[13] M. Zaccanti, B. Deissler, C. DErrico, M. Fattori, M. Jona-Lasinio, S. Müller, G. Roati, M. Inguscio, and G. Modugno. **Observation of an Efimov spectrum in an atomic system**. *Nature Phys.*, **5**:586, 2009. 15, 17, 91, 92, 106, 108, 109

[14] R. Jördens, N. Strohmaier, K. Gunter, H. Moritz, and T. Esslinger. **A Mott insulator of fermionic atoms in an optical lattice**. *Nature (London)*, **455**:204–207, 2008. 15, 35

[15] J. T. Stewart, J. P. Gaebler, and D. S. Jin. **Using photoemission spectroscopy to probe a strongly interacting Fermi gas**. *Nature (London)*, **454**:744–747, 2008. 15, 35

[16] U. Schneider, L. Hackermüller, S. Will, Th. Best, I. Bloch, T. A. Costi, R. W. Helmes, D. Rasch, and A. Rosch. **Metallic and Insulating Phases of Repulsively Interacting Fermions in a 3D Optical Lattice**. *Science*, **322**(5907):1520–1525, 2008. 15, 35

[17] A. Simoni, F. Ferlaino, G. Roati, G. Modugno, and M. Inguscio. **Magnetic Control of the Interaction in Ultracold K-Rb Mixtures**. *Phys. Rev. Lett.*, **90**(16):163202, 2003. 15, 35

[18] S. Inouye, J. Goldwin, M. L. Olsen, C. Ticknor, J. L. Bohn, and D. S. Jin. **Observation of Heteronuclear Feshbach Resonances in a Mixture of Bosons and Fermions**. *Phys. Rev. Lett.*, **93**(18):183201, 2004. 15, 35

[19] F. Ferlaino, C. D'Errico, G. Roati, M. Zaccanti, M. Inguscio, G. Modugno, and A. Simoni. **Feshbach spectroscopy of a K-Rb atomic mixture**. *Phys. Rev. A*, **73**(4):040702, 2006. 15, 35

[20] J. J. Zirbel, K.-K. Ni, S. Ospelkaus, J. P. D'Incao, C. E. Wieman, J. Ye, and D. S. Jin. **Collisional Stability of Fermionic Feshbach Molecules**. *Phys. Rev. Lett.*, **100**(14):143201, 2008. 15, 35

[21] J. J. Zirbel, K.-K. Ni, S. Ospelkaus, T. L. Nicholson, M. L. Olsen, P. S. Julienne, C. E. Wieman, J. Ye, and D. S. Jin. **Heteronuclear molecules in an optical dipole trap**. *Phys. Rev. A*, **78**(1):013416, 2008. 15, 35

[22] C. Ospelkaus, S. Ospelkaus, L. Humbert, P. Ernst, K. Sengstock, and K. Bongs. **Ultracold Heteronuclear Molecules in a 3D Optical Lattice**. *Phys. Rev. Lett.*, **97**(12):120402, 2006. 15, 35

[23] S. Ospelkaus, C. Ospelkaus, L. Humbert, K. Sengstock, and K. Bongs. **Tuning of Heteronuclear Interactions in a Degenerate Fermi-Bose Mixture**. *Phys. Rev. Lett.*, **97**(12):120403, 2006. 15, 35

[24] S. Ospelkaus, K.-K. Ni, D. Wang, M. H. G. de Miranda, B. Neyenhuis, G. Quemener, P. S. Julienne, J. L. Bohn, D. S. Jin, and J. Ye. **Quantum-State Controlled Chemical Reactions of Ultracold Potassium-Rubidium Molecules**. *Science*, **327**(5967):853–857, 2010. 15, 35

[25] E. Wille, F. M. Spiegelhalder, G. Kerner, D. Naik, A. Trenkwalder, G. Hendl, F. Schreck, R. Grimm, T. G. Tiecke, J. T. M. Walraven, S. J. J. M. F. Kokkelmans, E. Tiesinga, and P. S. Julienne. **Exploring an Ultracold Fermi-Fermi Mixture: Interspecies Feshbach Resonances and Scattering Properties of ^{6}Li and ^{40}K**. *Phys. Rev. Lett.*, **100**(5):053201, 2008. 15, 35, 46

[26] C. J. Pethick and H. Smith. *Bose-Einstein Condensation in Dilute Gases*. Cambridge university press, 2001. 15, 30

[27] T. Köhler, K. Góral, and P. S. Julienne. **Production of cold molecules via magnetically tunable Feshbach resonances**. *Rev. Mod. Phys.*, **78**(4):1311–1361, 2006. 16, 23, 96, 98

[28] C. Chin, R. Grimm, P. Julienne, and E. Tiesinga. **Feshbach resonances in ultracold gases**. *Rev. Mod. Phys.*, **82**(2):1225–1286, 2010. 16, 23, 36, 43

[29] U. Fano. **Sullo spettro di assorbimento dei gas nobili presso il limite dello spettro darco.** *Nuovo Cimento*, **12**:154, 1935. 16

[30] U. Fano. **Effects of Configuration Interaction on Intensities and Phase Shifts**. *Phys. Rev.*, **124**:1866, 1961. 16

[31] H. Feshbach. **Unified theory of nuclear reactions**. *Ann. Phys.*, **5**:357, 1958. 16

[32] H. Feshbach. **Unified theory of nuclear reactions II**. *Ann. Phys.*, **19**:287, 1962. 16

[33] E. Tiesinga, B. J. Verhaar, and H. T. C. Stoof. **Threshold and resonance phenomena in ultracold ground-state collisions**. *Phys. Rev. A*, **47**(5):4114–4122, May 1993. 16

[34] V. Vuletić, A. J. Kerman, C. Chin, and S. Chu. **Observation of Low-Field Feshbach Resonances in Collisions of Cesium Atoms**. *Phys. Rev. Lett.*, pages 1406–1409, Feb 1999. 16

[35] S. Inouye, M. R. Andrews, J. Stenger, H.-J. Miesner, D. M. Stamper-Kurn, and W. Ketterle. **Observation of Feshbach resonances in a Bose-Einstein condensate**. *Nature (London)*, **392**:151–154, March 1998. 16, 133

[36] Ph. Courteille, R. S. Freeland, D. J. Heinzen, F. A. van Abeelen, and B. J. Verhaar. **Observation of a Feshbach Resonance in Cold Atom Scattering**. *Phys. Rev. Lett.*, **81**:69–72, Jul 1998. 16

[37] J. L. Roberts, N. R. Claussen, J. P. Burke, C. H. Greene, E. A. Cornell, and C. E. Wieman. **Resonant Magnetic Field Control of Elastic Scattering in Cold ^{85}Rb**. *Phys. Rev. Lett.*, **81**:5109–5112, Dec 1998. 16

[38] L. H. Thomas. **The Interaction Between a Neutron and a Proton and the Structure of H_3**. *Phys. Rev.*, **47**(12):903–909, Jun 1935. 16

[39] V. Efimov. **Energy levels arising from resonant two-body forces in a three-body system**. *Physics Letters B*, **33**:563–564, December 1970. 16, 91, 104

[40] W. Schöllkopf and J. P. Toennies. **Nondestructive Mass Selection of Small van der Waals Clusters**. *Science*, **266**(5189):1345–1348, 1994. 16

[41] W. Schöllkopf and J. P. Toennies. **The nondestructive detection of the helium dimer and trimer**. *The Journal of Chemical Physics*, **104**(3):1155–1158, 1996. 16, 75

[42] T. Kraemer, M. Mark, P. Waldburger, J. G. Danzl, C. Chin, B. Engeser, A. D. Lange, K. Pilch, A. Jaakkola, H. C. Nägerl, and R. Grimm. **Evidence for Efimov quantum states in an ultracold gas of cesium atoms,**. *Nature*, **440**:315–318, 2006. 17, 91

[43] T. B. Ottenstein, T. Lompe, M. Kohnen, A. N. Wenz, and S. Jochim. **Collisional Stability of a Three-Component Degenerate Fermi Gas**. *Phys. Rev. Lett.*, **101**:203202, Nov 2008. 17, 91

[44] J. H. Huckans, J. R. Williams, E. L. Hazlett, R. W. Stites, and K. M. O'Hara. **Three-Body Recombination in a Three-State Fermi Gas with Widely Tunable Interactions**. *Phys. Rev. Lett.*, **102**:165302, Apr 2009. 17, 91

[45] S. Knoop, F. Ferlaino, M. Mark, M. Berninger, H. Schöbel, H.C. Nägerl, and R. Grimm. **Observation of an Efimov-like trimer resonance in ultracold atom-dimer scattering**. *Nature Phys.*, **5**:227–230, 2009. 17, 91

[46] G. Barontini, C. Weber, F. Rabatti, J. Catani, G. Thalhammer, M. Inguscio, and F. Minardi. **Observation of heteronuclear atomic Efimov resonances**. *Phys. Rev. Lett.*, **103**:043201, 2009. 17, 91

[47] N. Gross, Z. Shotan, S. Kokkelmans, and L. Khaykovich. **Observation of Universality in Ultracold ^{7}Li Three-Body Recombination**. *Phys. Rev. Lett.*, **103**:163202, Oct 2009. 17, 91

[48] S. E. Pollack, D. Dries, and R. G. Hulet. **Universality in Three- and Four-Body Bound States of Ultracold Atoms**. *Science*, **326**(5960):1683–1685, 2009. 17, 91

[49] S. Nakajima, M. Horikoshi, T. Mukaiyama, P. Naidon, and M. Ueda. **Nonuniversal Efimov Atom-Dimer Resonances in a Three-Component Mixture of ^{6}Li**. *Phys. Rev. Lett.*, **105**:023201, Jul 2010. 17, 91

[50] N. Gross, Z. Shotan, S. Kokkelmans, and L. Khaykovich. **Nuclear-Spin-Independent Short-Range Three-Body Physics in Ultracold Atoms**. *Phys. Rev. Lett.*, **105**:103203, Sep 2010. 17, 91

[51] T. Lompe, T. B. Ottenstein, F. Serwane, K. Viering, A. N. Wenz, G. Zürn, and S. Jochim. **Atom-Dimer Scattering in a Three-Component Fermi Gas**. *Phys. Rev. Lett.*, **105**:103201, Sep 2010. 17, 91

[52] S. Nakajima, M. Horikoshi, T. Mukaiyama, P. Naidon, and M. Ueda. **Measurement of an Efimov Trimer Binding Energy in a Three-Component Mixture of ^{6}Li**. *Phys. Rev. Lett.*, **106**:143201, Apr 2011. 17, 91

[53] L. D. Faddeev. *Mathematical Aspects of the Three-Body Problem in the Quantum Scattering Theory*. Sivan, Jerusalem, 1965. 17, 83, 112

[54] E. O. Alt, P. Grassberger, and W. Sandhas. **Reduction of the three-particle collision problem to multi-channel two-particle Lippmann-Schwinger equations**. *Nuc. Phys. B*, **2**(2):167–180, June 1967. 17, 18, 103, 112, 126

[55] J. R. Taylor. *Scattering theory*. Dover, New York, 1972. 19, 20, 21, 22, 23, 26, 41, 42, 44, 62, 69, 80, 94, 97, 117, 118

[56] R. G. Newton. *Scattering theory of waves and particles.* Dover, New York, 1966. 20, 22, 26, 41, 62, 77, 78, 79, 80, 83, 89, 94, 104, 112, 113, 114, 117, 119, 124

[57] B. H. Bransden and C. J Joachain. *Physics of atoms and molecules.* Pearson, 1983. 28, 29, 37, 61

[58] G. Herzberg. *Molecular spectra and molecular structure. Spectra of diatomic molecules.* Van Nostrand, New York, 1939. 29

[59] H. T. C. Stoof, J. M. V. A. Koelman, and B. J. Verhaar. **Spin-exchange and dipole relaxation rates in atomic hydrogen: Rigorous and simplified calculations**. *Phys. Rev. B*, **38**(7):4688–4697, 1988. 32, 36, 38, 41, 42, 46

[60] J. R. Zacharias. **The Nuclear Spin and Magnetic Moment of ^{4}0K**. *Phys. Rev.*, **61**(5-6):270–276, 1942. 35, 36

[61] C. A. Regal, C. Ticknor, J. L. Bohn, and D. S. Jin. **Tuning p-wave Interactions in an Ultracold Fermi Gas of Atoms**. *Phys. Rev. Lett.*, **90**(5):053201, 2003. 36, 137

[62] C. Ticknor, C. A. Regal, D. S. Jin, and J. L. Bohn. **Multiplet structure of Feshbach resonances in nonzero partial waves**. *Phys. Rev. A*, **69**(4):042712, 2004. 36, 134, 138

[63] C. A. Regal and D. S. Jin. **Measurement of Positive and Negative Scattering Lengths in a Fermi Gas of Atoms**. *Phys. Rev. Lett.*, **90**(23):230404, 2003. 36, 39

[64] E. Arimondo, M. Inguscio, and P. Violino. **Experimental determinations of the hyperfine structure in the alkali atoms**. *Rev. Mod. Phys.*, **49**(1):31–75, 1977. 36

[65] T. M. Hanna, E. Tiesinga, and P. S. Julienne. **Prediction of Feshbach resonances from three input parameters**. *Phys. Rev. A*, **79**(4):040701, 2009. 37, 46

[66] T. G. Tiecke, M. R. Goosen, A. Ludewig, S. D. Gensemer, S. Kraft, S. J. J. M. F. Kokkelmans, and J. T. M. Walraven. **Broad Feshbach Resonance in the ^{6}Li-^{40}K Mixture**. *Phys. Rev. Lett.*, **104**(5):053202, 2010. 37, 46, 50, 51, 133

[67] S. Falke, H. Knöckel, J. Friebe, M. Riedmann, E. Tiemann, and C. Lisdat. **Potassium ground-state scattering parameters and Born-Oppenheimer potentials from molecular spectroscopy**. *Phys. Rev. A*, **78**(1):012503, 2008. 37, 50, 53

[68] U. Schneider, L. Hackermüller, J. P. Ronzheimer, S. Will, S. Braun, T. Best, I. Bloch, E. Demler, S. Mandt, D. Rasch, and A. Rosch. **Breakdown of diffusion: From collisional hydrodynamics to a continuous quantum walk in a homogeneous Hubbard model**. *ArXiv e-prints*, May 2010. 38, 134, 136

[69] M. Gustavsson, E. Haller, M. J. Mark, J. G. Danzl, G. Rojas-Kopeinig, and H.-C. Nägerl. **Control of Interaction-Induced Dephasing of Bloch Oscillations**. *Phys. Rev. Lett.*, **100**(8):080404, 2008. 38, 137

[70] C. A. Regal, M. Greiner, and D. S. Jin. **Observation of Resonance Condensation of Fermionic Atom Pairs**. *Phys. Rev. Lett.*, **92**(4):040403, 2004. 39, 137

[71] C. A. Regal. ***Experimental realization of BCS-BEC crossover physics with a Fermi gas of atoms***. PhD thesis, University of Colorado, 2006. 39

[72] J. P. Gaebler, J. T. Stewart, J. L. Bohn, and D. S. Jin. **p-wave Feshbach molecules**. *Phys. Rev. Lett.*, **98**:200403, 2007. 40

[73] B. R. Johnson. **The multichannel log-derivative method for scattering calculations**. *J. Comput. Phys.*, **13**(3):445 – 449, 1973. 38

[74] J. M. Hutson. **Coupled channel methods for solving the bound-state Schrödinger equation**. *Comput. Phys. Commun.*, **84**(1-3):1 – 18, 1994. 38, 44

[75] Mies et al. **Estimating Bounds on Collisional Relaxation Rates of Spin-Polarized ^{87}Rb Atoms at Ultracold Temperatures**. *J. Natl Inst. Stand. Technol.*, **101**:521, 1996. 38

[76] S. Falke, H. Knöckel, J. Friebe, M. Riedmann, E. Tiemann, and C. Lisdat. **Potassium ground-state scattering parameters and Born-Oppenheimer potentials from molecular spectroscopy**. *Phys. Rev. A*, **78**(1):012503, 2008. 38, 41, 56, 73, 142

[77] D. E. Manolopoulos. **An improved log derivative method for inelastic scattering**. *J. Chem. Phys.*, **85**(11):6425–6429, 1986. 42, 68

[78] D. Naik, A. Trenkwalder, C. Kohstall, F. Spiegelhalder, M. Zaccanti, G. Hendl, F. Schreck, R. Grimm, T. Hanna, and P. Julienne. **Feshbach resonances in the ^{6}Li-^{40}K Fermi-Fermi mixture: elastic versus inelastic interactions**. *The European Physical Journal D - Atomic, Molecular, Optical and Plasma Physics*, **65**:55–65, 2011. 43

[79] J. M. Hutson. **Feshbach resonances in ultracold atomic and molecular collisions: threshold behaviour and suppression of poles in scattering lengths**. *New Journal of Physics*, **9**(5):152, 2007. 43

[80] J. L. Bohn and P. S. Julienne. **Semianalytic theory of laser-assisted resonant cold collisions**. *Phys. Rev. A*, **60**(1):414–425, 1999. 43, 67

[81] P. O. Fedichev, Y. Kagan, G. V. Shlyapnikov, and J. T. M. Walraven. **Influence of Nearly Resonant Light on the Scattering Length in Low-Temperature Atomic Gases**. *Phys. Rev. Lett.*, **77**(14):2913–2916, 1996. 43, 56

[82] B. Gao, E. Tiesinga, C. J. Williams, and P. S. Julienne. **Multichannel quantum-defect theory for slow atomic collisions**. *Phys. Rev. A*, **72**:042719, Oct 2005. 44

[83] A. M. Kaufman, R. P. Anderson, Thomas M. Hanna, E. Tiesinga, P. S. Julienne, and D. S. Hall. **Radio-frequency dressing of multiple Feshbach resonances**. *Phys. Rev. A*, **80**:050701, Nov 2009. 46

[84] T. M. Hanna, E. Tiesinga, and P. S. Julienne. **Creation and manipulation of Feshbach resonances with radiofrequency radiation**. *New Journal of Physics*, **12**(8):083031, 2010. 46

[85] B. J. Verhaar, E. G. M. van Kempen, and S. J. J. M. F. Kokkelmans. **Predicting scattering properties of ultracold atoms: Adiabatic accumulated phase method and mass scaling**. *Phys. Rev. A*, **79**:032711, Mar 2009. 46

[86] Z. Li, S. Singh, T. V. Tscherbul, and K. W. Madison. **Feshbach resonances in ultracold ^{85}Rb-^{87}Rb and ^{6}Li-^{87}Rb mixtures**. *Phys. Rev. A*, **78**:022710, Aug 2008. 46

[87] A.-C. Voigt, M. Taglieber, L. Costa, T. Aoki, W. Wieser, T. W. Hänsch, and K. Dieckmann. **Ultracold Heteronuclear Fermi-Fermi Molecules**. *Phys. Rev. Lett.*, **102**:020405, Jan 2009. 46

[88] B. Deh, W. Gunton, B. G. Klappauf, Z. Li, M. Semczuk, J. Van Dongen, and K. W. Madison. **Giant Feshbach resonances in ^{6}Li-^{85}Rb mixtures**. *Phys. Rev. A*, **82**:020701, Aug 2010. 46

[89] S. Knoop, T. Schuster, R. Scelle, A. Trautmann, J. Appmeier, M. K. Oberthaler, E. Tiesinga, and E. Tiemann. **Feshbach spectroscopy and analysis of the interaction potentials of ultracold sodium**. *Phys. Rev. A*, **83**:042704, Apr 2011. 46

[90] M. R. Goosen, T. G. Tiecke, W. Vassen, and S. J. J. M. F. Kokkelmans. **Feshbach resonances in ^{3}He*-^{4}He* mixtures**. *Phys. Rev. A*, **82**:042713, Oct 2010. 46

[91] T. V. Tscherbul, T. Calarco, I. Lesanovsky, R. V. Krems, A. Dalgarno, and J. Schmiedmayer. **rf-field-induced Feshbach resonances**. *Phys. Rev. A*, **81**:050701, May 2010. 46

[92] J. Heinze, U. Schüle, F. Engelke, and C. D. Caldwell. **Doppler-free polarization spectroscopy of the $B^1\Pi_u - X^1\Sigma_g^+$ band system of $\mathbf{K}_2$**. *J. Chem. Phys.*, **87**(1):45–53, 1987. 56, 73, 139, 142

[93] J. Heinze and F. Engelke. **The $B^1\Pi_u$ potential energy curve and dissociation energy of $^{39}K_2$**. *J. Chem. Phys.*, **89**(1):42–50, 1988. 56, 73, 142

[94] J. Heinze, P. Kowalczyk, and F. Engelke. **Quasibound levels and shape resonances of $^{39}K_2(B^1\Pi_u)$ crossed laser?molecular beam studies and analytical interpretation**. *J. Chem. Phys.*, **89**(6):3428–3434, 1988. 56

[95] B. K. Clark, J. M. Standard, Z. J. Smolinski, D. P. Ripp, and J. R. Fleming. **Optically pumped laser emission in K_2 involving rovibrational levels near the $B^1\Pi_u$ state dissociation limit**. *Chemical Physics*, **213**(1-3):229 – 241, 1996. 56

[96] H. Wang, P. L. Gould, and W. C. Stwalley. **Long-range interaction of the $^{39}K(4s)+^{39}K(4p)$ asymptote by photoassociative spectroscopy. I. The 0_g^- pure long-range state and the long-range potential constants**. *J. Chem. Phys.*, **106**(19):7899–7912, 1997. 56, 73, 140, 141

[97] K. Bergmann, H. Theuer, and B. W. Shore. **Coherent population transfer among quantum states of atoms and molecules**. *Rev. Mod. Phys.*, **70**:1003–1025, Jul 1998. 56

[98] S. J. J. M. F. Kokkelmans, H. M. J. Vissers, and B. J. Verhaar. **Formation of a Bose condensate of stable molecules via a Feshbach resonance**. *Phys. Rev. A*, **63**:031601, Feb 2001. 56

[99] K. Winkler, F. Lang, G. Thalhammer, P. v. d. Straten, R. Grimm, and J. Hecker Denschlag. **Coherent Optical Transfer of Feshbach Molecules to a Lower Vibrational State**. *Phys. Rev. Lett.*, **98**:043201, Jan 2007. 56

[100] M. Theis, G. Thalhammer, K. Winkler, M. Hellwig, G. Ruff, R. Grimm, and J. Hecker Denschlag. **Tuning the Scattering Length with an Optically Induced Feshbach Resonance**. *Phys. Rev. Lett.*, **93**:123001, Sep 2004. 56

[101] T. Mullins, W. Salzmann, S. Götz, M. Albert, J. Eng, R. Wester, M. Weidemüller, F. Weise, A. Merli, S. M. Weber, F. Sauer,

L. Wöste, and A. Lindinger. **Photoassociation and coherent transient dynamics in the interaction of ultracold rubidium atoms with shaped femtosecond pulses. I. Experiment**. *Phys. Rev. A*, **80**:063416, Dec 2009. 56

[102] A. Merli, F. Eimer, F. Weise, Albrecht L., W. Salzmann, T. Mullins, S. Götz, R. Wester, M. Weidemüller, R. Ağanoğlu, and C. P. Koch. **Photoassociation and coherent transient dynamics in the interaction of ultracold rubidium atoms with shaped femtosecond pulses. II. Theory**. *Phys. Rev. A*, **80**:063417, Dec 2009. 56

[103] O. Dulieu. private communication. 56

[104] E. Hodby, S. T. Thompson, C. A. Regal, M. Greiner, A. C. Wilson, D. S. Jin, E. A. Cornell, and C. E. Wieman. **Production Efficiency of Ultracold Feshbach Molecules in Bosonic and Fermionic Systems**. *Phys. Rev. Lett.*, **94**:120402, Mar 2005. 57

[105] M. Gell-Mann and M. L. Goldberger. **The Formal Theory of Scattering**. *Phys. Rev.*, **91**:398–408, Jul 1953. 63

[106] C. Boisseau, E. Audouard, J. Vigué, and P. S. Julienne. **Reflection approximation in photoassociation spectroscopy**. *Phys. Rev. A*, **62**:052705, Oct 2000. 65, 73

[107] R. Ciuryło, E. Tiesinga, and P. S. Julienne. **Stationary phase approximation for the strength of optical Feshbach resonances**. *Phys. Rev. A*, **74**:022710, Aug 2006. 67

[108] Y. B. Band, K. F. Freed, and D. J. Kouri. **Half-collision description of final state distributions of the photodissociation of polyatomic molecules**. *J. Chem. Phys.*, **74**(8):4380–4394, 1981. 69

[109] M. H. Alexander. **A linear reference potential algorithm for the study of molecular photodissociation**. *Comput. Phys. Commun.*, **75**(1-2):87 – 97, 1993. 69

[110] D. E. Manolopoulos and M. H. Alexander. **Quantum flux redistribution during molecular photodissociation**. *J. Chem. Phys.*, **97**(4):2527–2535, 1992. 69

[111] St. Falke, I. Sherstov, E. Tiemann, and Ch. Lisdat. **The $A^1\Sigma_u^+$ state of K_2 up to the dissociation limit**. *J. Chem. Phys.*, **125**(22):224303, 2006. 73, 139, 140

[112] M. Marinescu and A. Dalgarno. **Dispersion forces and long-range electronic transition dipole moments of alkali-metal dimer excited states**. *Phys. Rev. A*, **52**:311–328, 1995. 73, 140

[113] K. T. Tang, J. P. Toennies, and C. L. Yiu. **Accurate Analytical He-He van der Waals Potential Based on Perturbation Theory**. *Phys. Rev. Lett.*, **74**(9):1546–1549, Feb 1995. 75, 77, 78, 82

[114] P. Barletta and A. Kievsky. **Variational description of the helium trimer using correlated hyperspherical harmonic basis functions**. *Phys. Rev. A*, **64**(4):042514, Sep 2001. 75, 76, 82, 86, 87, 89

[115] C. Lovelace. **Practical Theory of Three-Particle States. I. Nonrelativistic**. *Phys. Rev.*, **135**(5B):B1225–B1249, Sep 1964. 76, 79, 85, 112

[116] E. Tiesinga, C. J. Williams, and P. S. Julienne. **Photoassociative spectroscopy of highly excited vibrational levels of alkali-metal dimers: Green-function approach for eigenvalue solvers**. *Phys. Rev. A*, **57**(6):4257–4267, Jun 1998. 76

[117] L. D. Faddeev. *Mathematical Aspects of the Three-Body Problem in the Quantum Scattering Theory*. Sivan, Jerusalem, 1965. 76, 83

[118] R. A. Aziz and M. J. Slaman. **An examination of ab initio results for the helium potential energy curve**. *J. Chem. Phys.*, **94**(12):8047–8053, 1991. 77

[119] B. Liu and A. D. McLean. **The interacting correlated fragments model for weak interactions, basis set superposition error, and the helium dimer potential**. *J. Chem. Phys.*, **91**(4):2348–2359, 1989. 77

[120] E. W. Schmid and H. Ziegelmann. *The quantum mechanical three-body problem*. Oxford: Pergamon Press, Oxford, 1974. 79, 83

[121] K. Goral, T. Kohler, S. A. Gardiner, E. Tiesinga, and P. S. Julienne. **Adiabatic association of ultracold molecules via magnetic-field tunable interactions**. *J. Phys. B*, **37**(17):3457–3500, 2004. 79

[122] S. Nakaichi-Maeda and T. K. Lim. **Zero-energy scattering and bound states in the ^{4}He trimer and tetramer**. *Phys. Rev. A*, **28**(2):692–696, Aug 1983. 83

[123] J. Avery. *Hyperspherical harmonics: applications in quantum theory*. Kluwer academic, Dordrecht, 1934. 88

[124] E. O. Alt, P. Grassberger, and W. Sandhas. **Reduction of the three-particle collision problem to multi-channel two-particle Lippmann-Schwinger equations**. *Nuc. Phys. B*, **2**(2):167–180, June 1967. 89

[125] T. Weber, J. Herbig, M. Mark, H.-C. Nägerl, and R. Grimm. **Bose-Einstein Condensation of Cesium**. *Science*, **299**(5604):232–235, 2003. 91

[126] C. D'Errico, M. Zaccanti, M. Fattori, G. Roati, M. Inguscio, G. Modugno, and A. Simoni. **Feshbach resonances in ultracold ^{39}K**. *New Journal of Physics*, **9**(7):223, 2007. 92

[127] M. D. Lee, T. Köhler, and P. S. Julienne. **Excited Thomas-Efimov levels in ultracold gases**. *Phys. Rev. A*, **76**(1):012720, 2007. 92, 105, 106

[128] S. T. Rittenhouse, N. P. Mehta, and C. H. Greene. **Green's functions and the adiabatic hyperspherical method**. *Phys. Rev. A*, **82**:022706, Aug 2010. 101

[129] E. Braaten and H.-W. Hammer. **Enhanced dimer relaxation in an atomic and molecular Bose-Einstein condensate**. *Phys. Rev. A*, **70**:042706, Oct 2004. 101

[130] E. Nielsen and J. H. Macek. **Low-Energy Recombination of Identical Bosons by Three-Body Collisions**. *Phys. Rev. Lett.*, **83**:1566–1569, Aug 1999. 105

[131] A. J. Moerdijk, H. M. J. M. Boesten, and B. J. Verhaar. **Decay of trapped ultracold alkali atoms by recombination**. *Phys. Rev. A*, **53**:916–920, Feb 1996. 105

[132] Y. Kagan, B. V. Svistunov, and G. V. Shlyapnikov. **Effect of Bose condensation on inelastic processes in gases**. *JETP Lett.*, **42**:209, 1985. 105

[133] E. A. Burt, R. W. Ghrist, C. J. Myatt, M. J. Holland, E. A. Cornell, and C. E. Wieman. **Coherence, Correlations, and Collisions: What One Learns about Bose-Einstein Condensates from Their Decay**. *Phys. Rev. Lett.*, **79**:337–340, Jul 1997. 105

[134] P. O. Fedichev, M. W. Reynolds, and G. V. Shlyapnikov. **Three-Body Recombination of Ultracold Atoms to a Weakly Bound s Level**. *Phys. Rev. Lett.*, **77**:2921–2924, Sep 1996. 108

[135] M. Berninger, A. Zenesini, B. Huang, W. Harm, H.-C. Nägerl, F. Ferlaino, R. Grimm, P. S. Julienne, and J. M. Hutson. **Universality of the Three-Body Parameter for Efimov States in Ultracold Cesium**. *Phys. Rev. Lett.*, **107**:120401, Sep 2011. 108

[136] J. P. D'Incao, C. H. Greene, and B. D. Esry. **The short-range three-body phase and other issues impacting the observation of Efimov physics in ultracold quantum gases**. *Journal of Physics B: Atomic, Molecular and Optical Physics*, **42**(4):044016, 2009. 108

[137] E. Kolganova, A. Motovilov, and W. Sandhas. **The ^{4}He Trimer as an Efimov System**. *Few-Body Systems*, **51**:249–257, 2011. 111

[138] D. Bollé. **Separable approximations to the off-shell two-body t and K matrices at positive energies**. *Il Nuovo Cimento A (1971-1996)*, **12**:651–664, 1972. 112

[139] M. Scadron and S. Weinberg. **Potential Theory Calculations by the Quasiparticle Method**. *Phys. Rev.*, **133**:B1589–B1596, Mar 1964. 112

[140] K. Meetz. **Spectrum of the Scattering Integral Operator in the Physical Energy Sheet**. *Journal of Mathematical Physics*, **3**(4):690–699, 1962. 112, 113, 124

[141] E. Harms. **Convenient Expansion for Local Potentials**. *Phys. Rev. C*, **1**(5):1667–1679, May 1970. 112, 113, 114

[142] T. A. Osborn. **On the convergence of separable expansions for the t-matrix**. *J. Math. Phys*, **14**:373, 1973. 112

[143] D. Hilbert. *Grundzüge einer allgemeinen Theorie der linearen Integralgleichungen*. Leipzig, 1912. 113

[144] M. Kitagawa, K. Enomoto, Kentaro Kasa, Y. Takahashi, R. Ciuryło, P. Naidon, and P. S. Julienne. **Two-color photoassociation spectroscopy of ytterbium atoms and the precise determinations of s-wave scattering lengths**. *Phys. Rev. A*, **77**:012719, Jan 2008. 115, 119, 121

[145] W. M. Frank, D. J. Land, and R. M. Spector. **Singular Potentials**. *Rev. Mod. Phys.*, **43**(1):36–98, Jan 1971. 114

[146] G. F. Gribakin and V. V. Flambaum. **Calculation of the scattering length in atomic collisions using the semiclassical approximation**. *Phys. Rev. A*, **48**(1):546–553, Jul 1993. 114, 119

[147] C. A. Regal, C. Ticknor, J. L. Bohn, and D. S. Jin. **Creation of ultracold molecules from a Fermi gas of atoms**. *Nature (London)*, **424**(5):47, 2003. 137

[148] R. Jördens, L. Tarruell, D. Greif, T. Uehlinger, N. Strohmaier, H. Moritz, T. Esslinger, L. De Leo, C. Kollath, A. Georges, V. Scarola, L. Pollet, E. Burovski, E. Kozik, and M. Troyer. **Quantitative Determination of Temperature in the Approach to Magnetic Order of Ultracold Fermions in an Optical Lattice**. *Phys. Rev. Lett.*, **104**(18):180401, 2010. 137

[149] K. Günter, T. Stöferle, H. Moritz, M. Köhl, and T. Esslinger. *p*-**wave Interactions in Low-Dimensional Fermionic Gases**. *Phys. Rev. Lett.*, **95**(23):230401, 2005. 138

[150] C. Corliss and J. Sugar. *J. Phys. Chem. Ref. Data*, **8**:1109–1145, 1979. 140

[151] M. Movre and G. Pichler. **Resonance interaction and self-broadening of alkali resonance lines. I. Adiabatic potential curves**. *J. Phys. B*, **10**(2631), 1977. 141

[152] K. M. Jones, E. Tiesinga, P. D. Lett, and P. S. Julienne. **Ultracold photoassociation spectroscopy: Long-range molecules and atomic scattering**. *Rev. Mod. Phys.*, **78**:483–535, 2006. 141